

Assessment of Conceptual Hybrid-Electric Regional Aircraft with Boundary-Layer Ingestion Propeller

Yi-Kai Peng

Technische Universiteit Delft



ASSESSMENT OF CONCEPTUAL HYBRID-ELECTRIC REGIONAL AIRCRAFT WITH BOUNDARY-LAYER INGESTION PROPELLER

by

Yi-Kai Peng

in partial fulfillment of the requirements for the degree of

Master of Science
in Aerospace Engineering

at the Delft University of Technology,
to be defended publicly on Monday November 27, 2023 at 1:00 PM.

Supervisor:	Dr. ir. M. F. M. (Maurice) Hoogreef,	TU Delft	
	Dr. ir. V. O. (Vincent) Bonnin,	TU Delft	
Thesis committee:	Dr. ir. G. (Gianfranco) La Rocca,	TU Delft,	Chair
	Dr. R. (Roberto) Merino Martinez,	TU Delft,	Examiner

An electronic version of this thesis is available at <http://repository.tudelft.nl/>.

PREFACE

This thesis can only be fulfilled with much help. First of all, I want to give much gratitude to Vincent and Maurice, who gave me a lot of input, feedback, and guidance throughout this journey. I was chaotic and lost in this thesis journey many times. However, Vincent spent a lot of time and patience to put me back on track, and Maurice always saw through my problem when I was stuck. In the end, I can reach the final destination.

Thanks to fellows in room NB1.09, Pranav, Lukas, and Dhruv, who gave me a lot of out-of-box perspectives and ideas to overcome challenges. Moreover, I want to give special thanks to Egon, who worked on many assignments with me since the first year and helped me go through many study challenges. Furthermore, thanks to all my friends in Delft who made my master's study very enjoyable.

Last but not least, thanks to my family, who supported me a lot, especially financially, and offered me the privilege to study in the Netherlands. Moreover, I want to thank my girlfriend, who gave me emotional support throughout the thesis and put my mind at ease.

謝謝爸爸媽媽支持我來荷蘭念書，還有謝謝羿寶的不離不棄，最後謝謝羿寶媽的電鍋讓我方便煮飯。

Yi-Kai Peng

彭依愷

Delft, November 2023

ABSTRACT

Boundary Layer Ingestion (BLI) is a promising propulsion concept for aviation, aiming to reduce fuel burn. This configuration involves using the propulsor to ingest the boundary layer from the fuselage or wing. Typically, aircraft with BLI propulsors also integrate a hybrid-electric powertrain. This integrated setup has shown potential in fuel burn reduction. This thesis investigates the interactive effects of BLI-induced power-saving benefits and aircraft design parameters on overall performance, focusing on a fuselage tail-mounted BLI propeller.

The thesis has three primary objectives. First, it seeks to enhance the fidelity of the existing BLI model within a conceptual aircraft design tool. The improvement involves transitioning from the actuator disk theory to the blade element theory (BET) with gradient-based optimization. Additionally, a surrogate model is established with this improvement through multidisciplinary design optimization (MDO), design of experiment (DoE), and response surface methodology (RSM) to predict power-saving benefits based on fuselage geometric and operational parameters. Comparison reveals discrepancies between the existing BLI model and the surrogate model, emphasizing the influence of blade aerodynamics.

The second and third objectives delve into the sensitivity of aircraft-level performance and powertrain settings. The conceptual aircraft design tool, Aircraft Design Initiator (Initiator), is used for sizing, with the surrogate model integrated. The study uses a regional turboprop ATR-72 as a reference conventional aircraft design and employs a partial-turboelectric (PTE) architecture for the hybrid-electric powertrain in the radical aircraft design. A sensitivity analysis varying design parameters by $\pm 20\%$, including fuselage slenderness ratio, propeller size ratio, and shaft-power ratio, reveals their impact on BLI effects and aircraft-level performance.

The study reveals that fuselage length significantly impacts fuel weight and, consequently, aircraft performance. Surprisingly, aero-propulsive benefits from BLI do not directly enhance overall aircraft performance, attributed to an associated weight penalty. Instead, the shaft-power ratio and propeller size ratio prove significant at the system level. Further investigation into powertrain settings suggests that radical BLI-equipped aircraft designs are not able to surpass the energy efficiency of conventional counterparts. Additionally, the proposed surrogate model exhibits a limited applicable range, especially under high BLI propeller disk loading, rooted in underlying physical constraints in propeller design. These findings prompt a critical examination of the feasibility of hybrid-electric powertrains with BLI for regional turboprop aircraft, with a note of caution regarding potential variations in modeling methods and assumptions.

CONTENTS

Abstract	v
List of Figures	ix
List of Tables	xi
Nomenclature	xi
1 Introduction	1
1.1 Research Background	2
1.1.1 Fuselage-propulsor level research.	3
1.1.2 Aircraft-level research	5
1.1.3 Exiting boundary-layer ingestion model	6
1.2 Research Question	8
1.3 Thesis outlines	9
2 Methodology	11
2.1 Conceptual aircraft design tool	12
2.1.1 Validation of the conceptual aircraft design tool	13
2.2 Boundary layer ingestion modeling.	15
2.3 Propeller design	17
2.3.1 Validation of propeller design	19
2.4 Propeller optimization	21
2.5 Surrogate model	25
2.5.1 Surrogate model during the cruise	25
2.5.2 Lookup table during other flight phases	27
2.6 Integration of the surrogate model	31
2.7 Powertrain modeling.	33
2.8 Aircraft-level key performance indicators	34
3 Result and Discussion	37
3.1 Reliability of the response surface	37
3.2 Comparison between actuator disk and surrogate models	38
3.3 Conceptual hybrid-electric aircraft results	41
3.3.1 Comparison between baseline radical design and reference design	41
3.3.2 Sensitivity of aircraft-level KPIs to design parameters	44
3.3.3 Investigation of the powertrain setting	47
3.3.4 Investigation of constraints of the surrogate model	49
4 Conclusion and Recommendation	55
4.1 Conclusion remark.	55
4.2 Recommendation for future work.	57

A	Radial Basis Function Interpolation	59
A.1	Basic concept	59
A.2	Additional polynomial precision	59
A.3	Type of RBF Kernel	60
A.4	Sensitivity study of parameters for RBF kernel	61

LIST OF FIGURES

1.1	Development of the boundary layer over the flat plat [10]	2
1.2	Different BLI configurations from [11]	2
1.3	Thick boundary layer over the tail of an axisymmetric body [12]	3
1.4	Principle of the boundary-layer ingestion mechanism [13]	3
1.5	Pressure distribution around the fuselage-propulsor configuration from [14]	4
1.6	Velocity profile on an upswept tailcone [21]	5
1.7	The HEA design with the BLI propulsor	6
1.8	Streamline curve around the vertical tail from [4]	7
2.1	The overview of methodology at the BLI-propeller level. The large box on the top represents the section in this chapter.	11
2.2	The high-level perspective of integration of surrogate model with the aircraft design tool to account for BLI effects.	12
2.3	The workflow of Aircraft Design Initiator [32].	12
2.4	Schematic flow adapted from Hoogreef et al. [32] about the power and energy sizing	13
2.5	The geometry of ATR-72 reproduced from the Initiator	14
2.6	Workflow of the BLI model from the in-house report [18]	15
2.7	Equivalent flowfield for the uninstalled BLI propeller reproduced from [18].	15
2.8	The demonstration of the velocity profile used in this study	15
2.9	Workflow of the new approach to model the boundary layer profile	16
2.10	The control volume surrounds the bare fuselage with a propeller derived from [4, 14, 15].	16
2.11	Workflow of the propeller design	17
2.12	Comparison between different aerodynamic polar and data from XFOIL	18
2.13	The lifting-line representation of the propeller from van Arnhem [43]	19
2.14	Propeller performance (a) to (c), and the lift-to-drag polar comparison (d).	20
2.15	Propeller optimization loop	21
2.16	The chord and twist distribution of the blade described by the CST method	22
2.17	BLI propeller design with forward swept and lean angle from Costa et al. [50]	24
2.18	The setup of building data points for the surrogate model	26
2.19	Demonstration of the data distribution with two independent variables (λ_{fus}, J) and the dependent variable ($\Delta\eta_p$). Values of data point are normalized.	27
2.20	The procedure of creating the lookup table	28
2.21	Demonstration of the $T_c - \eta_p$ plot. The analysis case is with λ_p of 0.63 with light designed disk loading.	28
2.22	The lookup table with all propeller sizes	29
2.23	Example of surface created by different propeller sizes with scattered validation points.	30
2.24	Scattered validation points on different surfaces	31
2.25	Constraint diagram generated by the Initiator	31
2.26	Workflow of integration part of the surrogate model	32
2.27	Integration of the propeller-level surrogate model with the conceptual aircraft sizing loop	33

2.28	The PTE architecture adapted from [29]. Blue components belong to the primary propulsion system, and green components belong to the secondary propulsion system.	33
3.1	Four different independent variables versus the equivalent thrust coefficient.	38
3.2	Comparison between estimated value from the actuator disk model and surrogate model.	39
3.3	Difference in $\Delta\eta_p$ between actuator disk model and surrogate model.	40
3.4	Velocity profile in two models when λ_p is 10% higher than the baseline.	40
3.5	Comparison of aircraft geometry in a top-view perspective, generated from the Initiator	43
3.6	The sensitivity of aircraft-level KPIs to the change of design parameters	45
3.7	The sensitivity of propulsion system weight to the change of design parameters	46
3.8	The sensitivity of BLI effects to the change of design parameters	47
3.9	The change of KPIs for the aircraft with different setting of ϕ	48
3.10	Comparison of chord and twist distributions of three additional BLI propeller design	51
3.11	All optimized propeller planform for BLI with different blade numbers.	52
A.1	R^2 value against N with different c	62
A.2	Number of matched validation point against N with different c	62
A.3	Mean deviation against N with different c	62
A.4	Max deviation against N with different c	62
A.5	Average error against N with different c	62

LIST OF TABLES

2.1	Top-level requirements of ATR-72 [32, 38, 39]	13
2.2	Parameter comparison between Initiator and real aircraft for ATR-72-600. Reference data is taken from [38, 39].	14
2.3	Required key aerodynamic parameters for XROTOR	18
2.4	Bounds for design variables. All values in this table is not normalized.	22
2.5	Independent variables for DoE, the bound refers to Roskam [53]	25
2.6	Electrical powertrain component technology assumption in this thesis, values of efficiency refers to Bonnin and Hoogreef [33].	34
3.1	Lower and upper bounds of thrust coefficients for different propellers.	38
3.2	Baseline design variables	39
3.3	Aircraft KPIs comparison between reference design and baseline radical design	41
3.4	Baseline design variables	49
3.5	The resulting power-saving benefit of the corresponding blade number	53
4.1	Summary of the sensitivity study of the aircraft performance	56
A.1	Classical kernel of radial basis function. Recompiled from [56, 59, 60]	60

NOMENCLATURE

Greek letters

β	Propeller twist angle	[rad]
δ_{99}	Boundary layer thickness	[-]
η_p	Propeller efficiency $\frac{T}{P_s} V_\infty$	[-]
γ_a	Axial free vortex circulation	[-]
γ_t	Tangential free vortex circulation	[-]
λ_p	Propeller size ratio $\frac{D_p}{D_{fus}}$	[-]
λ_{fus}	Fuselage slenderness ratio $\frac{L_{fus}}{D_{fus}}$	[-]
λ_{tc}	Tailcone slenderness ratio $\frac{L_{tc}}{D_{fus}}$	[-]
Ω	Rotational speed	[rad/s]
Φ	Supplied-power ratio / Dissipation rate	[-] / [-]
ϕ	Shaft-power ratio	[-]
ρ	Air density	[kg/m ³]

Roman symbols

A	Bernstein coefficient	[-]
c	Smoothing parameter / Chord length	[-] / [m]
$C_{D0,cruise}$	Profile drag coefficient at the cruise	[-]
C_p	Pressure coefficient	[-]
C_Q	Torque coefficient $\frac{T}{\rho n^2 D^5}$	[-]
C_t	Thrust coefficient $\frac{T}{\rho n^2 D^4}$	[-]
D_{fus}	Fuselage diameter	[m]
D_p	Propeller diameter	[m]
$E_{mission}$	Energy for flight mission	[J]
F_X	Streamwise net force	[N]
J	Advance ratio	[-]
L_{fus}	Fuselage length	[m]

L_{tc}	Tailcone length	[<i>m</i>]
N	Degree of polynomial / Coefficient of Class function	[-] / [-]
n	Revolutions per second	[-]
N_{crit}	Critical amplification factor	[-]
P_K	Kinetic energy inflow rate	[<i>W</i>]
P_s	Shaft power	[<i>W</i>]
R	Aircraft range	[<i>km</i>]
R^2	Coefficient of determination	[-]
S	Wing area	[<i>m</i> ²]
SS_E	Sum of squared residuals	[-]
SS_T	Sum of squared total	[-]
T	Thrust force	[<i>N</i>]
$T_{c,\infty}$	Thrust coefficient $\frac{T}{\rho V_\infty^2 D_p^2}$	[-]
$T_{c,des}$	Designed thrust coefficient	[-]
$T_{c,eq}$	Equivalent thrust coefficient $\frac{T}{\rho V_{eq}^2 D_p^2}$	[-]
U	Boundary layer tangential velocity	[<i>m/s</i> ²]
V	Boundary layer wall-normal velocity	[<i>m/s</i> ²]
V_∞	Freestream velocity	[<i>m/s</i> ²]
V_{eq}	Equivalent mean boundary layer velocity	[<i>m/s</i> ²]
W	Aircraft weight	[<i>N</i>]
W_{PL}	Payload weight	[<i>N</i>]

Abbreviations

BAT	Battery
EM	Electric motor
GB	Gear box
GT	Gas turbine
PM	Power management system
P	Propulsor
<i>BET</i>	Blade element theory
<i>BLI</i>	Boundary-layer ingestion

<i>CFD</i>	Computational fluid dynamics
<i>DoE</i>	Design of experiment
<i>ESP</i>	Equivalent specific power
<i>EU</i>	European Union
<i>FM</i>	Fuel mass
<i>HEA</i>	Hybrid-electric aircraft
<i>KPI</i>	Key performance indicator
<i>LHS</i>	Latin hypercube sampling
<i>LUT</i>	Lookup table
<i>MTOM</i>	Maximum takeoff mass
<i>OEM</i>	Operational empty mass
<i>PBM</i>	Power balance method
<i>PcP</i>	Power control parameter
<i>PREE</i>	Payload range energy efficiency
<i>PSC</i>	Power-saving coefficient
<i>PTE</i>	Partial-turboelectric
<i>RBF</i>	Radial basis function
<i>RSM</i>	Response surface methodology
<i>SM</i>	Surrogate model
<i>SPPH</i>	Serial-parallel partial hybrid

1

INTRODUCTION

Industry governance institutions have set up stricter environmental impact regulations to meet sustainable development. Particularly, the European Union (EU) proposed a road map to reach net-zero emissions by 2050 [1]. In the aviation sector, the report of Flightpath 2050 [2] established an ambitious goal to reduce 75% CO_2 and 90% NO_x emissions per passenger kilometer compared to typical new aircraft in 2000.

New energy carriers, such as sustainable aviation fuel and hydrogen, with hybrid-electric powertrains have been investigated to move toward sustainable aviation. On top of these advancements, one of the airframe-propulsor integrated configurations is also a promising solution to decrease energy consumption, namely boundary-layer ingestion (BLI). BLI utilizes the energy from the fuselage surface boundary layer and reduces the power requirement of the propulsor.

Several studies have focused on the configuration of the fuselage-propulsor and have confirmed the benefits of using the BLI mechanism [3, 4, 5, 6]. These studies, which exclude the factors of other aircraft subsystems, concluded that providing power supply to the propulsor in BLI conditions is lower than ingesting the freestream. Furthermore, recent research on BLI in hybrid-electric aircraft by NASA and the EU, such as STARC-ABL [7, 8] and CENTRELINE [9], have shown a reduction in fuel burn ranging from 3% to 5% compared to their conventional baseline. These studies consider the impact of different aircraft systems and optimize aircraft performance.

However, the airframe and BLI propulsor integration involve many factors influencing the power-saving benefit, such as the assumption of hybrid-electric powertrains, fuselage geometric parameters, and the BLI propulsor size. Previous studies do not fully cover the interactive effects of various powertrain settings and geometric parameters together on the aircraft level. Therefore, the presented work considers those factors and focuses on the impact on aircraft-level performance.

1.1. RESEARCH BACKGROUND

When air encounters an object, the friction between air particles and the surface generates a tangential force. This frictional effect causes a layer of air particles to slow down, gradually increasing as more particles get caught in this deceleration process [10]. Additionally, air viscosity resists the deformation of this layer, giving rise to a thin layer of airflow known as the boundary layer. The development of a typical flat plate boundary layer is illustrated in Figure 1.1. The distance from the surface to the point where the velocity reaches 99% of the freestream velocity defines the boundary layer thickness (δ_{99}).

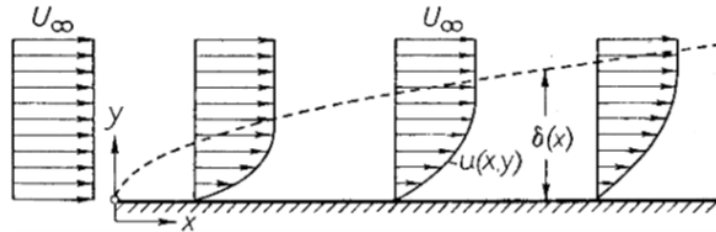


Figure 1.1: Development of the boundary layer over the flat plate [10]

Within the boundary layer, the friction force at the wall and the viscosity of the air cause the dissipation of the heat, leading to the wasted energy around the object. Therefore, the boundary layer ingestion configuration is proposed to exploit this wasted energy and further reduce the dependency on the power source.

Several BLI configurations ingest the boundary layer from different sources, as shown in Figure 1.2. Steiner et al. [11] performed a sensitivity study with certain drag assumptions and concluded that ingesting the annular fuselage boundary-layer flow, corresponding to the PROPFUS concept, achieves the most significant power savings for the propulsor. Therefore, this thesis focuses on the aircraft configuration with fuselage tail-mounted BLI propulsor.

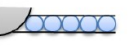
Concept	Description and Abbreviation
	Aft-mounted fans covering the upper part of a cylindrical fuselage (REVOLVE)
	BWB with embedded fans on top of the lifting body trailing edge (BWB)
	Tube and wing configuration with fans integrated within a split-wing (SPLIT)
	Tube and wing concept with fans mounted on the upper wing side (WING)
	Cylindrical fuselage with circumferential fan at the aft section (PROPFUS)
	Cross-flow fan embedded into the trailing edge of the wing (CROSS)

Figure 1.2: Different BLI configurations from [11]

It is important to note that the geometry of an object's surface plays a vital role in determining the progression of its boundary layer. The characteristics of the boundary layer on the fuselage, partic-

ularly around the tailcone section, differ from those on the flat plate due to the surface curvature. Figure 1.3 shows a sketch of the boundary layer at the tail of the axisymmetric body from Patel [12].

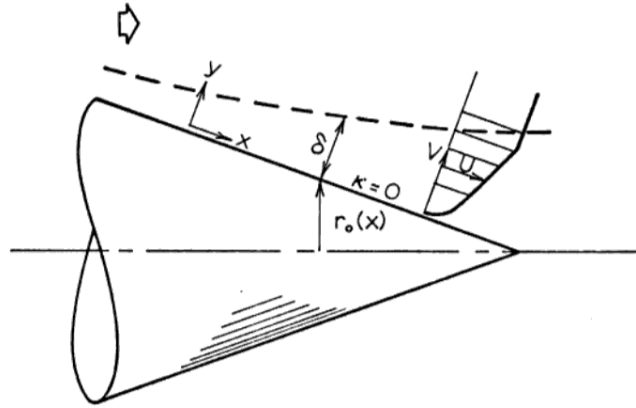


Figure 1.3: Thick boundary layer over the tail of an axisymmetric body [12]

The streamline within the boundary layer is decomposed into wall-normal (V) and tangential (U) velocities. Moreover, Patel [12] suggested three findings due to the diminishing radius of the axisymmetric body:

1. The rapid thickening of the boundary layer leads to significant flow divergence.
2. The flow at the tail of axisymmetric body has strong viscous-inviscid interaction.
3. The constant pressure assumption in the y -direction, as used in the flat plate case, is invalid.

Therefore, considering the wall-normal velocity effect within the boundary layer is essential in the design of BLI propulsors, particularly in the context of the tail of the fuselage. The current research regarding the tail-mounted BLI propulsor configuration can be categorized into fuselage-propulsor level and aircraft-level research. Fuselage-propulsor level research focuses on the combined aerodynamic behavior of the BLI propulsor-fuselage system. In contrast, aircraft-level research emphasizes the impact on aircraft performance.

1.1.1.1. FUSELAGE-PROPULSOR LEVEL RESEARCH

The BLI propulsor reduces required power by accelerating the low-speed fuselage boundary layer through the propulsor, reducing downstream jet and wake energy dissipation. Figure 1.4 illustrates this mechanism. Smith [3] noted that the energy contribution from the upstream boundary layer could increase propulsive efficiency (η_p), gaining power-saving benefits. Furthermore, he proposed a power-saving coefficient (PSC) to quantify the power-saving benefit by showing the change of total power from freestream, noted as non-BLI, to BLI configuration, as shown in Equation 1.1

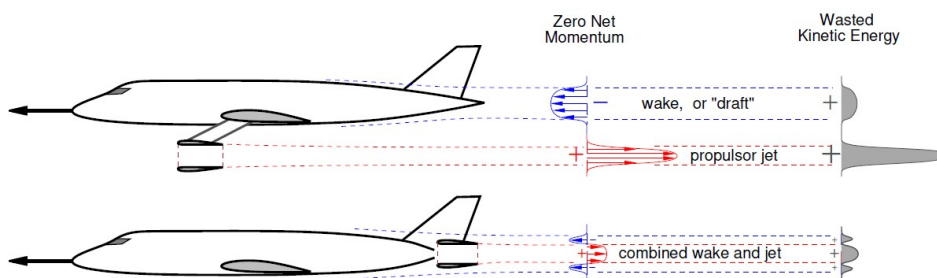


Figure 1.4: Principle of the boundary-layer ingestion mechanism [13]

$$PSC = \frac{P_{non-BLI} - P_{BLI}}{P_{non-BLI}} \quad (1.1)$$

Although BLI offers power-saving benefits to reduce energy consumption, this mechanism leads to an increase in profile drag and challenges in the conventional aircraft design context. The fuselage tail-mounted BLI propulsor accelerates the upstream boundary layer inflow to decrease the boundary-layer thickness and static pressure, resulting in the increase in friction drag and pressure drag [3, 14]. Figure 1.5 illustrates the expansion of low-pressure area around the tailcone due to the BLI effect in the CFD simulation from Lv et al. [14]

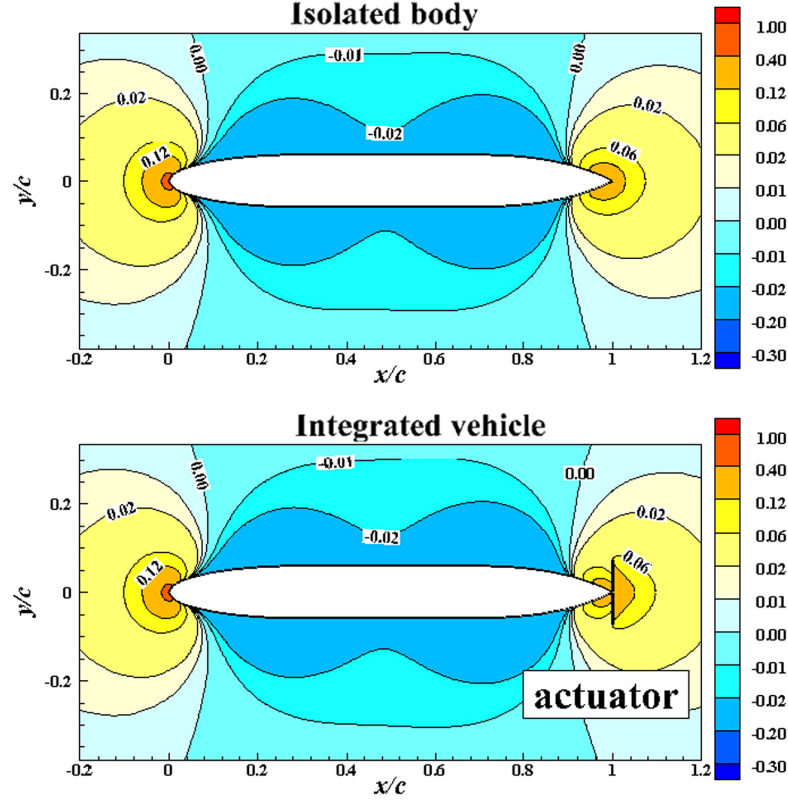


Figure 1.5: Pressure distribution around the fuselage-propulsor configuration from [14]

Furthermore, BLI also introduces ambiguity to the conventional thrust-to-drag definition because part of the fuselage profile drag contributes to the propulsor thrust. To resolve these problems due to BLI, Drela [15] proposed a power balance method (PBM) to analyze the BLI system from a kinetic-rate perspective. PBM utilizes a control volume surrounding a fuselage-propulsor configuration to analyze the power flow. Thus, the required power for the BLI propulsor can be determined.

On the other hand, the reduction in the required power leads to a problem with the definition of η_p . Conventional freestream propulsive efficiency is the ratio between the power propelling the aircraft and the power used to accelerate the air. However, due to the low-speed boundary layer in the propulsor inflow, several studies [3, 14, 16, 17] indicated that the value of η_p can exceed the unity and have a maximum of 2 theoretically. In an early time, Smith [3] proposed using a "propulsive coefficient" for BLI cases as it violates the definition of efficiency. Later, Lv et al. [14] explained the abnormal η_p using PBM, stating that the conventional definition fails to reflect the true energy output and input ratio. In this thesis, the definition of η_p partially refers to the in-house report [18], in which the propulsor shaft power is calculated for the required thrust, and the thrust-to-power ratio is normalized by the freestream velocity in order to fit into the aircraft sizing tool.

In recent decades, wind tunnel experiments and computational fluid dynamics (CFD) simulations utilizing models from prior research [13, 14, 19, 20] confirm the power-saving benefits of BLI in comparison to reference models. These research employ PBM to calculate the power of the BLI propulsor. However, PBM requires the velocity and pressure data within the control volume, which is not applicable in this thesis due to the limitations of the conceptual aircraft sizing method. This thesis uses a relatively low-fidelity method to model BLI effects, which is elaborated in section 2.2.

In addition, the influence of the geometric parameters has been studied as the fuselage-propulsor system is a bilateral relation in terms of power-saving benefits. Fuselage geometry, encompassing variables like fuselage length, diameter, and tailcone upsweep, emerges as a crucial factor impacting the extent of these power-saving benefits [4, 19]. Ahuja et al. [4] showed that a longer fuselage provides 8.3% more inflow power to the BLI propulsor than its baseline. Moreover, Habermann et al. [21] indicated that a tailcone upsweep angle of 3.5° requires 19% more power for the BLI propulsor due to the asymmetric boundary-layer development, as presented in Figure 1.6. Furthermore, Smith [3] and Baskaran et al. [22] showed that the size of the BLI propulsor significantly influences the extent of power saving. A larger propulsor ingests more freestream portion than the boundary layer, diminishing the advantage of utilizing the power within the boundary layer. Therefore, using BLI saves power rather than ingesting freestream, yet it is affected by the interaction of many design parameters.

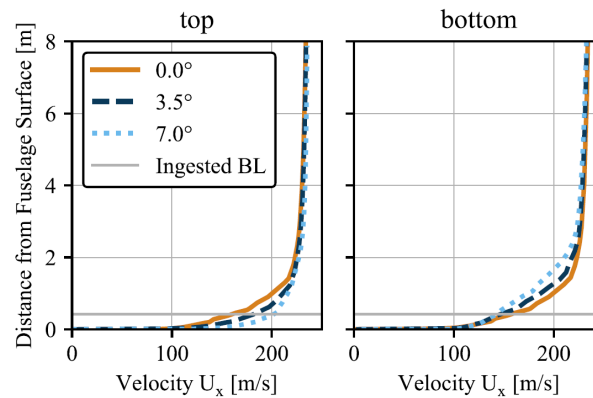


Figure 1.6: Velocity profile on an upswept tailcone [21]

1.1.2. AIRCRAFT-LEVEL RESEARCH

When it comes to aircraft-level research, integration of the BLI propulsion system with the hybrid-electric powertrain is a common approach for reducing fuel burn. NASA has conducted extensive research on BLI hybrid-electric aircraft (HEA), including N3-X [23], SUGAR Freeze with BLI [24], STARC-ABL [7, 8], and SUSAN [25], while the EU has worked on projects such as NOVA [26] and CENTRELINE [27]. The HEA design entails configuring power control parameters (PcP) in the hybrid-electric powertrain to obtain optimal aircraft-level key performance indicators (KPIs). PcP encompasses power allocation between underwing engines and BLI propulsors, denoted as the shaft-power ratio (ϕ). However, if a battery is present, an additional parameter indicates the ratio of power supplied by batteries, referred to as the supplied-power ratio (Φ). Additionally, common KPIs applied to HEA include maximum takeoff weight (MTOW), operational empty weight (OEW), fuel weight (FW), and payload range energy efficiency (PREE) [28, 29].

BLI aircraft studies frequently investigate the combination of a partial-turboelectric (PTE) powertrain and BLI propulsors. Notably, the CENTRELINE and STARC-ABL projects, as shown in Figure 1.7, focusing on medium-to-long range tube-and-wing HEA designs, revealed elevated OEW but reduced fuel weight through advanced powertrain configurations [8, 9]. A similar pattern can



(a) STARC-ABL project coordinated by NASA [30]



(b) CENTRELINE project coordinated by BAUHAUS LUFTFAHRT EV [31]

Figure 1.7: The HEA design with the BLI propulsor

be seen in the results from Hoogreef et al. [32], where a sensitivity study was conducted on various conceptual aircraft designs with the PTE powertrain and BLI technology. When the hybrid-electric powertrain shares less than 20% of total shaft power with the BLI propulsor, it can obtain the power-saving benefit with the technology level in 2050. A higher power-sharing causes the weight penalty to the aircraft and induces the cyclic effect on MTOW due to the additional component weight from the powertrain.

However, Bonnin and Hoogreef [33] presented an alternative perspective on fuel burn reduction for regional turboprop aircraft, underscoring the significance of powertrain modeling methodology. Their study investigated the reduction of the energy requirement for BLI with PTE and serial-parallel partial hybrid (SPPH) powertrains across regional, medium-range, and long-haul aircraft categories. The powertrain modeling method is discussed in detail in section 2.7, which follows a "black box" approach from de Vries et al. [34]. The hybrid-electric regional turboprop aircraft with the BLI propulsor cannot obtain the reduction in fuel burn, showing no benefit from BLI can impact the final aircraft design. Moreover, the weight penalty from the battery becomes a dominant effect in the SPPH powertrain.

In the study from Bonnin and Hoogreef [33], the PcP settings remain constant at each flight phase throughout the analysis, meaning a constant power sharing between underwing propellers and the BLI propulsor is set during the cruise. This setting and the powertrain modeling approach potentially elucidate divergent conclusions from the aforementioned major projects. This thesis, however, follows the same approach to reduce the degree of freedom in the research and exerts more effort on the influence of the BLI effect on aircraft performance.

Another attention should be paid that the BLI model used in [32, 33] is highly simplified. The detailed background information about this BLI model is discussed in the next section.

1.1.3. EXITING BOUNDARY-LAYER INGESTION MODEL

The existing BLI model mentioned in the previous section will be used as the fundamental framework to assess the power-saving benefit of BLI. This model is compiled in MATLAB and valid for unducted propeller design. There are several assumptions and theories, as described by the in-house report [18]:

1. Axisymmetric fuselage body representation
2. Low-speed boundary-layer velocity profile
3. Constant pressure field in wall-normal direction

4. No consideration of empennage and wing downwash distortion
5. Actuator disk theory with a uniform inflow to the disk plane
6. Incompressible flow
7. No iterative dependencies of effects of the BLI propulsor and fuselage

As previously discussed in [subsection 1.1.1](#), using an axisymmetric fuselage body representation can underestimate the required power for the BLI propulsor. Additionally, the boundary-layer velocity profile, which is mentioned in Point 2, is measured from the in-house report by della Corte [35]. The wind tunnel experiment is conducted with a freestream velocity of 25[m/s], so its validity at high subsonic speed may be questionable.

Point 3 states that the pressure field in the wall-normal direction is assumed constant. The pressure coefficient in such direction is simply computed by [Equation 1.2](#), in which $C_{p,TE}$ refers to the pressure coefficient at the tailcone trailing edge. However, as previously discussed in [section 1.1](#), the wall-normal direction has velocity perturbations that could affect this assumption, especially when δ_{99} is relatively thick.

$$C_{p,TE} = 1 - \left(\frac{V_{Edge}}{V_{\infty}} \right)^2 \quad (1.2)$$

Point 4 states that the empennage disruption and wing downwash are not included. However, the study by Ahuja et al. [4] showed that the BLI propulsor needs 19% more power with a wing-downwash effect without proper wing-fuselage fairing design. Yet, the empennage can contribute extra wake energy to the BLI propulsor, as the red strip behind the vertical tail in [Figure 1.8](#). Furthermore, Kenway and Kiris [36] suggested that wing downwash increases the upper BLI propulsor plane's high-pressure area, amplifying the inflow distortion. Although these studies are based on the non-axisymmetric fuselage, the wing downwash can still have a similar effect on the BLI propulsor with the axisymmetric fuselage.

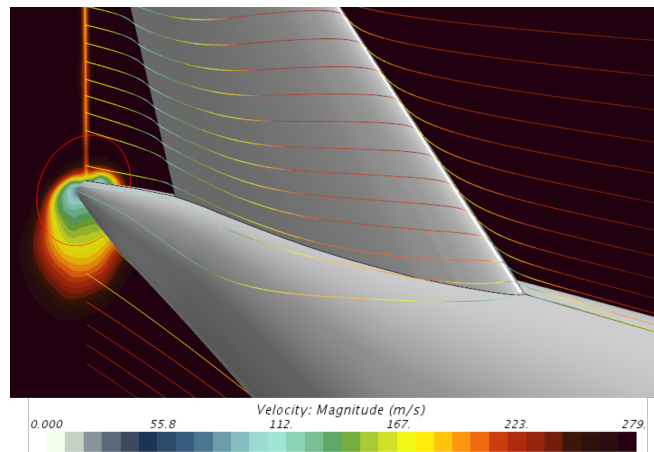


Figure 1.8: Streamline curve around the vertical tail from [4]

Point 5 states that the BLI model is based on the actuator disk theory, assuming that the velocity and the static pressure are uniform in the stream tube. However, the uniform flow will overestimate the power-saving benefit when more high-speed flow is ingested. Moreover, the actuator disk theory does not account for the blade aerodynamic effect. Lastly, the model uses incompressible flow calculation without compressibility correction on the actuator disk model.

The final point, Point 7, highlights a non-iterative process when evaluating the interaction between the BLI propeller and fuselage. In this process, the upstream fuselage's flowfield superimposes on that of the BLI propeller, assuming the BLI propeller operates within an equivalent flowfield. However, when evaluating the power-saving benefit, the model does not account for the acceleration of the boundary layer, meaning the BLI propeller remains unaffected by its upstream effect on the boundary layer.

While there are various ways to improve or replace existing assumptions and theories, it's vital to consider three key factors when choosing and implementing solutions:

1. Minimize impact on other assumptions in the existing BLI model.
2. Ensure smooth coding integration with the current BLI model.
3. Assess the practicality of the chosen approach, considering factors like computational resources.

Optimally, addressing all assumptions is crucial to enhancing the existing BLI model's capacity to calculate power-saving benefits, facilitating a more comprehensive treatment of the underlying physical phenomena. Nevertheless, practical constraints related to the thesis framework and time-frame necessitate a reasonable approach. Consequently, Point 5 is selected for further exploration to strengthen the model's credibility, as elaborated in detail in [section 2.2](#).

1.2. RESEARCH QUESTION

Based on the literature review, [subsection 1.1.1](#) shows that BLI can reduce required power at the system level, but the same effect is not necessarily obtained at the aircraft level as discussed in [subsection 1.1.2](#). As many studies have investigated the system-level BLI effect, the main research objective should focus on aircraft-level effects. The research gap analysis found that there are two groups of research. The first group [4, 21, 22] emphasizes the influence of fuselage or propulsor geometric parameters on the fuselage-propulsor level. In contrast, the second group [8, 9, 32, 33] focuses on the powertrain technology scenario and PcP settings on the aircraft level. However, there is a need for a comprehensive study that connects the focus of both groups. Considering the limitations of the existing BLI model, this need brings into a main research question: ***What is the sensitivity of aircraft-level key performance indicators to boundary layer ingestion effects affected by aircraft design parameters?***

This thesis concentrates on regional turboprop aircraft design within the context of the existing BLI model, which primarily applies to unducted propellers. The reference aircraft for the regional turboprop class is ATR-72, which is representative of its class. Moreover, as a result of the significant weight penalty associated with using batteries, the hybrid-electric powertrain modeling specifically addresses the PTE architecture.

The central focus of this thesis lies in assessing how BLI effects, influenced by various aircraft design parameters, affect aircraft-level KPIs. The primary aircraft design parameters under consideration are the fuselage slenderness ratio, propeller size ratio, and the shaft-power ratio setting. To address these topics effectively, three sub-research questions must be answered:

1. What alternative approach could improve the limitations in the existing boundary-layer ingestion model?
2. How do changes in the fuselage and BLI propeller size affect the power-saving benefit on the aircraft level?
3. What is the optimal powertrain setting to maximize aircraft energy efficiency?

1.3. THESIS OUTLINES

This thesis consists of four chapters, including this Introduction. [chapter 2](#) describes the method to answer the research questions, including the improvement over the BLI model and aircraft sizing process. Next, [chapter 3](#) presents and analyzes results to answer research questions. Lastly, [chapter 4](#) concludes the findings and proposes the potential improvement in future work.

2

METHODOLOGY

Figure 2.1 provides an overview and dependencies of all approaches at the BLI-propeller level. In order to answer the first research question, it is necessary to develop a new approach to create an improved BLI model. As the existing BLI model assesses the power-saving benefits based on the actuator disk theory, the blade aerodynamic effect is not considered. Therefore, the blade element theory (BET) method is proposed to account for the propeller performance.

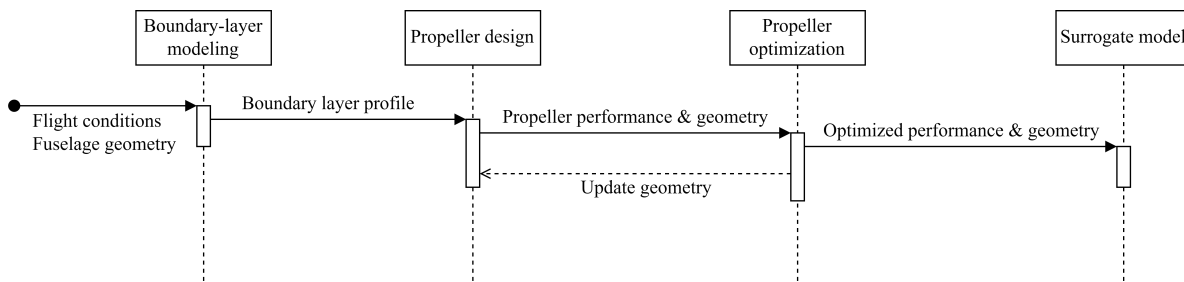


Figure 2.1: The overview of methodology at the BLI-propeller level. The large box on the top represents the section in this chapter.

The BET method requires the boundary layer velocity profile to be modeled since the propeller blade is divided into individual sections, requiring the local inflow condition. Therefore, the first step is to model the boundary layer velocity profile as explained in [section 2.2](#). Once the velocity profile is determined, the propeller design and analysis method can be accomplished using XFOIL and XROTOR, which will be discussed in [section 2.3](#), along with a case validation from the literature. The thesis focuses on the fuselage tail-mounted BLI propeller design. Thus, combining two approaches leads to optimizing the propeller for the boundary layer profile, resulting in an optimal design for BLI. The optimization setup is elaborated in [section 2.4](#).

Directly integrating the aircraft sizing tool and propeller optimization proves impractical. Therefore, a statistical approach in the form of a surrogate model provides a solution to this challenge. The surrogate model construction process is detailed in [section 2.5](#).

Shifting the focus to the aircraft level, given the thesis's emphasis on aircraft-level performance affected by BLI effects, [Figure 2.2](#) presents the interaction between the BLI propeller surrogate model and the aircraft sizing. The programming modification and model integration details are discussed in [section 2.6](#). Furthermore, the hybrid-electric powertrain framework and essential parameters are outlined in [section 2.7](#), and KPIs at the aircraft level are discussed in [section 2.8](#).

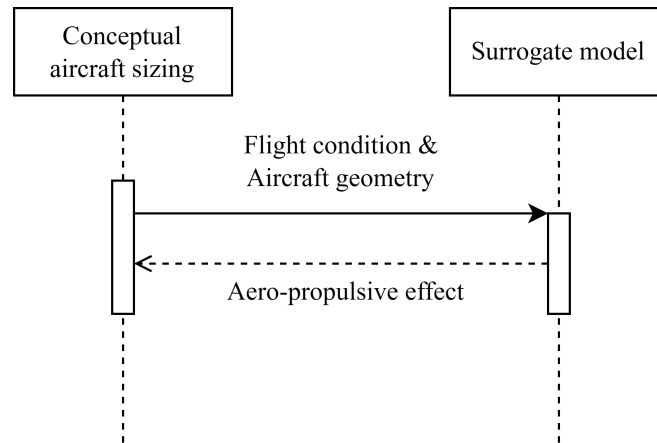


Figure 2.2: The high-level perspective of integration of surrogate model with the aircraft design tool to account for BLI effects.

Before delving deeper into each method in [Figure 2.1](#), the conceptual aircraft design tool is first introduced in [section 2.1](#) as it is the primary tool to answer the main research question.

2.1. CONCEPTUAL AIRCRAFT DESIGN TOOL

Aircraft Design Initiator (Initiator), developed by the Flight Performance and Propulsion track, uses MATLAB to perform conceptual aircraft design [37]. As shown in [Figure 2.3](#), the design loop in the Initiator comprises three major modules: Class I and Class II weight estimation and Class 2.5 simplified finite-element method structure analysis. Each module is divided into sub-modules and is interdependent. For hybrid-electric aircraft sizing, the design loop follows the procedure in de Vries et al. [29] A user has to provide top-level requirements in the input file to the Initiator, and the program will iterate and produce a feasible design.

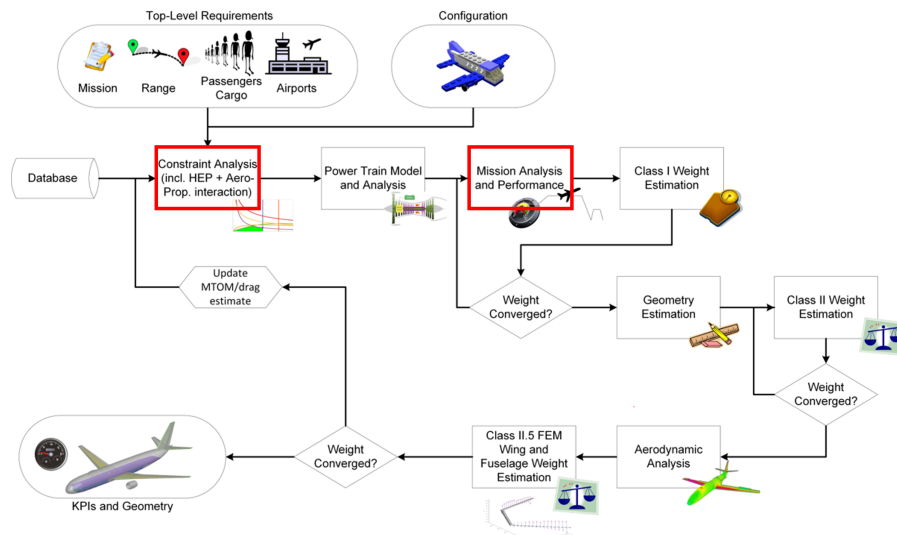


Figure 2.3: The workflow of Aircraft Design Initiator [32].

Furthermore, it is crucial to consider the impact of the hybrid-electric powertrain's secondary propulsion system. Hoogreef et al. [32] mentioned that this workflow allows for the inclusion of aero-propulsive effects within different constraints in the design-point diagram, particularly within the

highlighted sizing modules in Figure 2.3. A schematic flow, adapted from Hoogreef et al. [32], pointing out the power and energy sizing with aero-propulsive effects for the aircraft is presented in Figure 2.4. For a detailed examination of constraint and mission analysis modules, refer to section 2.6. These modules evaluate numerous design points, taking into account aero-propulsive effects, making the propeller optimization mentioned in Figure 2.1 impractical to implement within the context of Figure 2.3. Consequently, the thesis proposes a surrogate model as an alternative approach to incorporate aero-propulsive effects.

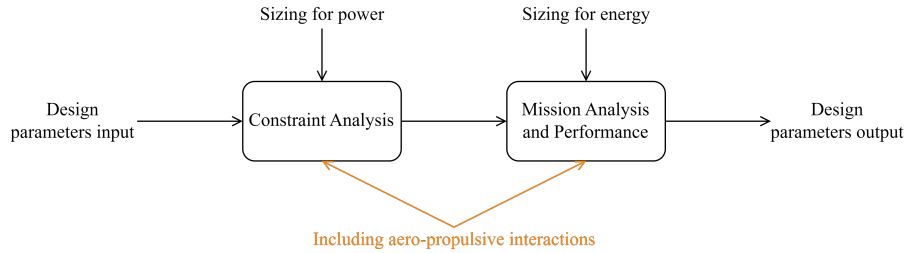


Figure 2.4: Schematic flow adapted from Hoogreef et al. [32] about the power and energy sizing

2.1.1.1. VALIDATION OF THE CONCEPTUAL AIRCRAFT DESIGN TOOL

This validation centers on the ATR-72 aircraft, a model that is representative of its class. ATR-72 employs underwing turboprops with a conventional powertrain for propulsion, and it is replicated using the Initiator and validated by juxtaposing it with real-world aircraft data. The top-level requirements are detailed in Table 2.1.

Parameter	Value	Unit
Harmonic range	926	[<i>nmi</i>]
Max payload	7500	[<i>kg</i>]
Cruise required MTOM fraction	0.95	[–]
Cruise Mach	0.41	[–]
Cruise altitude	7000	[<i>m</i>]
Take-off length	1315	[<i>m</i>]
Landing speed	58.13	[<i>m/s</i> ²]
Time to climb to FL170	17.5	[<i>min</i>]
Diversion range	185	[<i>km</i>]
Loiter time	30	[<i>min</i>]

Table 2.1: Top-level requirements of ATR-72 [32, 38, 39]

Table 2.2 presents the aircraft sizing result together with an aircraft geometry from the Initiator in Figure 2.5. It can be seen that the dimensions and weight are fairly matched. However, it is found that the horizontal tail ratio is significantly overestimated. This overestimated issue has been reported in Schouten et al. [40]. Although equipping the BLI propeller at the tailcone tip causes mass redistribution and shifts the center of gravity, the thesis objective does not include the investigation of aircraft stability. While the Initiator’s estimation error in horizontal tail size is acknowledged, it is deemed secondary to our core research goals.

Parameter	Reference	Initiator	Unit	Deviation (%)
MTOM	22.80	22.80	[t]	-0.14
OEM	13.45	13.35	[t]	-1.17
Wing span	27.05	27.06	[m]	0.02
Wing area	61.00	61.03	[m ²]	0.01
Fuselage length	27.20	27.52	[m]	1.16
Fuselage diameter	2.90	2.77	[m]	-4.46
Propeller diameter	3.90	3.85	[m]	-1.17
W/S	3662.95	3663.12	[N/m ²]	0.00
W/P _{gt}	0.0552	0.0530	[N/kW]	-4.06

Table 2.2: Parameter comparison between Initiator and real aircraft for ATR-72-600. Reference data is taken from [38, 39].

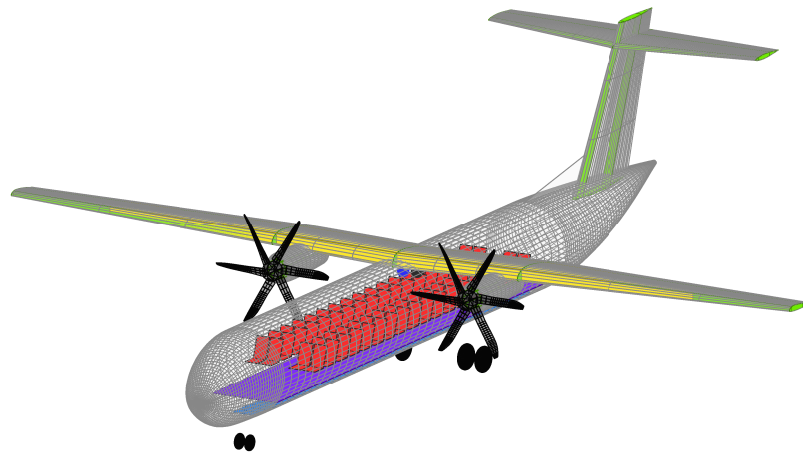


Figure 2.5: The geometry of ATR-72 reproduced from the Initiator

2.2. BOUNDARY LAYER INGESTION MODELING

This thesis explores the configuration of BLI propellers, which are electrically driven. The size of these propellers is determined by the diameter ratio (λ_p), which signifies the proportion of the propeller diameter to the fuselage diameter. The BLI model, developed by de Vries [18], is employed to assess power-saving benefits within the Initiator, as illustrated in Figure 2.6 .

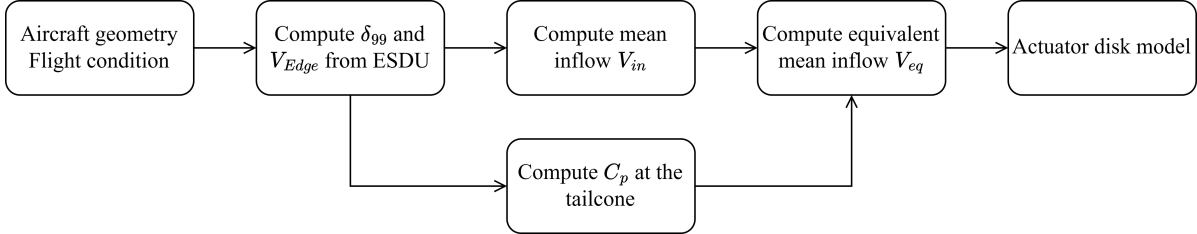


Figure 2.6: Workflow of the BLI model from the in-house report [18]

The fuselage geometry is characterized by the fuselage and tailcone slenderness ratio (λ_{fus} , λ_{tc}), and λ_p . Both λ_{fus} and λ_{tc} indicate the length-to-diameter ratio of the fuselage and tailcone. The BLI model uses data from ESDU [41, 42] to determine the boundary-layer thickness (δ_{99}) and edge velocity (V_{Edge}), based on the Reynolds number, λ_{fus} , and λ_{tc} . Moreover, δ_{99} and V_{Edge} further manipulate the given velocity profile (the orange vector in Figure 2.8) into the corresponding inflow for the BLI propeller.

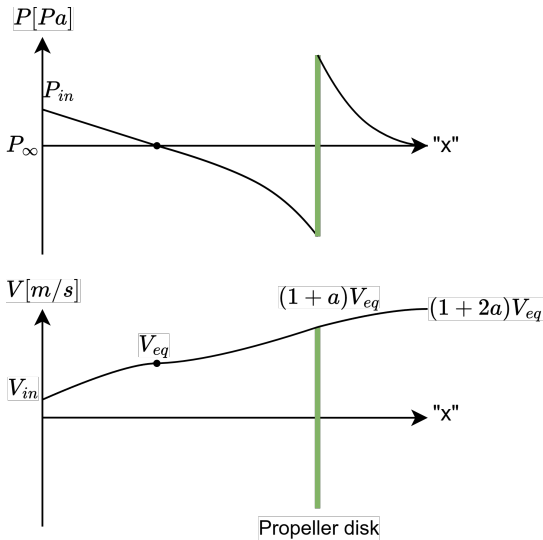


Figure 2.7: Equivalent flowfield for the uninstalled BLI propeller reproduced from [18].

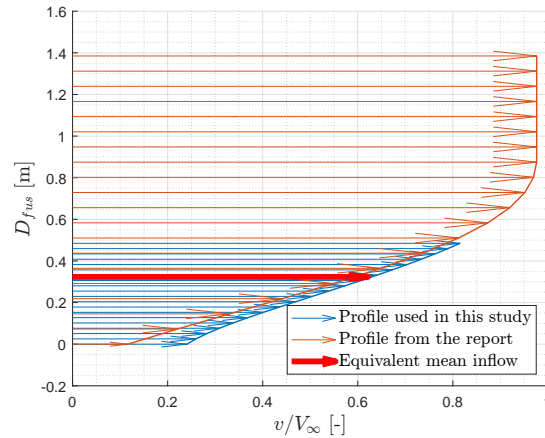


Figure 2.8: The demonstration of the velocity profile used in this study

In the existing BLI model, the BLI propeller is modeled as an uninstalled propeller operating in an equivalent flowfield, as shown in Figure 2.7, which accounts for pressure and velocity disturbances caused by the upstream axisymmetric fuselage [18]. The "x" denotes the fictitious coordinate in the equivalent flow field. Thus, additional velocity due to pressure expansion at the fuselage tail should be added to the inflow, resulting in the mean equivalent boundary layer velocity (V_{eq}), as shown in the thick red arrow in Figure 2.8. Consequently, the BLI propeller efficiency can be determined through the actuator disk theory.

It is worth noting that the use of an axisymmetric fuselage will potentially underestimate the required power for the BLI propeller, as mentioned in [subsection 1.1.3](#). However, the effect of tailcone upsweep angle remains neglected in the relatively low-fidelity estimation at the conceptual aircraft design stage. This effect should be considered in the later stage with a higher fidelity method and full aircraft optimization.

As mentioned at the beginning of this chapter, this thesis opts for the BET method to refine some assumptions in the actuator disk theory. Consequently, [Figure 2.9](#) presents the new approach replacing the actuator disk model and not using uniform mean quantities for the boundary layer. Instead, an example of the velocity profile used in the BET method is shown as a blue vector in [Figure 2.8](#). The BET method incorporates this boundary-layer inflow and can further determine the BLI propeller efficiency with the consideration of blade aerodynamics.

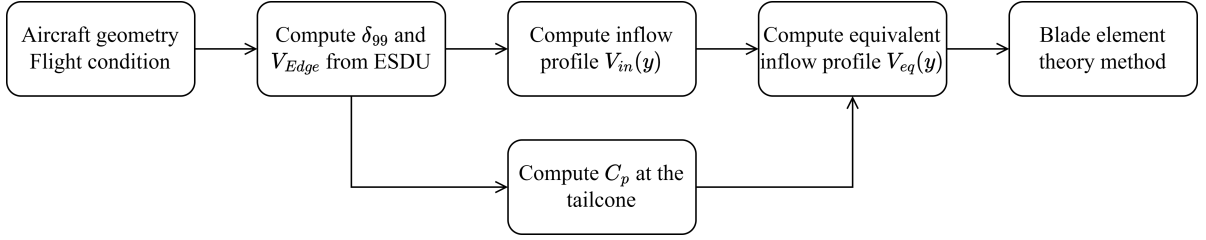


Figure 2.9: Workflow of the new approach to model the boundary layer profile

Despite these adjustments in the calculation of BLI propeller efficiency, the profile drag induced by BLI is commonly calculated by PBM. However, the kinetic energy rate-based analysis method requires the work produced by the velocity and pressure. The pressure data can be obtained through CFD simulation or wind tunnel experiments. [Figure 2.10](#) shows the control volume surrounding the fuselage-propulsor configuration. The power balance equation for this control volume can be expressed as [Equation 2.1](#). The left-hand side is the power inflow to the control volume, where P_s represents the shaft power, P_K represents the power to accelerate the fluid through the BLI propeller, and $F_X V_\infty$ is the power of streamwise net force. On the other hand, the right-hand side shows all power dissipation in the control volume.

$$P_s + P_K + F_X V_\infty = \Phi_{BL} + \Phi_{jet} + \Phi_{vortex} \quad (2.1)$$

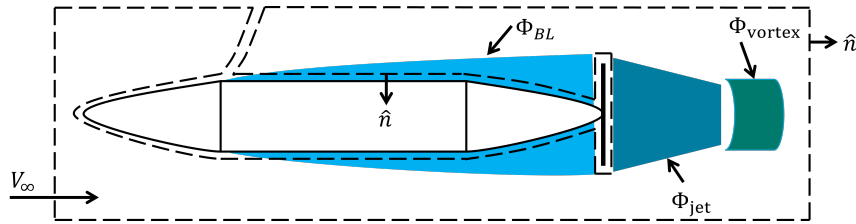


Figure 2.10: The control volume surrounds the bare fuselage with a propeller derived from [\[4, 14, 15\]](#).

However, P_K and Φ_{jet} require the pressure integral around the fuselage and in the slipstream. The modeling framework cannot obtain such data. Therefore, the change in profile drag due to BLI still lies on the actuator disk theory and V_{eq} .

According to the in-house report [\[18\]](#), BLI-induced profile drag focuses solely on the tailcone section, considering only static pressure and velocity changes caused by the actuator disk. The changes

of both quantities are again modeled in the equivalent flowfield by finding the difference between propeller on and off conditions. The flowfield of the propeller-off condition considers the bare fuselage, while the propeller-on condition imposes the induced velocity by the BLI propeller to that flowfield. Changes in skin friction drag over the inclined fuselage surface are assumed to be identical to those on the propeller axis. On the other hand, pressure drag changes can be determined by identifying pressure jumps at the actuator disk, a function of disk loading for the BLI propeller. Finally, the sum of skin friction and pressure drag changes provides the profile drag induced by BLI.

2.3. PROPELLER DESIGN

It has been decided to address the assumptions of uniform inflow and a propulsor disk in the actuator disk theory. Propeller performance is calculated using the BET method to enhance these aspects. The propeller design routine, as shown in [Figure 2.11](#), combines XFOIL and XROTOR, similar to the setup used by van Arnhem [\[43\]](#).

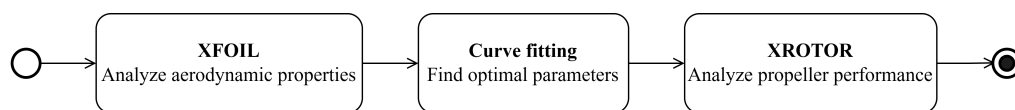


Figure 2.11: Workflow of the propeller design

XFOIL analyzes two-dimensional airfoil aerodynamic properties to calculate the induced velocity and force in the propeller analysis. However, the propeller experiences three-dimensional effects and strong Coriolis force, stabilizing the blade's boundary layer, resulting in a higher lift coefficient around a high angle of attack [\[44\]](#). The lift polar from XFOIL is, thus, corrected by the empirical method from Snel et al. [\[44\]](#). The local Reynolds number is calculated based on the effective inflow velocity, $\sqrt{(\Omega r)^2 + V^2}$, without considering the induced velocity. Since the induced velocity is a relatively small value, the effective inflow velocity still provides a reasonable approximation to the local Reynolds number.

The aerodynamic results from XFOIL serve as the basis for XROTOR to reconstruct the aerodynamic polar. As indicated in the XROTOR manual [\[45\]](#), the program uses the key aerodynamic parameters with parametric equations to build lift and drag polar for each blade section. [Table 2.3](#) presents all required key aerodynamic parameters for parametric equations. Moreover, XROTOR uses Prandtl-Glauert compressibility correction to account for the compressibility effect. This implies that the maximum effective tip velocity should be Mach 0.7, as the compressibility correction loses the validity beyond this value [\[46\]](#).

Parameter name	Symbol
Maximum lift coefficient	$C_{l,max}$
Minimum lift coefficient	$C_{l,min}$
Zero-lift angle of attack	α_0
Lift slope	C_{l_α}
Post-stall lift slope	$C_{l_{\alpha_{stall}}}$
Lift increment to stall	$C_{l_{stall}}$
Minimum drag coefficient	$C_{d,min}$
Lift coefficient at minimum drag coefficient	$C_{l,@C_{d,min}}$
Slope of drag coefficient with respect to lift coefficient squared	$\frac{\partial C_d}{\partial C_l^2}$
Reference Reynolds number	Re_{ref}
Critical Mach number	M_{crit}

Table 2.3: Required key aerodynamic parameters for XROTOR

Furthermore, XROTOR uses Equation 2.2 to model the drag rise due to compressibility effects. Drela [45] mentioned that this correction is based on drag rise behavior of representative NACA airfoils, which may not apply to exotic airfoils.

$$\Delta C_D = 10(M_{local} - M_{crit})^3 \quad (2.2)$$

Additionally, applying a curve fitting function to the aerodynamic data from XFOIL is essential due to the aerodynamic modeling method in XROTOR. The curve fitting process extracts the values of key aerodynamic parameters from XFOIL as an initial guess. The fitting function minimizes the least-squared error between raw aerodynamic data from XFOIL and the results from the parametric equation. Thus, the optimal key aerodynamic parameters can be determined. Figure 2.12 shows the combined effect of the curve fitting function and XROTOR's parametric equations. This example is a sectional airfoil near the propeller blade root. The curve of raw fit indicates that the polar is recreated in XROTOR without the curve fitting process. In contrast, the curve fitting function results in the optimal fit. The lift coefficient within the linear range can be approximated fairly well. Therefore, the curve fitting ensures that the reconstructed polar in XROTOR is nearly identical to the one from XFOIL.

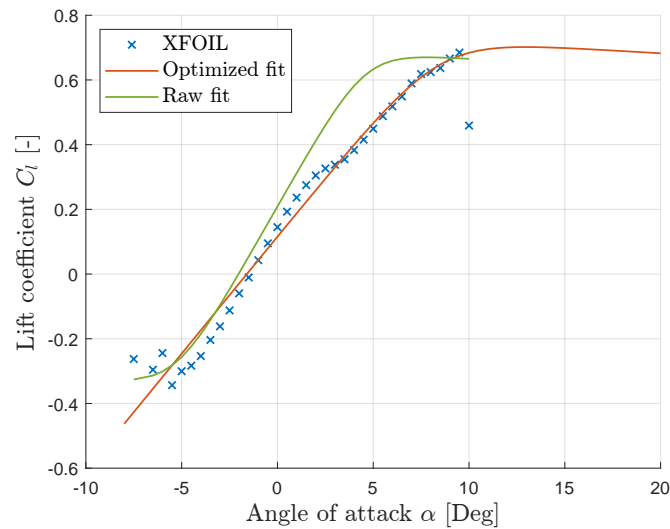


Figure 2.12: Comparison between different aerodynamic polar and data from XFOIL

XROTOR employs the lifting-line theory to analyze propeller blade flowfield, as outlined by Drela [45]. In this approach, a bound vortex characterizes each propeller blade section along the quarter-chord line. As the bound vortex sheds downstream, it creates induced velocity in both axial and tangential directions. The resulting vortex sheet, along with its components in the axial and tangential directions, is illustrated in Figure 2.13.

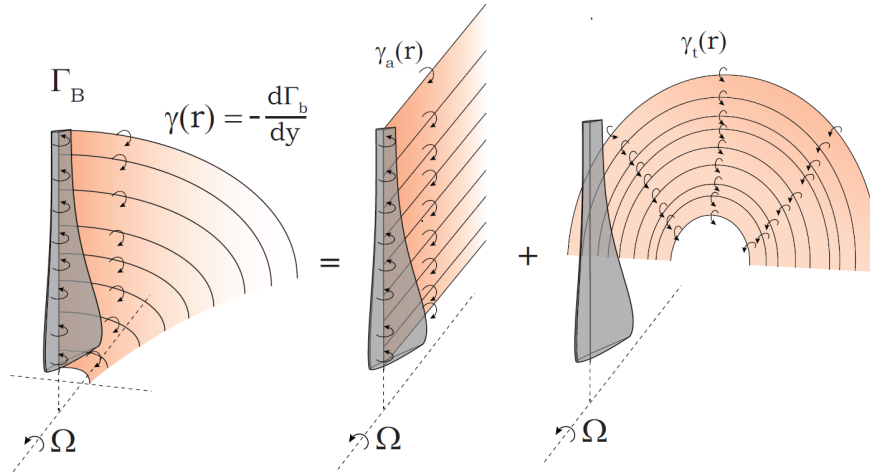


Figure 2.13: The lifting-line representation of the propeller from van Arnhem [43]

In this illustration, it is evident that the axial free vortex, denoted as γ_a , leads to the tangential induced velocity (swirl) component, while the tangential free vortex, γ_t , contributes to the axial induced velocity component. Moreover, the lifting-line theory incorporates the influence of free vortices on the circulation of the bound vortex. This means that adjacent sectional airfoils interact with each other. Consequently, the lifting-line code effectively models the neighboring effects among sections in the calculation of propeller performance.

Furthermore, XROTOR possesses the capability to analyze the ingestion of incoming slipstream into the propeller [45]. This feature makes XROTOR a suitable tool for solving boundary-layer ingestion problems.

2.3.1. VALIDATION OF PROPELLER DESIGN

The validation result shows differences between the propeller design routine and the wind tunnel test. Li et al. [47] provide a validation case that performs an analysis with a sweep of advance ratio at a low-speed wind tunnel. According to their experimental setup, the freestream velocity is 29 m/s with a turbulence level of 0.5%. The propeller geometry of XPROP has six blades with a diameter of 0.4046 meters and a 30-degree pitch angle at 70% blade radius [47].

Moreover, the free transition with $N_{crit} = 4.25$ is used in XFOIL to simulate the turbulence level in the wind tunnel experiment. The final results of thrust coefficient (C_T), torque coefficient (C_Q), and propeller efficiency (η_p) are shown in Figure 2.14a to Figure 2.14c. The maximum error for these three quantities are 8.4%, 8.6%, and 4%, respectively. Additionally, Figure 2.14d compares the curve fitting and raw aerodynamic data. The curve fitting is generated from XROTOR's aerodynamic parametric equations. The quadratic fitting curve shows a significant error margin at different lift coefficients. This result indicates the limitation of XROTOR in determining the required power at different radial positions. The airfoil at the propeller outboard has more camber than the inboard. Therefore, the reconstructed polar in XROTOR might not be representative and further overestimate the required power.

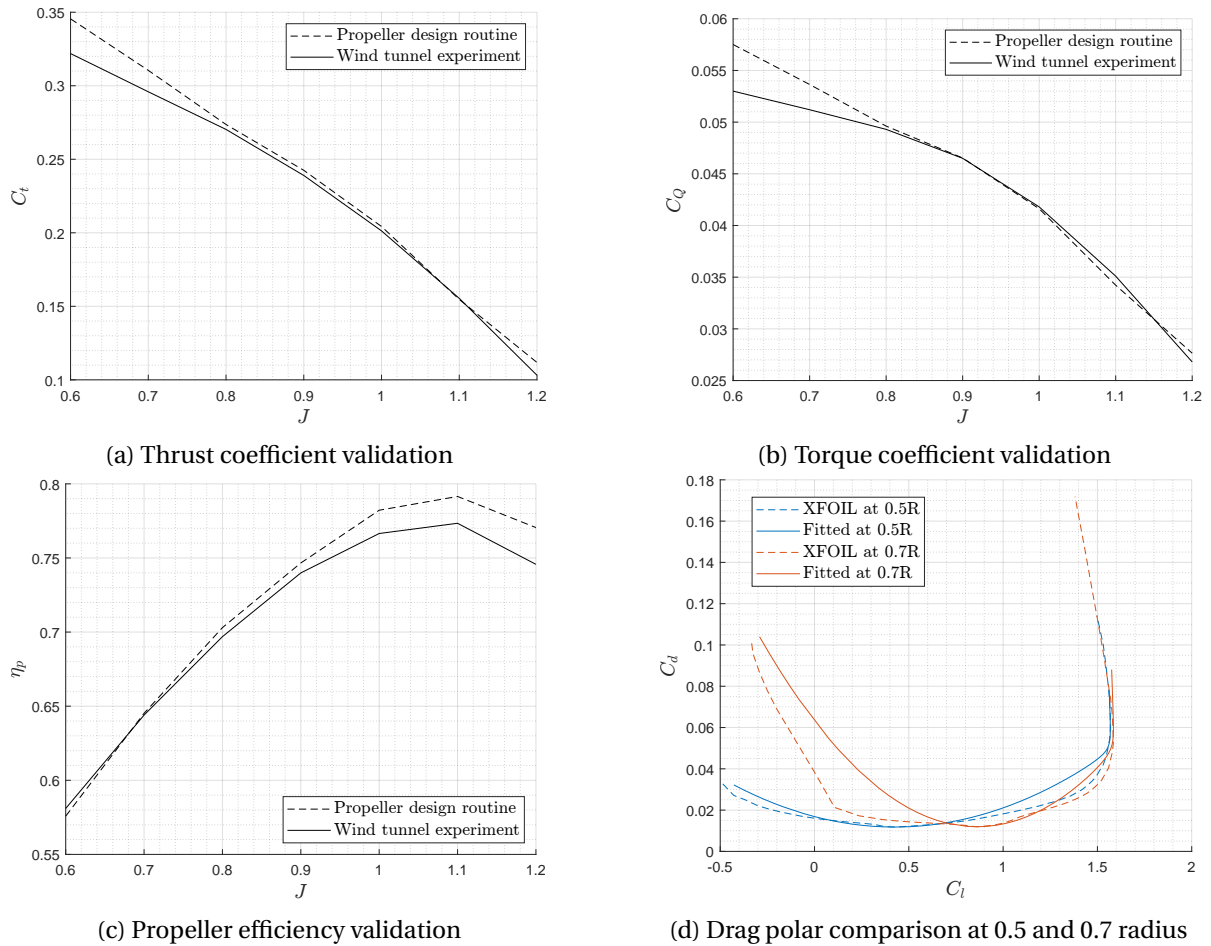


Figure 2.14: Propeller performance (a) to (c), and the lift-to-drag polar comparison (d).

The over-prediction in C_t and C_Q is observed at a lower advance ratio, which has been indicated in several studies [43, 48]. This could be several reasons:

1. XROTOR does not include the viscous effect in the slipstream. The vortex structure in the slipstream will dissipate in reality.
2. The radial flow over the blade is not captured by XROTOR. However, the vortices shed from the blade create the radial flow close to the trailing edge [43], causing a thicker boundary layer over the blade.
3. The N_{crit} value affects the transition point on the airfoil, and the transition point might not be the same as the one of the wind tunnel test.
4. The aerodynamic coefficient fitting function based on aerodynamic equations in XROTOR predicts a slightly higher C_l and C_{l_α} value.
5. The nacelle and spinner in the wind tunnel test might cause the blockage effect to accelerate the incoming flow and increase the advance ratio in reality. Thus, the thrust and torque are smaller.

This study will avoid the low advance ratio region because of the limit of compressibility correction. The range of advance ratio is discussed in detail in [section 2.5](#). Therefore, the propeller design routine gives reasonable predictions of the propeller performance.

2.4. PROPELLER OPTIMIZATION

As necessary approaches for modeling the boundary-layer profile and analyzing the propeller performance with the BET method have been discussed, the propeller optimization for the boundary-layer profile can be built. The optimization utilizes MATLAB optimizer *fmincon* with a gradient-based algorithm. Although the gradient-based algorithm may not be able to find the global minimum in the design space, the convergence speed is faster than other algorithms, such as the genetic algorithm. The optimization minimizes the distance between the theoretical maximum η_p in BLI and obtained η_p . Moreover, the objective is subject to a required thrust force. Thus, a higher value of η_p can be translated into a lower required shaft power for the BLI propeller. The objective function is present in Equation 2.3.

$$\text{minimize } f(x) = (2 - \eta_p(x)) \quad \text{such that } \begin{cases} c(x) \leq 0 \\ \text{lower bound} \leq x \leq \text{upper bound} \end{cases} \quad (2.3)$$

The optimization loop is presented in Figure 2.15 and starts with an initial guess of propeller geometry taken from XPROP, which represents a propeller of typical regional turboprop aircraft [47].

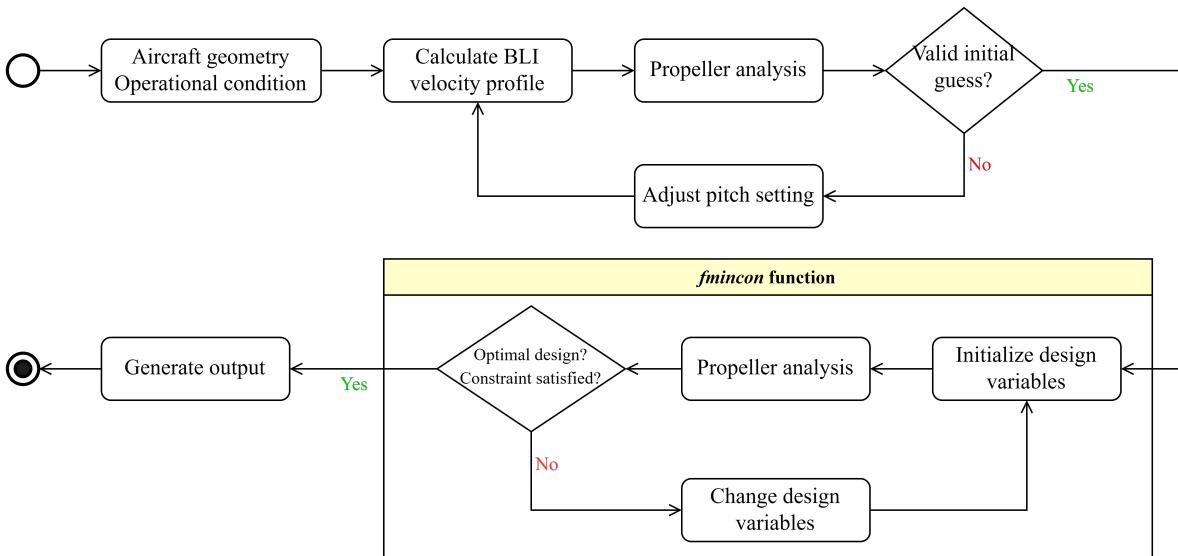


Figure 2.15: Propeller optimization loop

The propeller geometry is characterized by twist distribution, chord distribution, and propeller radius. The radius is a given input, further discussed in section 2.5. Thus, the optimizer changes the twist and chord distribution of the propeller blade through a parameterization method. The Class-Shape Transformation (CST) method from Kulfan [49] describes the twist and chord distribution over the blade. Equation 2.4 shows the general expression for the CST method, which was originally used to parameterize the shape of an airfoil. Coefficients of the class function (N_1 and N_2) determine the general shape of the distribution. Moreover, it is found that three Bernstein coefficients (A) adequately modify the general shape of distribution to describe the chord and twist distribution, respectively. ψ can represent either the twist or chord values, while $\Delta\xi$ represents the twist angle or chord length at the tip.

$$\zeta = (\psi)^{N_1} (1 - \psi)^{N_2} \sum_{i=1}^n A_i S_i(\psi) + \psi \Delta\xi \quad (2.4)$$

There are 10 design variables in the design vector x . The lower and upper bounds of all design variables are shown in Table 2.4. Bounds are set for the twist and chord to prevent the *fmincon* function from exploring the design space, where tip loss is significant, or the local angle of attack between the stall, leading to unrealistic designs.

Variable name	Symbol	Lower bound	Upper bound
Chord CST coefficient	$A_{1,c}$	0.05	1.8
Chord CST coefficient	$A_{2,c}$	0.05	1.8
Chord CST coefficient	$A_{3,c}$	0.05	1.8
Twist CST coefficient	$A_{1,\beta}$	0.3	1.5
Twist CST coefficient	$A_{2,\beta}$	0.3	1.5
Twist CST coefficient	$A_{3,\beta}$	0.3	1.5
Chord N_2 coefficient	$N_{2,c}$	0.5	1
Twist N_1 coefficient	$N_{1,\beta}$	1	0.5
Tip chord	c_{tip}	0.04	0.1
Tip twist	β_{tip}	0.4	1

Table 2.4: Bounds for design variables. All values in this table is not normalized.

Figure 2.16 presents the chord and twist distribution for the initial propeller geometry. This figure shows that with three CST coefficients, the chord and twist distribution can be described by Equation 2.4 and evaluated by the optimizer.

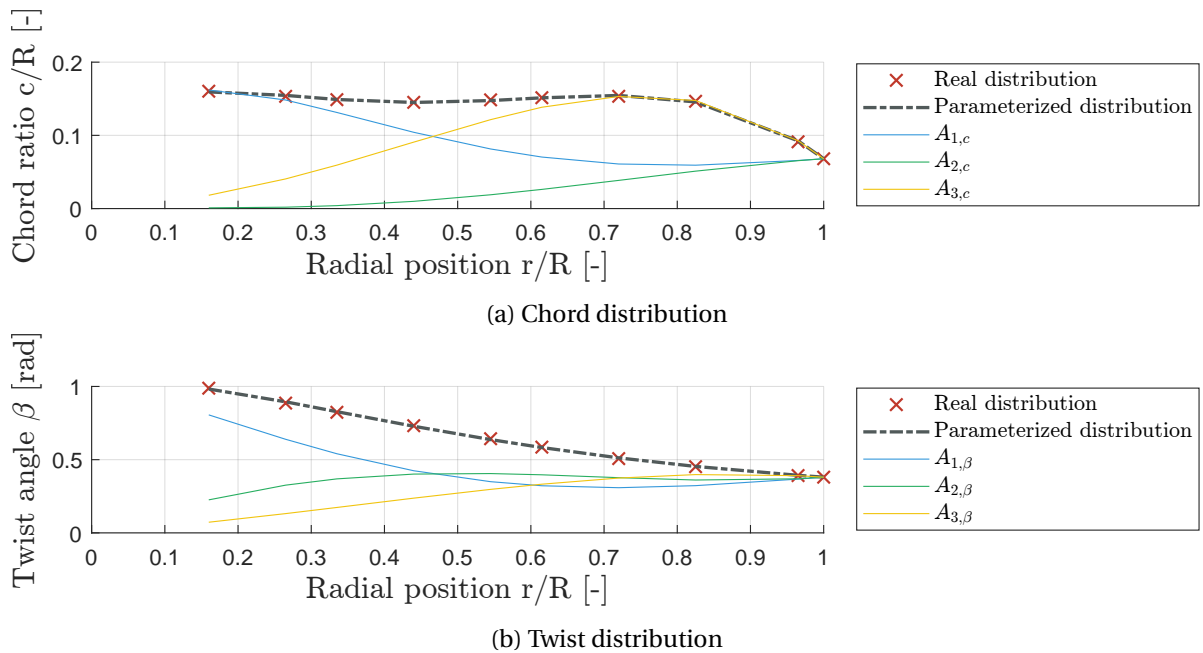


Figure 2.16: The chord and twist distribution of the blade described by the CST method

Additionally, several constraints are implemented to ensure the optimizer does not diverge during the optimization. The inequality constraint guarantees that the thrust produced by the optimized BLI propeller geometry can meet the required thrust force. A 5% error margin is implemented on this requirement. Thus, the inequality constraints are shown in Equation 2.5.

$$\begin{aligned}
c(x)_1 &= T_{required} - T_{produced} \\
c(x)_2 &= \frac{T_{produced}}{T_{required}} - 1.05
\end{aligned} \tag{2.5}$$

Moreover, the constraints on the BLI propeller geometry and blade aerodynamic characteristics need to be satisfied:

1. The blade sectional lift coefficient has to be in the positive and linear range, given that the optimal lift-to-drag ratio is in this range.
2. The thrust and power should not be Not a Number (NaN) since XROTOR can still converge with a negative local angle of attack on the blade.
3. Both XFOIL and XROTOR have to converge during the optimization.

Suppose any of the conditions mentioned above cannot be met in the optimization. In that case, the program will return NaN to the objective function and constraints, so the optimizer will try different settings in the design space.

However, there are some cases where all constraints cannot be satisfied, and the bounds for all design variables must be adjusted. For a small BLI propeller generating a high thrust force, the optimizer sometimes traps into a design point that any change in twist or chord distribution cannot retrieve a real value for the objective function. Due to the nature of the gradient-based algorithm, which evaluates the gradient between current and previous values of the objective function, the optimizer tends to increase twist CST coefficients to increase the produced thrust to obtain the steepest gradient. However, this will easily violate the constraint of the local lift coefficient staying within the linear range. Thus, the optimizer will eventually reach an infeasible design point. Consequently, the bounds of design variables must be fine-tuned for some cases.

It is important to acknowledge that the design loop has some limitations:

1. The determination of propeller blade number

The *fmincon* function explores various twist and chord distributions while ensuring the thrust constraint is met. However, some propeller sizes cannot meet the required thrust. For instance, the required thrust force may be too high for a small propeller or too low for a large one. To address this issue, the number of blades needs to be adjusted.

The baseline number of blades is six because of the initial geometry from XPROP. The ratio between the available thrust force of the initial geometry and the required thrust force determines the change in the number of blades. If this ratio exceeds 1.5 or below 0.5, the blade number will be adjusted by two. It is found that adding or removing two blades to the initial geometry can accelerate the convergence time. Moreover, this design setting decreases the chance that the optimizer cannot find a feasible design to satisfy the constraint, excessively using high twist angles. However, this setting potentially introduces the design bias to the optimization because the number of blades is not a design variable. Thus, the optimizer does not evaluate the impact of different numbers of blades, which could influence the final chord length and twist angle.

2. Unswept propeller blade design

The BLI propeller blade design does not include the sweep angle as the design variable. The current framework utilizes the lifting-line code in blade element theory, which has a limitation in designing a propeller with a sweep angle.

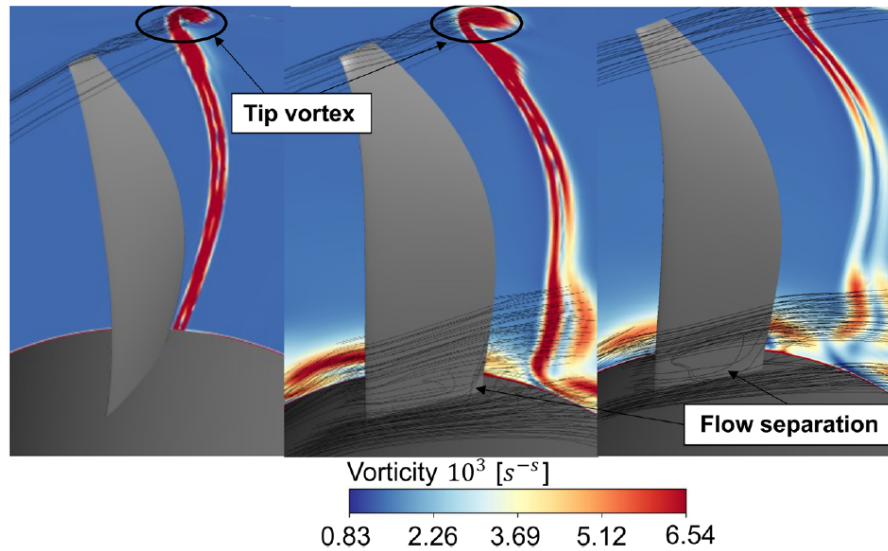


Figure 2.17: BLI propeller design with forward swept and lean angle from Costa et al. [50]

However, with high-fidelity methods and full analysis, the propeller can generate more thrust force with a lower required power. The study from Costa et al. [50] designed a BLI propeller operating at Mach 0.47 with a forward swept angle and lean angle to reduce the flow separation on the blade surface as shown in Figure 2.17. This design framework involves meshing, CFD, and genetic algorithm optimization to optimize the propeller and account for the three-dimensional flow effect on the blade.

3. Unoptimized airfoil shape for BLI

The study on BLI propeller optimization conducted by van Arnhem [43] not only involves changing the twist and chord distribution over the blade but also includes the sectional airfoil shape as a design variable. However, this thesis does not focus on optimizing airfoil shape due to the computational cost, as there are numerous BLI propeller optimization cases to be run, which will be elaborated in section 2.5. The initial geometry for the optimization is taken from XPROP, which is designed for freestream ingestion conditions. The unoptimized airfoil may not be suitable for a non-uniform inflow across the blade. Nevertheless, it is worth mentioning that modifying the twist and chord distribution can still lead to some improvements in achieving the optimal design. The trade-off here is to strike a balance between the computational cost and the optimal solution.

2.5. SURROGATE MODEL

This thesis investigates the aircraft performance affected by BLI, which entails the BLI propeller design in conceptual aircraft sizing. As introduced in [section 2.1](#), the Initiator consists of different sizing modules and intensively evaluates the BLI effect during the design iteration. However, a single BLI propeller optimization can take up to an hour to design and analyze the propeller. This challenge suggests that the direct interaction between the BLI propeller optimization and the Initiator is extremely computationally expensive. Therefore, an alternative approach is necessary to incorporate the BLI effect in the conceptual aircraft sizing.

This thesis proposes a surrogate model as a solution. A surrogate model is a cheap-to-run analytical model that characterizes the input-output behavior of a complex system [51, 52]. In this thesis, the complex system is the assessment of power-saving benefits due to BLI. Design of Experiment (DoE) is then used to build the surrogate model by choosing the number of data points in the design space. Moreover, a suitable data regression method can approximate the available data points to create the response surface, a process known as Response Surface Methodology (RSM). As a result, the surrogate model can generate the output during the conceptual aircraft design process within a second.

2.5.1. SURROGATE MODEL DURING THE CRUISE

The input variables of the surrogate model, called independent variables, are identified and organized by the DoE approach. Independent variables for DoE with different levels per variable are shown in [Table 2.5](#). The number of levels decides the number of sample points within the bound uniformly. The dependent variable of the surrogate model is the change in propeller efficiency due to BLI, denoted as $\Delta\eta_p$. Thus, the relation between independent and dependent variables can be described as [Equation 2.6](#). For the sake of reducing the total convergence time, a cruise flight speed of Mach 0.41 and an altitude of 7000 meters have been selected in the BLI propeller optimization, which is identical to the reference aircraft.

Independent variable	Symbol	Lower Bound	Upper Bound	Level
Fuselage Slenderness Ratio	λ_{fus}	8	12	5
Tailcone Slenderness Ratio	λ_{tc}	2.4	4	3
Propeller Diameter Ratio	λ_p	0.3	0.8	4
Advance Ratio	J	1.8	2.5	3
Equivalent thrust Coefficient	$T_{c,eq}$	0.01	0.5	4

Table 2.5: Independent variables for DoE, the bound refers to Roskam [53]

$$\Delta\eta_p = SM(\lambda_{fus}, \lambda_{tc}, \lambda_p, J, T_{c,eq}) \quad (2.6)$$

[Figure 2.18](#) displays the setup for creating dependent variables with different combinations of independent variables in DoE. To evaluate the aero-propulsive benefits of BLI, a freestream propeller with XPROP's geometry and the same operating conditions as BLI cases is analyzed. The propeller pitch setting is adjusted to generate the same required thrust as the BLI propeller. Thus, $\Delta\eta_p$ can be determined by subtracting η_p from BLI and freestream conditions.

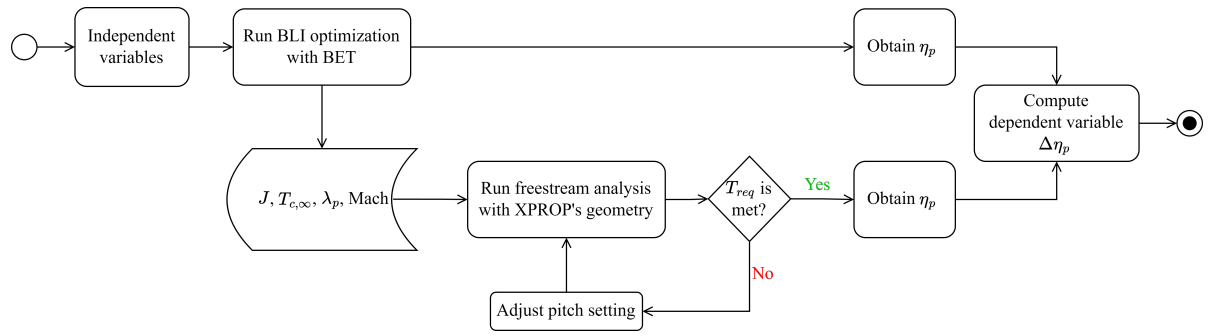


Figure 2.18: The setup of building data points for the surrogate model

As the second research question aims to assess the impact of fuselage and propeller geometric parameters, λ_{fus} and λ_p have more points compared to other parameters. Moreover, a preliminary sensitivity study over independent variables shows that the change of λ_p and $T_{c,eq}$ significantly affects $\Delta\eta_p$, which requires more points to cover the design space. Furthermore, it is worth highlighting that in this DoE, $T_{c,eq}$ represents the thrust coefficient normalized by V_{eq} because the propeller operates within the boundary layer.

It is essential to underscore that the value of variable J is pre-defined within this framework. The determination of J is a result of the conceptual aircraft design process, where factors such as flight speed, propeller size, and an initial estimate of rotational speed come into play. As part of the design iteration in the Initiator, the rotational speed is adjusted based on the effective tip Mach constraint to ensure the validity of the compressibility correction. Over the course of this iterative process, the value of J converges to a constant. Consequently, in DoE for optimizing the BLI propeller geometry, J is a known parameter, and the rotational speed becomes an outcome of the propeller optimization. However, the propeller optimization is then limited to seeking the most optimal twist and chord distribution to satisfy the required thrust without evaluating other advance ratios. Consequently, the propeller might not operate at the maximum efficiency line in the $\eta_p - J$ plot.

Factorial designs are a well-established experimental design in DoE for assessing the joint effects of multiple independent variables on dependent variables [54]. Nevertheless, the application of a full-factorial design is often hindered by its time-consuming and computationally expensive nature. Thus, to address this issue, a multi-level fractional-factorial design is used instead, which reduces the number of data points while still capturing the main interactions.

However, it is crucial to acknowledge that this design approach lacks the benefit of randomization, a feature provided by methods such as Latin hypercube sampling (LHS). LHS ensures a more even distribution of data points throughout the design space, as discussed in studies by McKay et al. [55] and Myers et al. [54]. Figure 2.19 illustrates the distribution of data points within two independent variables and the dependent variable using a fractional-factorial design.

Notably, the speed of convergence, as detailed in section 2.4, must be taken into consideration. Additionally, certain combinations of independent variables are filtered out to comply with the local tip Mach constraint, maintaining the integrity of the compressibility correction. Given these considerations, a fractional-factorial design is selected to strike a balance between the number of data points and computational cost

The response surface can be created after gathering all data points in DoE, which consists of 370 data points. The coefficient of determination (R^2) is a common method to inspect the accuracy of regression, which indicates the reduction in the variability of predicted output [54]. A larger value of R^2 indicates a response surface has better numerical prediction quality. 90% of data points in DoE are randomly selected as training points, while the remaining 10% are utilized as testing points to

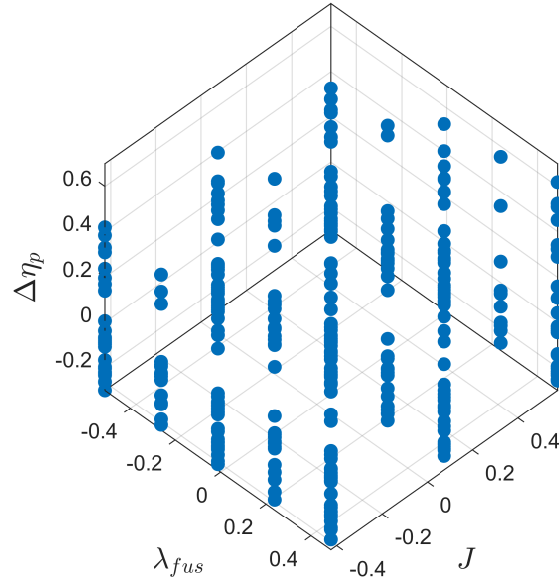


Figure 2.19: Demonstration of the data distribution with two independent variables (λ_{fus} , J) and the dependent variable ($\Delta\eta_p$). Values of data point are normalized.

assess the quality of the regression. Additionally, 23 validation points are interspersed between data point intervals for cross-validation, selected systematically and randomly.

An N-dimensional polynomial regression is initially employed to predict the output ($\Delta\eta_p$). Despite achieving a high R^2 value with a 2- or 3-degree polynomial, indicating a strong predictive capability over the given DoE, only 4 out of 23 validation points are accurately predicted. This suggests that the N-dimensional polynomial regression may not be suitable for this DoE.

Instead, the multivariate radial basis function (RBF) interpolation provides more accurate predictions over the validation points. The description of RBF is provided in [Appendix A](#). Carr et al. [56] noted that the polyharmonic type of RBF is well-suited for interpolating scattered data, even in large data-free areas. As presented in [Figure 2.19](#), there are many data-free areas between sets of independent variables. The final settings for the smoothing parameter (c) and degree of polynomial (N) for RBF are set at 0.01 and 2, respectively.

Lastly, due to propeller design constraints, there are limits to $T_{c,eq}$ for different λ_p . After observing response surface validation, the final lower and upper bounds of $T_{c,eq}$ for different λ_p are established.

2.5.2. LOOKUP TABLE DURING OTHER FLIGHT PHASES

The previously mentioned surrogate model is only valid for the cruise condition, while other flight phases can also utilize the BLI propeller. A lookup table method for other flight phases is implemented to resolve the surrogate model's limitations. [Figure 2.20](#) describes the procedure to create the lookup table.

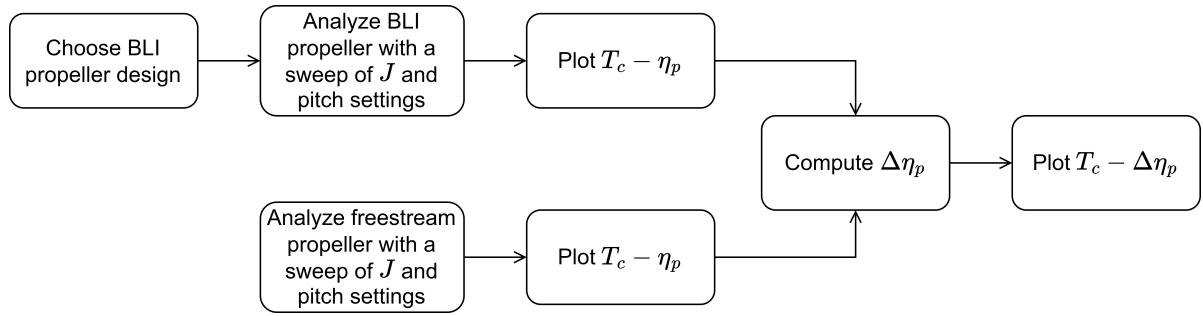


Figure 2.20: The procedure of creating the lookup table

Different propeller sizes with the highest and lowest designed disk loading are analyzed to obtain the $T_c - \eta_p$ plot. [Figure 2.21](#) shows the analysis results from one of the propeller sizes. It can be seen that the low-speed boundary layer provides the benefit of power-saving when both propellers generate the same thrust force. Each data point in [Figure 2.21](#) corresponds to a combination of J and propeller pitch setting (β). As mentioned at the beginning of [section 2.2](#), the propeller is driven by the electrical motor, providing the variable rotational speed by changing the frequency of the voltage supply. Moreover, the propeller pitch angle is assumed to be variable. As a result, a $T_c - \eta_p$ plot presents the propeller performance under different disk loading. In this way, $\Delta\eta_p$ can be obtained for different λ_p and corresponding designed disk loading under different $T_{c,\infty}$.

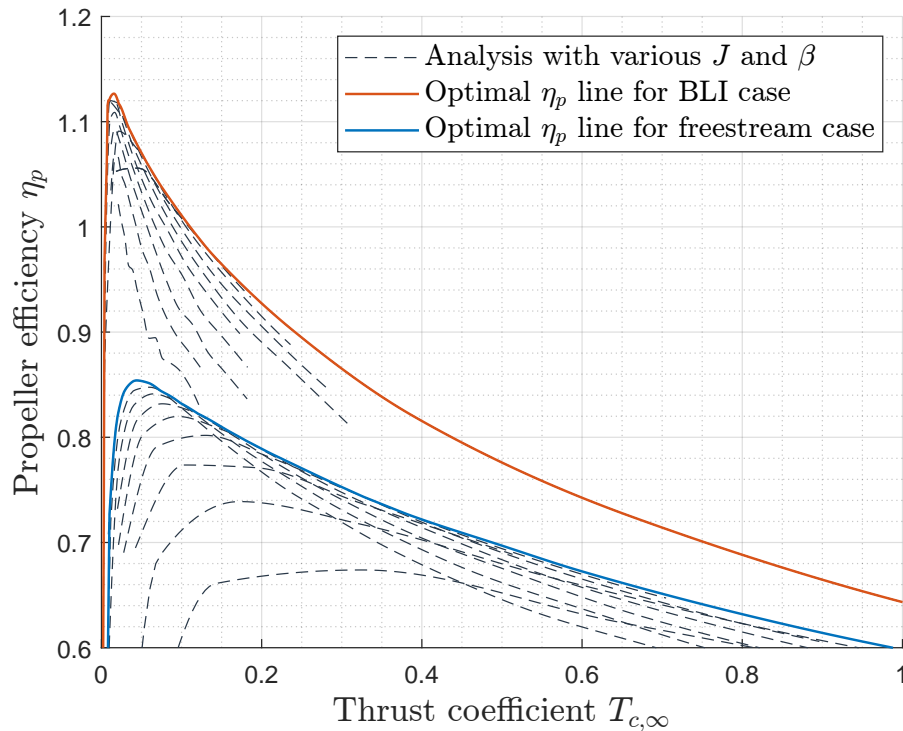


Figure 2.21: Demonstration of the $T_c - \eta_p$ plot. The analysis case is with λ_p of 0.63 with light designed disk loading.

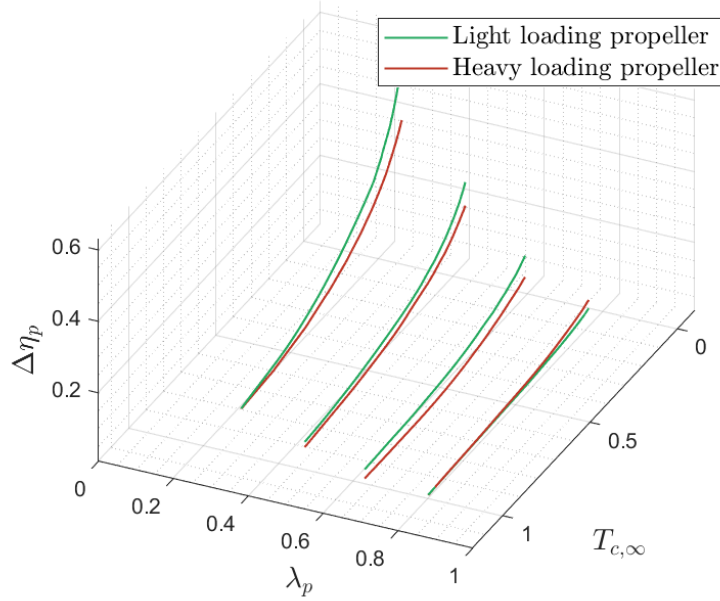


Figure 2.22: The lookup table with all propeller sizes

However, the over-speed issue with the effective Mach number is found when $T_{c,\infty}$ is lower than 0.08 for most propeller designs. More propeller performance details below $T_{c,\infty}$ of 0.08 require fine data points, which becomes computationally expensive. In this framework, it is decided to set 0.08 as the lower bound for the disk loading in the lookup table. Finally, with the workflow and condition mentioned above, [Figure 2.22](#) presents the final result for all propeller sizes and designed disk loading, and [Equation 2.7](#) describes the relation of all variables.

$$\Delta\eta_p = LUT(\lambda_p, T_{c,des}, T_{c,\infty}) \quad (2.7)$$

An observation can be made from [Figure 2.22](#) is that the propeller intended for light loading in the boundary layer has a higher $\Delta\eta_p$ compared to the one designed for heavy loading. Moreover, as $T_{c,\infty}$ increases, the propeller performance decreases, especially for the small propeller. $T_{c,\infty}$ is correlated to J with freestream velocity and propeller diameter. With the same propeller size, the increase in $T_{c,\infty}$ implies the decrease in freestream velocity, resulting in a lower J and the local inflow velocity. Although the low local inflow velocity decreases the Reynolds number, it is essential to note that the transition point over the local blade section is fixed at 0.05 chord length from the leading edge to simulate a fully turbulent boundary layer. This setup results in a higher drag coefficient at the low Reynolds number, decreasing the power-saving benefit towards the high thrust coefficient region. However, the propeller designed for light loading with a large diameter has a different trend than other propellers. This could be because less blade number is used for the light-loading propeller, as a large diameter can easily produce an excessive thrust force. However, this setup could cause the optimizer to converge with a longer blade chord, resulting in fewer power-saving benefits. Therefore, the propeller designed for light loading is below the heavy loading.

Additionally, this analysis ignores the change in density and temperature due to different altitudes for two reasons:

1. The sensitivity of propeller performance to the Reynolds number effect is negligible in this analysis. The propeller size and operational speed are relatively large, resulting in a high

Reynolds number. Thus, the turbulent boundary layer is dominant, and the change in friction coefficient is insignificant in this region.

2. Although the effect of Mach number affects the blade sectional aerodynamic polar, the propeller design is limited to not surpass Mach 0.7 locally due to the compressibility correction, which has been mentioned in [section 2.3](#).

The final lookup table is created by N-dimensional polynomial regression with a degree of 3, which gives a R^2 value of 0.9989. Moreover, 100 additional random points are used to validate data-free regions.

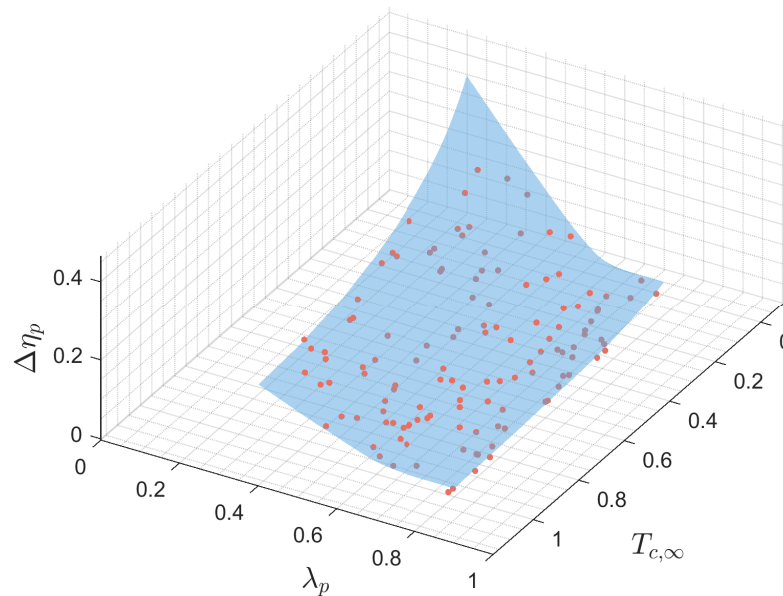


Figure 2.23: Example of surface created by different propeller sizes with scattered validation points.

The propeller designed for different loading can generate two surfaces as upper and lower limits, respectively. [Figure 2.23](#) shows an example with the surface created by the light-loading propeller in [Figure 2.22](#) with 100 validation points. The same validation workflow applies to both surfaces. [Figure 2.24a](#) shows the distribution of validation points with an average error of 4.7% on the surface of the light-loading propeller. Furthermore, [Figure 2.24b](#) presents the surface of a heavy-loading propeller with an average error of 5.8%. The similar outcome from both validation cases indicates that a higher deviation occurs between λ_p of 0.6 to 0.8. In this region, the deviation of the predicted result can be up to 50%. A high deviation is due to two surfaces crossing each other in that region, which makes the regression hard to predict $\Delta\eta_p$ accurately. However, the average regression error outside that region is less than 5%, which indicates that the regression still provides certain accuracy. Therefore, avoiding the large-propeller region when using the lookup table in the aircraft design process is advised.

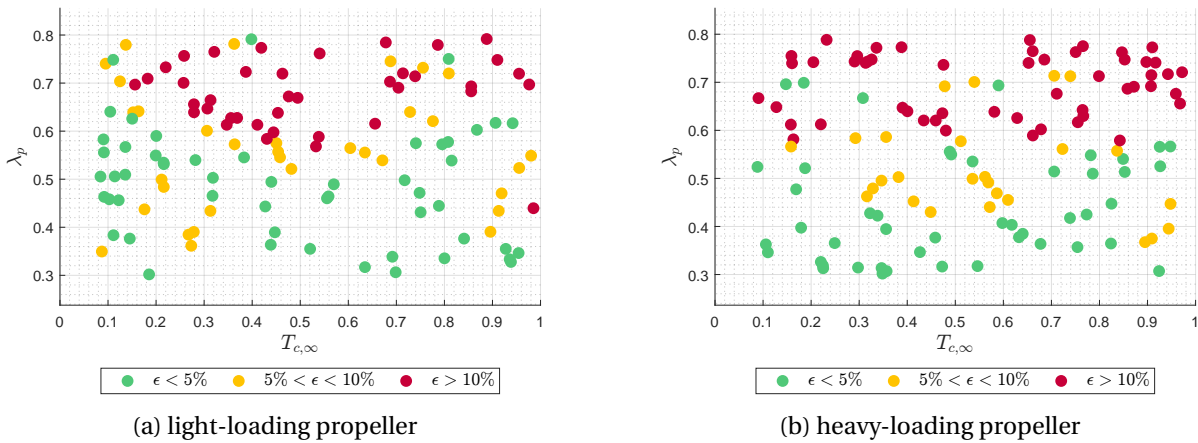


Figure 2.24: Scattered validation points on different surfaces

2.6. INTEGRATION OF THE SURROGATE MODEL

The development of the surrogate model assessing the power-saving benefit of the BLI propeller is discussed before this section. As mentioned earlier in section 2.5, the surrogate model is a solution for the conceptual aircraft design to incorporate the influence of the BLI propeller.

The integration of the BLI surrogate model requires modification in the Initiator, particularly in the constraint analysis and mission analysis. These two analysis modules play different roles in the conceptual aircraft sizing process:

1. The constraint analysis assesses the relative significance of selected aircraft performance parameters on the design [57]. It is the first step in the design process to determine wing loading (W/S) and power loading (W/P) for different flight conditions, such as takeoff, cruise, climb, and landing, to meet the design requirements. Figure 2.25 shows an example of the constraint diagram from the Initiator. The gray area indicates the feasible design space that those combinations of power and wing loading can satisfy all design constraints.

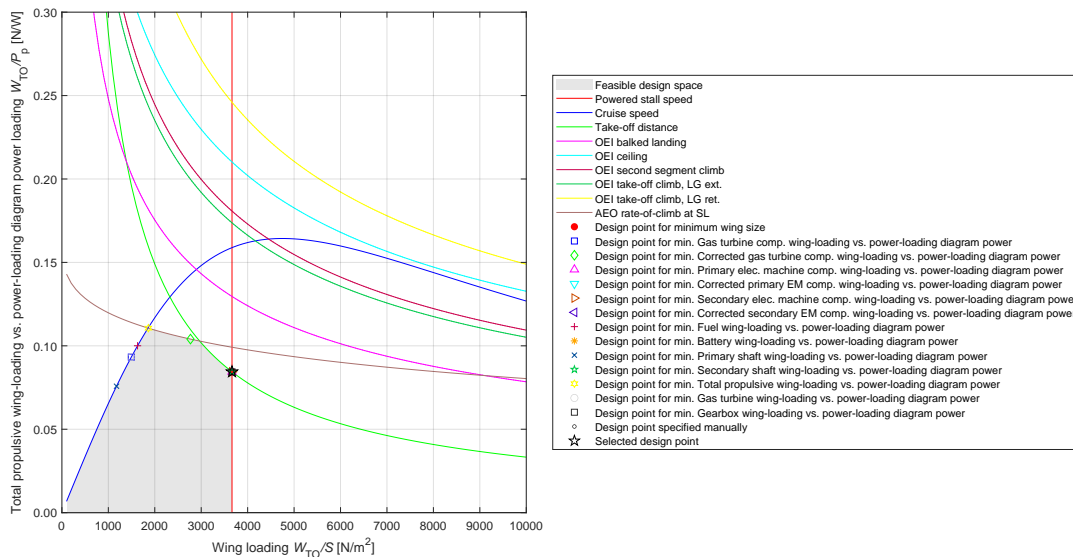


Figure 2.25: Constraint diagram generated by the Initiator

The constraint diagram is constructed by solving the hybrid-electric constraint equations out-

lined in de Vries et al. [29] The design point indicates the required power and wing area for a given weight. In this thesis, the design point is the minimum wing area.

2. The mission analysis accounts for the flight mission profile and an initial guess of aircraft mass. A numerical quasi-steady point model is implemented in the Initiator to size the energy requirement with small time intervals [29].

Weight estimation modules will further determine the aircraft mass, and the constraint and mission analysis will be updated. In both analysis modules, the aero-propulsive benefit from the BLI propeller is included, influencing the required power and energy at the design point.

Each unique combination of independent variables in the surrogate model represents one BLI propeller design. The cruise constraint will be calculated first in the constraint analysis, in which the BLI propeller will be determined. Once the BLI propeller is known, the design disk loading can be obtained accordingly. The rest of the constraint in Figure 2.25 can utilize the lookup table with the required disk loading to retrieve $\Delta\eta_p$ to obtain the power-saving benefit from the BLI propeller. Eventually, the required power includes the impact of BLI.

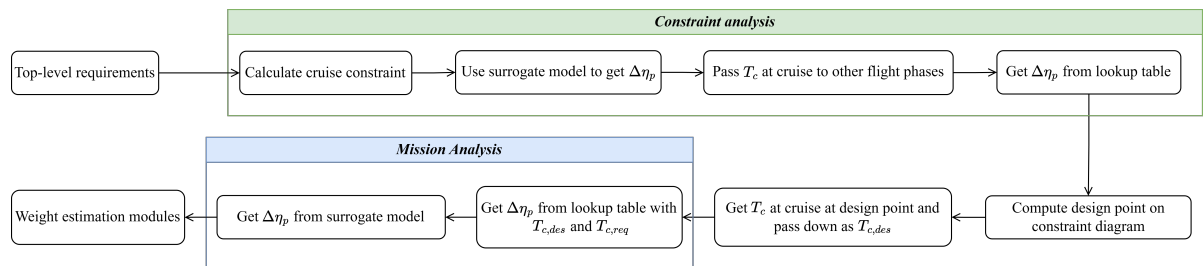


Figure 2.26: Workflow of integration part of the surrogate model

Figure 2.26 presents the workflow of how the surrogate model and lookup table are integrated into the Initiator. In the first few iterations, the required thrust coefficient during the cruise in the constraint and mission analysis has different values. The initial guess of aircraft mass is used in the mission analysis, leading to a different disk loading for the BLI propeller. This difference implies that the chosen BLI propellers are different in constraint and mission analysis. Moreover, more sophisticated weight estimation methods evaluate the aircraft mass in detail. As the Initiator uses an iterative process to size the aircraft, the aircraft mass from the previous iteration is used as the initial guess in the next iteration. Eventually, the aircraft mass will converge, and both analysis modules will result in an identical required disk loading for the BLI propeller.

In conclusion, the integration of all statistical models with the conceptual aircraft sizing can be summarized in Figure 2.27. This is a higher-level perspective of the detail described in Figure 2.26 and corresponds to the flow chart in section 2.1 that both constraint and mission analyses include the aero-propulsive effect during the conceptual aircraft sizing.

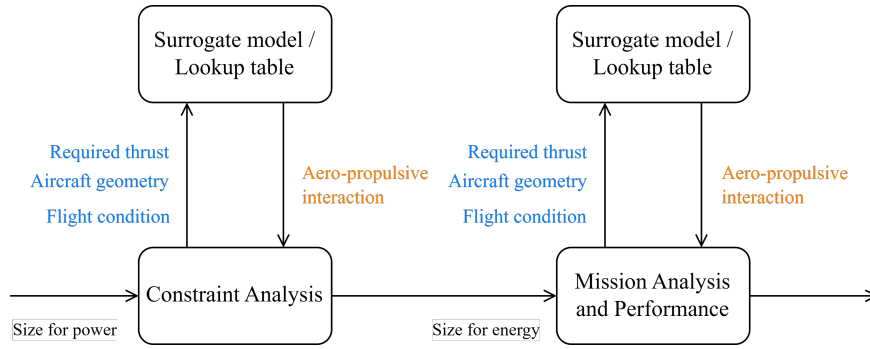


Figure 2.27: Integration of the propeller-level surrogate model with the conceptual aircraft sizing loop

2.7. POWERTRAIN MODELING

The hybrid-electric powertrain utilized in the Initiator aircraft follows the framework proposed by de Vries et al. [29]. While powertrains incorporating batteries, such as the SPPH powertrain, are available options for supplying power to the BLI propeller, their feasibility is hampered by the substantial weight penalty incurred due to the low power density of the battery. Consequently, this thesis narrows its focus to the PTE powertrain, as depicted in Figure 2.28.

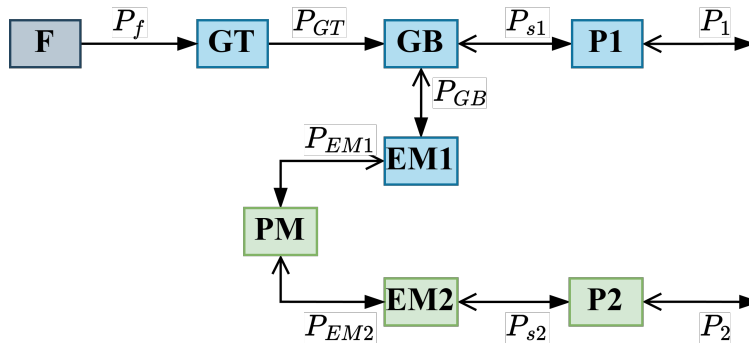


Figure 2.28: The PTE architecture adapted from [29]. Blue components belong to the primary propulsion system, and green components belong to the secondary propulsion system.

The following abbreviations are used to identify each component:

1. **GT** for Gas Turbine
2. **GB** for Gear Box
3. **BAT** for Battery
4. **EM** for Electric Motor / Generator
5. **PM** for Power Management
6. **P** for Propulsor

Additional power control parameters (PcP) are required to account for the electrical propulsion system. The shaft-power ratio (ϕ) is used to quantify the power allocation between the primary propulsion system (P_{s1}) and the secondary propulsion system (P_{s2}) as described in Equation 2.8 [29]. In this thesis, the primary propulsion system refers to wing-mounted propellers, while the secondary

propulsion system refers to the BLI propulsor. The value of ϕ can further translate into the thrust share between underwing propellers and the BLI propeller.

$$\phi = \frac{P_{s2}}{P_{s1} + P_{s2}} \quad (2.8)$$

The required power for each component in the powertrain sizing can be found by solving a system of equations, which involves the power flow, component efficiency, and power control parameter [29]. The hypothetical technology level for all electrical components is presented in Table 2.6, which refers to the near-term scenario in Hoogreef et al. [32]. The electric drivetrain represents a simplified powertrain modeling approach from de Vries et al. [34]. This approach treats the specific power of all electrical components as a combined value, including the generator (\mathbf{EM}_1), motor (\mathbf{EM}_2), inverter, and rectifier. An additional 30% weight penalty accounts for the thermal and power management system.

Component	Symbol	Value	Unit
Electric drivetrain	ESP	3.7	[kW/kg]
Generator / motor	η_{EM}	0.95	[-]
Gearbox	η_{GB}	0.95	[-]
Power management system	η_{PM}	1	[-]
Gas turbine	η_{GT}	0.42	[-]

Table 2.6: Electrical powertrain component technology assumption in this thesis, values of efficiency refers to Bonnin and Hoogreef [33].

2.8. AIRCRAFT-LEVEL KEY PERFORMANCE INDICATORS

In the field of HEA design, various KPIs are employed to evaluate the aircraft's performance. The performance indicators in this thesis refer to the hybrid-electric aircraft studies [29, 32, 33] and account for the characteristics of BLI. The following is an enumeration of the KPIs considered:

1. **Payload Range Energy Efficiency (PREE):** As proposed by Bijewitz et al. [28] for HEA, PREE serves as a measure of the transport system's efficiency. It quantifies how effectively energy is utilized per joule in a given mission ($E_{mission}$), considering the payload weight (W_{PL}) and range (R). The formula for PREE is expressed as:

$$PREE = \frac{W_{PL} \cdot R}{E_{mission}} \quad (2.9)$$

2. **Aircraft Mass Group:** This encompasses aircraft-level mass parameters, including Maximum Takeoff Mass (MTOM), Operational Empty Mass (OEM), and Fuel Mass (FM).
3. **Propulsion System Mass:** This category includes the mass associated with the electric propulsion system, generator, and electrical motor.
4. **Wing Area (S):** This metric evaluates the combined effects of the additional hybrid-electric powertrain and BLI propeller.
5. **Change of Aircraft Profile Drag at Cruise ($\Delta C_{D0, cruise}$):** This KPI is employed to assess the aerodynamic impact resulting from the BLI propeller.
6. **Change of Propeller Efficiency ($\Delta \eta_p$):** It is used to evaluate the power-saving benefits stemming from BLI.

All these KPIs are subjected to the analysis concerning specific aircraft design parameters, including:

1. Fuselage slenderness ratio, λ_{fus}
2. Propeller size ratio, λ_p
3. Shaft-power ratio, ϕ

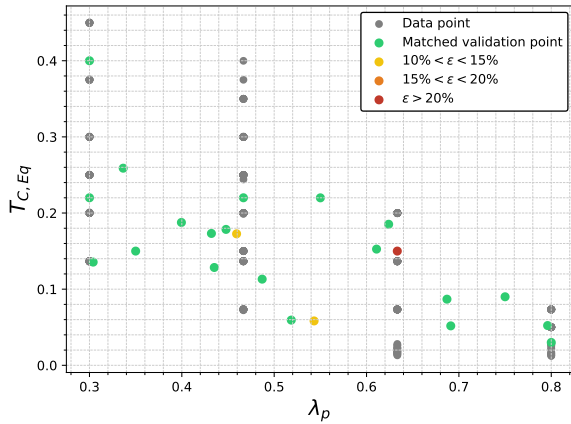
3

RESULT AND DISCUSSION

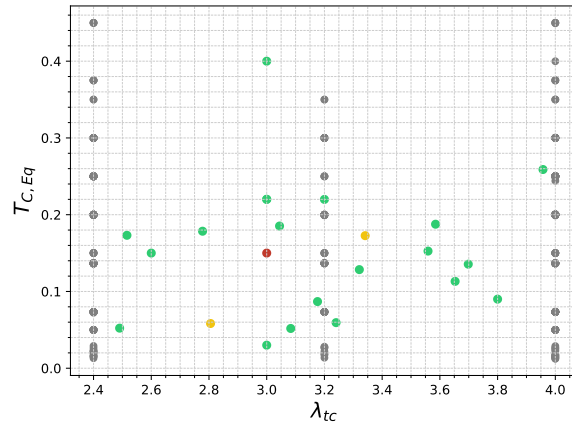
3.1. RELIABILITY OF THE RESPONSE SURFACE

The RBF regression method achieves an R^2 value of 0.9765 with an average deviation of 0.11%. However, the average maximum deviation is 14.7%, indicating potential high deviations in certain areas of the response surface. As de Vries [58] suggested, such large deviations could be due to outliers in input variables or improper distribution of data points on the response surface. The final error threshold for assessing prediction quality is set at 10%. Furthermore, 20 out of 23 validation points are matched with an average error of 3.44%, leading to the construction of the surrogate model using RBF interpolation. The RBF regression method provides a better interpolation ability than a pure polynomial regression for scattered data with a large data-free area.

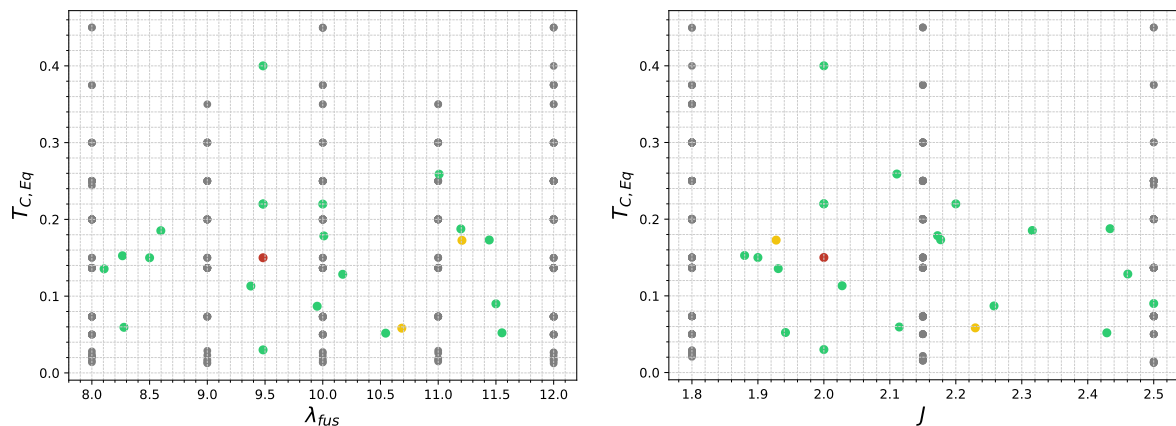
The validation of the response surface is depicted in Figure 3.1. All independent variables are plotted with respect to $T_{c,eq}$. The color gradation in all figures symbolizes the varying degrees of error margins between the predicted values derived from the surrogate model and actual values. A green dot signifies an error margin of less than 10%, indicative of an acceptable prediction. A yellow dot, signifying an error margin between 10% to 15%, implies that the surrogate model fails to provide an accurate prediction for those specific combinations of independent variables. Lastly, a red dot indicates an error margin exceeding 20%, rendering the prediction from the surrogate model negligible. By checking these validation points across the bounds of independent variables, regions with higher prediction accuracy for the dependent variable can be identified.



(a) Distribution of propeller size ratio.



(b) Distribution of tailcone slenderness ratio.



(c) Distribution of fuselage slenderness ratio.

(d) Distribution of advance ratio.

Figure 3.1: Four different independent variables versus the equivalent thrust coefficient.

Most of the cases can be predicted well except for three points. The error of two yellow dots are 11.7% and 11.3%, respectively. The red dot shows a 21% error from the actual simulation result. This discrepancy may be primarily attributed to the distribution of design points, which appears to substantially influence regression quality. Thus, avoiding these areas when using in the aircraft sizing process is suggested since the surrogate model may fail to predict $\Delta\eta_p$. The pattern of scattered data is due to the nature of factorial design, in which no randomization is involved. A further investigation of different regression methods is suggested to improve the reliability of the surrogate model.

Unswept blade design and tip Mach constraint limit achievable thrust force for each propeller size, as can be seen in Figure 3.1a that the disk loading decreases from a small to large propeller. Thus, the final bounds of the equivalent thrust coefficient vary for each propeller size. Combining with the observation from the response surface validation in Figure 3.1, Table 3.1 shows lower and upper bounds for the equivalent thrust coefficient at different propeller size ratios. The aircraft geometry from the Initiator sizing process will be checked to ensure the equivalent thrust coefficient lies within the bounds.

λ_p	Lower bounds	Upper bounds
0.3	0.14	0.45
0.47	0.073	0.39
0.63	0.013	0.2
0.8	0.012	0.07

Table 3.1: Lower and upper bounds of thrust coefficients for different propellers.

3.2. COMPARISON BETWEEN ACTUATOR DISK AND SURROGATE MODELS

The predicted $\Delta\eta_p$ from the surrogate model compares to the calculated result from the actuator disk model in this section. The baseline for the comparison is set as the median of all design variables, which is presented in Table 3.2. In order to investigate the sensitivity of $\Delta\eta_p$ to each design variable and compare results from both models, each design variable is changed by $\pm 10\%$.

λ_{fus}	λ_{tc}	λ_p	J	$T_{c,eq}$
10	3.2	0.45	2.15	0.244

Table 3.2: Baseline design variables

Figure 3.2 shows $\Delta\eta_p$ estimated by the surrogate and actuator disk models. The x-axis shows which variable is changed per time from the baseline. At first glance, both models give a similar trend in $\Delta\eta_p$. The power-saving benefit is increased for high λ_{fus} and λ_{tc} but small λ_p . On the contrary, a power-saving benefit is lower when J increases. It is important to note that the actuator disk model does not consider J because the propeller is modeled solely as a disk with a change in momentum across it. In contrast, J impacts the real propeller as it alters the rotational speed.

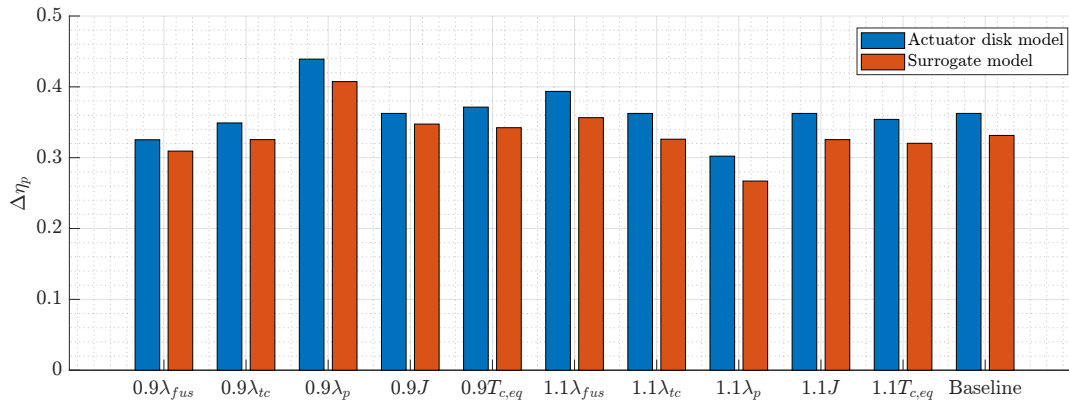


Figure 3.2: Comparison between estimated value from the actuator disk model and surrogate model.

A lower J results in a smaller inflow angle but a higher effective inflow velocity to the local blade section. The propeller has to generate the required thrust, and thus, the optimizer tends to satisfy this constraint by decreasing the local angle of attack and chord length. On the other hand, a higher J results in a higher inflow angle but slower effective inflow velocity. Instead, the optimizer increases the local angle of attack and chord length to generate a required thrust. Therefore, a higher J yields a lower $\Delta\eta_p$.

Moreover, the required thrust also impacts the power-saving benefit. It can be observed that a higher required $T_{c,eq}$ results in a lower $\Delta\eta_p$. The optimizer tries to satisfy the thrust constraint while searching for the highest η_p , yielding a longer blade chord or higher angle of attack. Therefore, the drag on local blade sections increases and deteriorates the eventual power-saving benefit.

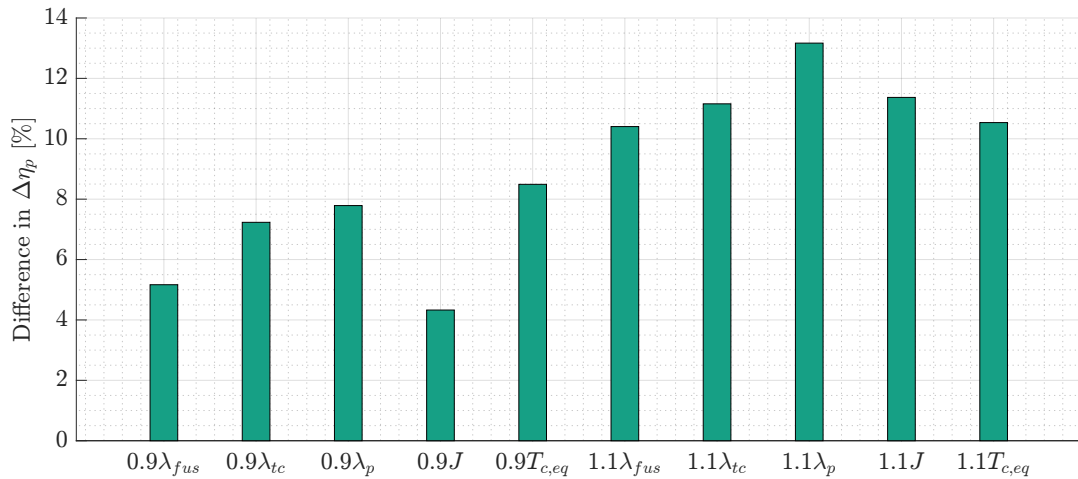


Figure 3.3: Difference in $\Delta\eta_p$ between actuator disk model and surrogate model.

The difference between estimated values from both models is presented in Figure 3.3. All changes in design variables indicate that the actuator disk model gives a higher power-saving benefit than the surrogate model. In particular, the actuator disk model yields a 13% higher $\Delta\eta_p$ at $1.1\lambda_p$, again indicating the significance of accounting for the propeller blade aerodynamic.

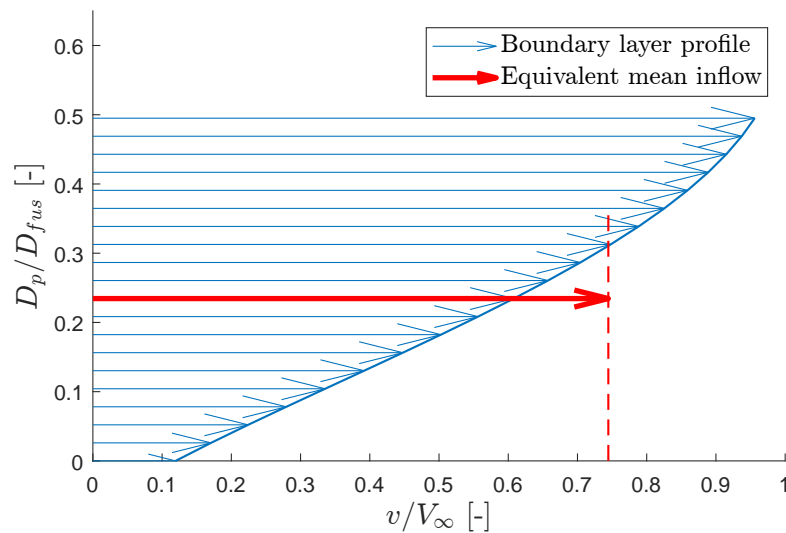


Figure 3.4: Velocity profile in two models when λ_p is 10% higher than the baseline.

A larger propeller ingests more high-speed inflow than a small propeller, yet this impact might not be captured by the actuator disk model. This is shown in Figure 3.4, which displays two different boundary layer velocity profiles used in the actuator disk and surrogate models. The equivalent mean inflow profile demonstrates the assumption of the actuator disk model, indicating that a portion of high-speed inflow is underestimated. On the contrary, since the surrogate model is based on propeller blade analysis code, the higher inflow velocity at the blade outboard region increases the drag force and, ultimately, the required power. It is worth mentioning that the airfoil shape is not a part of optimization as mentioned in section 2.4, which potentially further increases the required power. Thus, the surrogate model predicts less power-saving benefits than the actuator disk model due to the boundary layer modeling and the propeller design.

3.3. CONCEPTUAL HYBRID-ELECTRIC AIRCRAFT RESULTS

This section presents the results from the conceptual aircraft design with the proposed methodology. [subsection 3.3.1](#) presents and analyzes the impact of incorporating the hybrid-electric powertrain with the BLI propeller on the reference ATR-72 aircraft. Moreover, the sensitivity study is investigated in [subsection 3.3.2](#) to discuss the impact of different aircraft design parameters on aircraft-level performance and answer the second research question. Furthermore, [subsection 3.3.3](#) will show further research on the powertrain setting to answer the third research question. Finally, in [subsection 3.3.4](#), a complete propeller optimization case is presented to suggest the direction for improving the surrogate model.

3.3.1. COMPARISON BETWEEN BASELINE RADICAL DESIGN AND REFERENCE DESIGN

The radical design's baseline incorporates a PTE powertrain and uses the BLI propeller, which provides 20% of the total shaft power during the cruise. The propeller size is 45% of the fuselage diameter. The hybrid-electric powertrain and additional propulsion system impact several aircraft KPIs, as shown in [Table 3.3](#). It is immediately evident that the overall weight increases and aligns with the trend from past research. However, the fuel weight does not agree with conclusions from some joint programs, such as STARC-ABL and CENTRELIN. Instead of gaining some percentages of drop in fuel consumption, the baseline radical design needs more fuel than the reference aircraft, resulting in a lower PREE. The aero-propulsive benefit of exploiting the boundary layer is not reflected in the aircraft level. The same observation is also found in Bonnin and Hoogreef [33] that radical technology brings only second-order influence on aircraft-level performance.

KPI	Conventional	Radical baseline	Unit	change in [%]
MTOM	22.80	24.13	[t]	5.87
OEM	13.35	14.43	[t]	8.13
FM	1.95	2.20	[t]	12.93
Wing mass	2.22	2.39	[t]	7.51
Propulsion system mass	2.22	2.80	[t]	26.14
Wing area	61.03	64.63	[m ²]	5.90
PREE	1.16	1.03	[-]	-11.54

Table 3.3: Aircraft KPIs comparison between reference design and baseline radical design

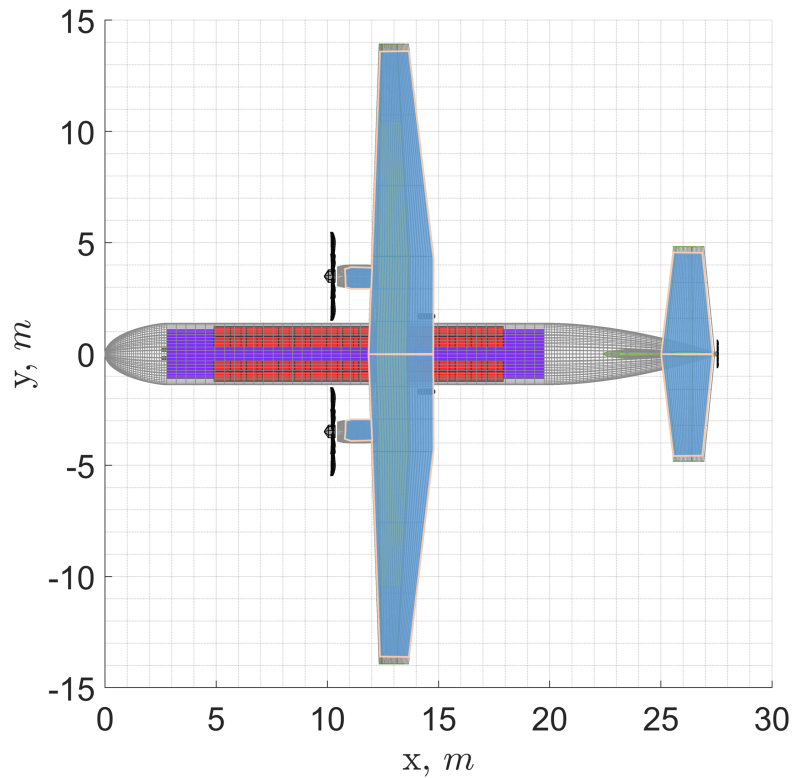
The power-saving benefit from the BLI propeller does not reduce the fuel weight can be attributed to several reasons:

1. From the perspective of propeller aerodynamics, the study only utilizes the unducted propeller, which poses more loss around the propeller tip than the ducted fan.
2. The surrogate model accounts for blade aerodynamic effect which shows a lower $\Delta\eta_p$, and it has been discussed in [section 3.2](#).
3. The propeller blade airfoil is not optimized for a given boundary layer, potentially increasing the drag and further translating to the required shaft power.
4. From the aircraft design perspective, the final design from the Initiator is the converged design, which only focuses on the design feasibility but not optimization. The interaction between subsystems may impact the fuel consumption for a mission.

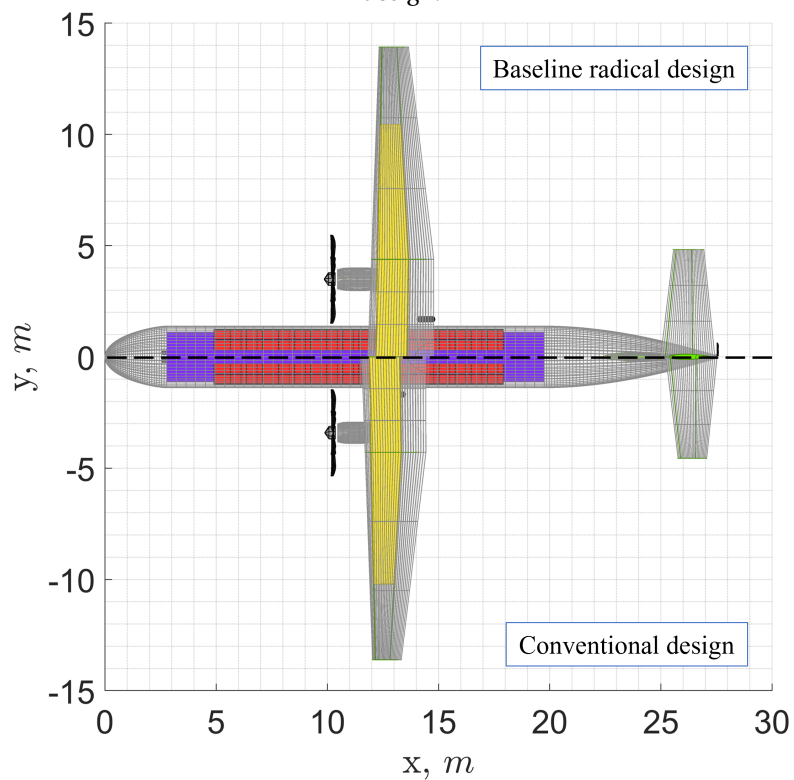
[Figure 3.5](#) illustrates the geometric modifications resulting from the integration of a hybrid-electric powertrain and the BLI propeller in the conceptual aircraft design. The blue shadow in [Figure 3.5a](#)

represents the conventional reference design. Several noteworthy observations can be drawn from these comparisons:

1. In comparison to the baseline radical design, [Figure 3.5a](#) shows that the wing area of the conventional design has been enlarged, as indicated in [Table 3.3](#), to support the increased weight of the aircraft during cruising. Additionally, the wing span has been extended to adhere to the aspect ratio constraint.
2. Due to the addition of the powertrain and the BLI propeller at the tailcone tip, as depicted in [Figure 3.5b](#), the wing position has been shifted further aft from its leading edge when compared to the conventional design.
3. To counterbalance the change in the wing position, it has been necessary to increase the size of the horizontal tail. This adjustment ensures an adequate moment of force, thereby maintaining the aircraft's pitch control.
4. The increased shaft power required for the BLI propeller has led to a rise in the mass of the generator, necessitating an expansion of the nacelle size to accommodate this larger propulsion component, as shown in [Figure 3.5a](#).
5. The redistribution of mass within the aircraft has also influenced the position of the main landing gear, causing it to shift towards the wing's trailing edge.



(a) The dimension comparison of wing, horizontal tail, and turbine. The blue shadow area indicates the dimension of the conventional design.



(b) The layout comparison between baseline radical design and conventional design.

Figure 3.5: Comparison of aircraft geometry in a top-view perspective, generated from the Initiator

Additionally, the cruise altitude remains constant for all aircraft designs throughout this thesis. In reality, the aircraft gradually increases the flight altitude during the cruise to maintain the optimal lift-to-drag ratio. Moreover, de Vries et al. [29] suggested that optimal cruise altitudes may vary between conventional and radical designs due to changes in wing loading. However, the primary focus is to examine the impact of several aircraft design parameters and BLI effects on aircraft KPIs, which do not alter the wing loading. Consequently, the decision is made to keep the cruise altitude unchanged for all aircraft sizing in this thesis.

3.3.2. SENSITIVITY OF AIRCRAFT-LEVEL KPIs TO DESIGN PARAMETERS

Three critical aircraft design parameters influence the power-saving benefits of boundary layer ingestion. Firstly, λ_{fus} affects the development of the velocity profile. Secondly, λ_p determines the proportion of the boundary layer flow that can be ingested. Lastly, ϕ controls the thrust distribution between the primary propulsion system and the BLI propeller. More than 30 radical designs were generated to explore how changes in design parameters such as λ_{fus} , λ_p , and ϕ can impact KPIs for aircraft. However, due to the limitations of the surrogate model, some designs were found to be meaningless. Therefore, this section only presents and analyzes a subset of the generated radical designs.

Figure 3.6 displays how aircraft-level KPIs respond to changes in aircraft design parameters, including discussions on how BLI effects influence these KPIs from different perspectives.

Several observations can be made in Figure 3.6a and Figure 3.6b as below:

1. **Change of λ_{fus} :** At first glance over Figure 3.6a and Figure 3.6b, the change of λ_{fus} gives the most significant impact on the aircraft mass. The OEM and wing mass change can be attributed to a snowball effect from a longer or shorter fuselage, which further impacts the fuel mass and consequent MTOM. Furthermore, PREE shows a noticeable change because it is highly tied to the fuel mass, as the aircraft range and payload mass are constant in this study. A longer fuselage length results in a slower boundary layer inflow to the BLI propeller, theoretically leading to more power savings. However, the increase in aircraft weight outweighs this impact.
2. **Change of ϕ :** As ϕ increases, more power is supplied to the BLI propeller, which in turn requires more thrust from it. Generating more thrust through BLI can theoretically reduce the required power and thus decrease the aircraft mass. However, a higher value of ϕ increases the mass of the propulsion system mass, and the cyclic weight penalty again offsets any gain from the BLI propeller. Further investigation of the mass change down to the system level can provide more insight into this result.
3. **Change of λ_p :** The change of λ_p has an insignificant impact on the aircraft mass, which gives less than 1% of change from the baseline. The pure aero-propulsive effect does not impact the aircraft-level performance.

In general, λ_{fus} plays the dominant role in analyzing the sensitivity of aircraft-level KPIs. Moreover, the impact of the aero-propulsive effect due to BLI is not visible at the aircraft-level mass KPIs.

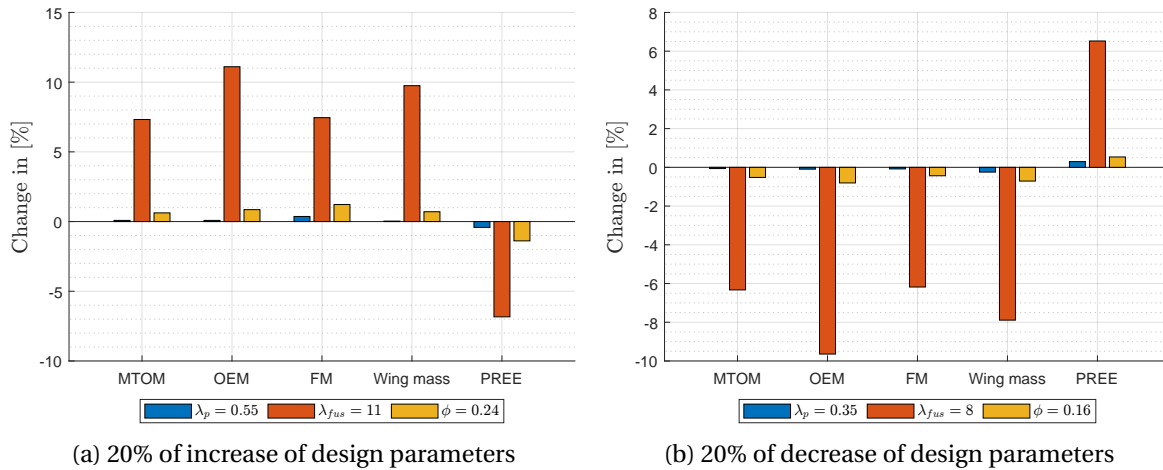


Figure 3.6: The sensitivity of aircraft-level KPIs to the change of design parameters

Instead of focusing on aircraft-level mass KPIs, it is noteworthy to investigate the mass change down to the propulsion system level, as mentioned in Point 2 in the previous analysis. Figure 3.7a and Figure 3.7b present the sensitivity of the entire propulsion system and the electric propulsion system with its related components. Several observations can be drawn:

1. **Change of λ_{fus} :** The impact from λ_{fus} becomes less significant at the system level. From the perspective of the entire propulsion system, λ_{fus} is still the governing factor due to the need to counterbalance the drag during the cruise. The increase in the entire propulsion system mass can be attributed to the heavier primary powertrain, in which all non-electric powertrain components contribute to the mass increment. Its significance diminishes in the electrical propulsion system, which is highly correlated to the setting of ϕ .
2. **Change of ϕ :** The shaft-power ratio exerts significant influence on the mass of electric propulsion components, primarily due to its direct impact on the allocation of shaft power for the BLI propeller. A higher ϕ value signifies that a greater proportion of the aircraft's thrust is generated by the BLI propeller. In contrast to the behavior observed in the change of λ_{fus} , the adjustment of ϕ results in a noticeable increase in the mass of all electric propulsion components. However, this influence on component mass is not immediately evident when considering the aircraft as a whole. Nonetheless, it emphasizes the necessity for a more detailed analysis of the impact of ϕ .
3. **Change of λ_p :** The influence of λ_p is more evident when examining the propulsion system rather than the aircraft as a whole. Notably, reducing the propeller size (a smaller λ_p) has a more pronounced effect than increasing it. A smaller propeller offers greater power-saving benefits because it operates in close proximity to the wall, where boundary layer velocity is very slow, and the propeller can harvest more power. Nevertheless, it is essential to note that, within all aircraft design parameters, the impact of λ_p remains relatively modest.

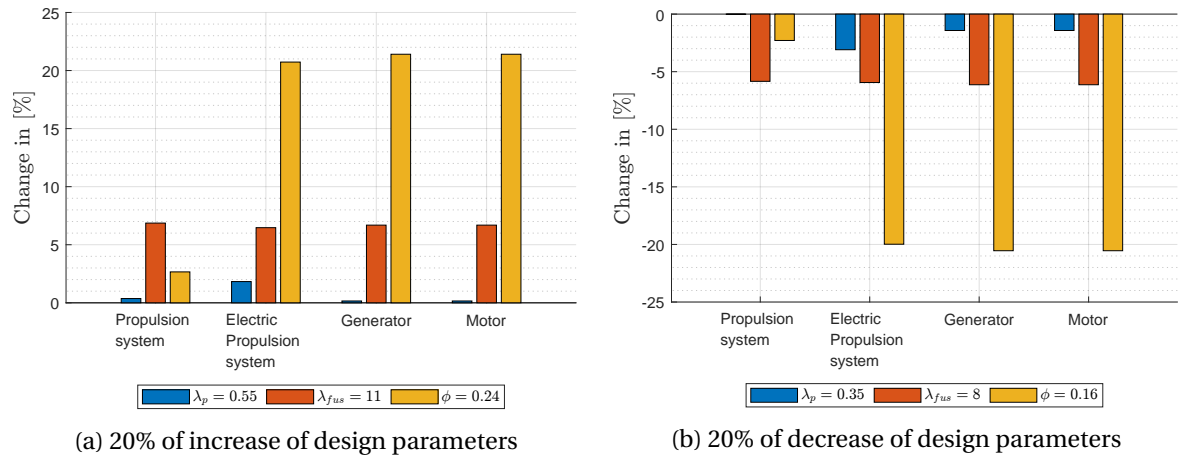


Figure 3.7: The sensitivity of propulsion system weight to the change of design parameters

Lastly, to further investigate the BLI effect due to the change of aircraft design parameters, $\Delta\eta_{p,cruise}$ and $\Delta C_{D0,cruise}$ are plotted with wing area in Figure 3.8a and Figure 3.8b to help the analysis of the result. Numerous observations can be discerned:

1. **Change of λ_{fus} :** It can be seen in Figure 3.8a that a higher value of λ_{fus} is still the most dominant aircraft design parameter, which means longer fuselage results in a slow boundary layer velocity profile and more power. However, a longer fuselage increases the profile drag induced by BLI because of a heavier aircraft and more required thrust. The BLI propeller has to accelerate the boundary layer more to obtain the required thrust, causing a thinner boundary layer and higher friction drag. Furthermore, a faster boundary layer decreases the static pressure around the fuselage tailcone, leading to an increase in the pressure drag. The drag penalty decreases when the fuselage is shorter but with the compromise of a lower power-saving benefit.
2. **Change of ϕ :** The increase in ϕ has opposite effects that more power supplied to the BLI propeller makes the value of $\Delta\eta_{p,cruise}$ decrease but $\Delta C_{D0,cruise}$ increase. Providing more power to the BLI propeller with a constant λ_p deteriorates the BLI effect because the propeller has to generate greater thrust force, making the propeller optimization find the feasible design with a longer blade chord or higher pitch setting. Thus, the blade aerodynamic effect becomes significant and reduces the benefit from BLI. The cause of the drag increment is the same as the mechanism described in the previous point. These penalties will vanish as ϕ decreases.
3. **Change of λ_p :** The increase of λ_p has a similar effect to a higher ϕ setting. As shown in Figure 3.8a, $\Delta\eta_{p,cruise}$ decreases by 22% because of a higher proportion of freestream in the propeller inflow. This issue in the blade aerodynamics with ingesting more high-speed inflow has been discussed in section 3.2. However, from the perspective of the profile drag due to BLI, a larger BLI propeller decreases the profile drag penalty on the fuselage because of its size. The large BLI propeller can achieve the required thrust without accelerating the boundary layer significantly. On the other hand, small λ_p provides outstanding performance of power saving because it is fully immersed in the boundary layer.

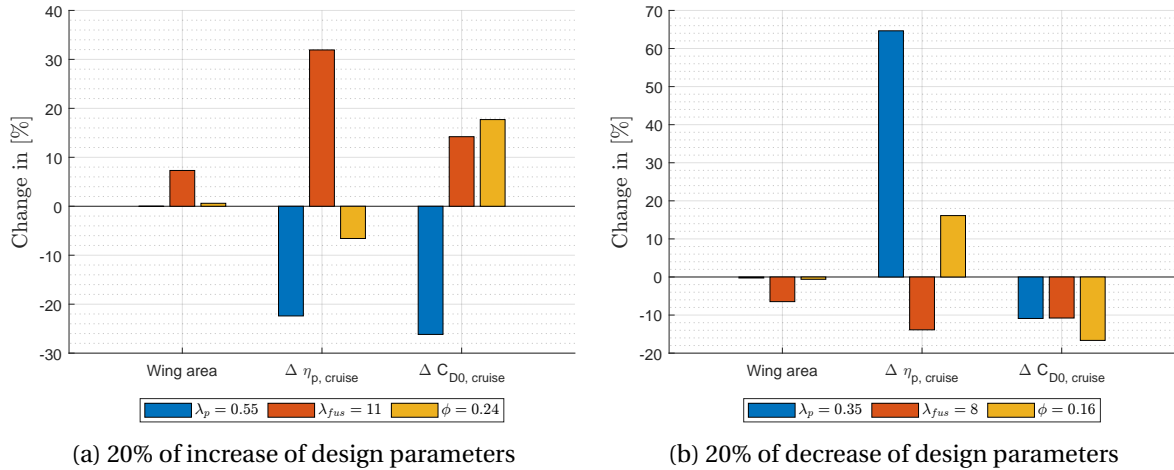
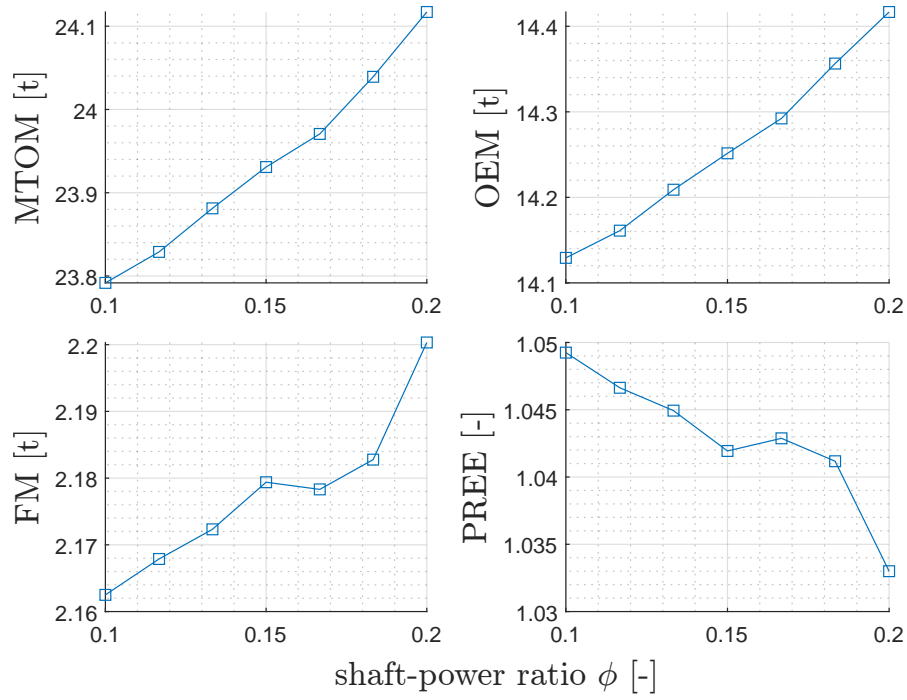


Figure 3.8: The sensitivity of BLI effects to the change of design parameters

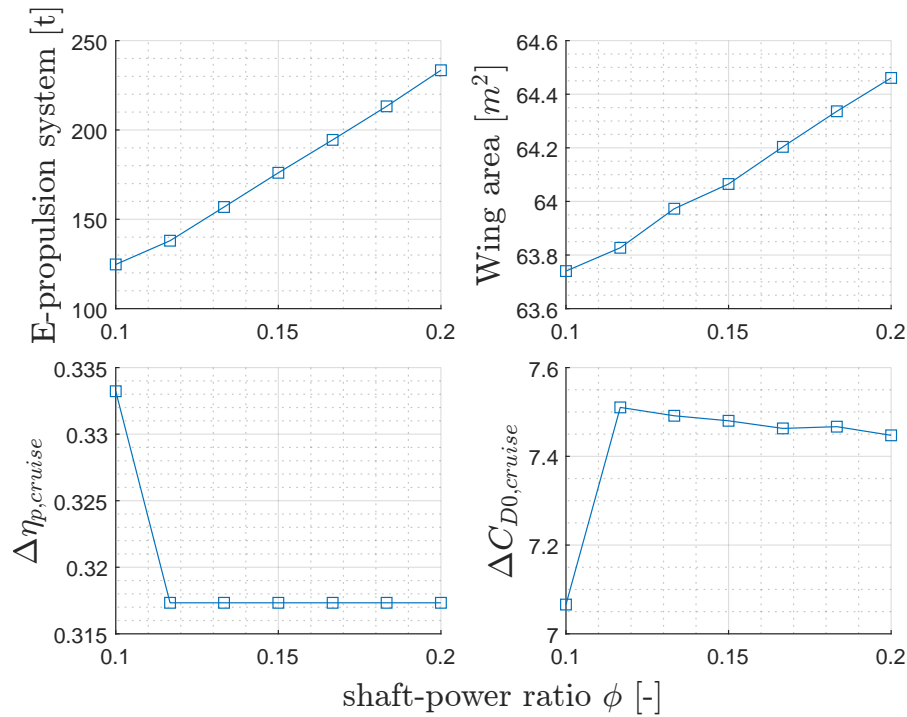
Nevertheless, it should be mentioned that a λ_p of 0.35 shows an unexpected trend of drag for smaller propeller size in Figure 3.8b. Instead of showing an increase in $\Delta C_{D0, \text{cruise}}$, the small propeller results in less BLI-induced profile drag during the cruise. This phenomenon relates to the limit of the surrogate model. The required $T_{c,eq}$ from the aircraft sizing exceeds the upper bound of the surrogate model for λ_p of 0.35. This issue requires more attention on the setting of ϕ and highlights the need to fine-tune the power allocation between the primary and BLI propulsion systems.

3.3.3. INVESTIGATION OF THE POWERTRAIN SETTING

Seven additional radical aircraft designs are generated to investigate further the effect of ϕ combined with other design parameters. Based on the sensitivity analysis, it is decided to fix λ_{fus} the same as the reference ATR-72 aircraft. Although a longer fuselage increases the power-saving effect from a BLI's perspective, the cyclic weight penalty outweighs any benefit gained on the system level. In order to maximize the power-saving benefit due to BLI, λ_p is decided to be 0.35 so the BLI propeller fully operates within the boundary layer. The setting of ϕ breaks into seven levels to understand the combined effect with λ_p and analyze to what extent the power-saving benefit at the system level will reflect at the aircraft level.



(a) The change of aircraft-level KPIs



(b) The change of system-level KPIs

Figure 3.9: The change of KPIs for the aircraft with different setting of ϕ .

Figure 3.9 illustrates the change of KPIs at different levels. The aircraft-level KPIs show a consistent trend with an increase in ϕ . This trend is expected as the cyclic weight penalty induced by the electrical powertrain leads to a higher MTOM, OEM, and the required fuel mass for the mission. Although there seems to be a decrease in the required fuel mass at ϕ of 0.17, the percentage of

change suggests that it may be due to the convergence tolerance. On the other hand, there is a plateau from the second ϕ setting for both $\Delta\eta_{p,cruise}$ and $\Delta C_{D0,cruise}$. It implies that the required $T_{c,eq}$ exceeds the upper bound of the surrogate model. Even if ϕ increases up to 0.2, only the mass of electrical components increases with this PcP. The actual required $T_{c,eq}$ is higher than the available $T_{c,eq}$, leading to an underestimated $\Delta\eta_{p,cruise}$ and $\Delta C_{D0,cruise}$. Even if the profile drag induced by BLI is underestimated, this advantage is still insignificant to impact the final MTOM.

Additionally, the result presented in [Figure 3.9](#) also suggests two conclusions:

1. The bound of $T_{c,eq}$ in the surrogate model is relatively narrow when the disk loading is high. Therefore, a comprehensive study of the setting for ϕ is recommended to avoid the problem of overestimating the power-saving benefit at a higher disk loading. This is important even though the aero-propulsive effect of BLI hardly shows on high-level KPIs.
2. All radical designs do not yield a higher PREE than the reference aircraft. This implies that the PTE powertrain and BLI technology may not provide any aero-propulsive benefit to regional turboprop aircraft, as previously found by Bonnin and Hoogreef [33]. On the contrary, a larger aircraft, such as a medium-range aircraft, shows the benefit of using the BLI propulsor. The thicker boundary layer of a larger aircraft makes the flow field more favorable for the optimized BLI propulsor to operate, which strengthens the power-saving benefit. This hypothesis suggests an opportunity for further investigation.

A further investigation of the limitation of the surrogate model is conducted in the next section with full BLI propeller optimization on the targeted aircraft configuration within the plateau region in [Figure 3.9b](#).

3.3.4. INVESTIGATION OF CONSTRAINTS OF THE SURROGATE MODEL

A further investigation of the surrogate model aims to identify the cause of the limitation and suggests possible solutions to address these challenges. The BLI propeller optimization case is selected from the first radical design case in the plateau region, as shown in the previous section. The radical aircraft design supplies 12% of total shaft power to the BLI propeller. [Table 3.4](#) presents the dimensionless parameters for the optimization. It is noted that this table shows the parameters at the cruise condition.

λ_{fus}	λ_{tc}	λ_p	J	$T_{c,eq}$
9.93	2.5	0.35	2.19	0.48

Table 3.4: Baseline design variables

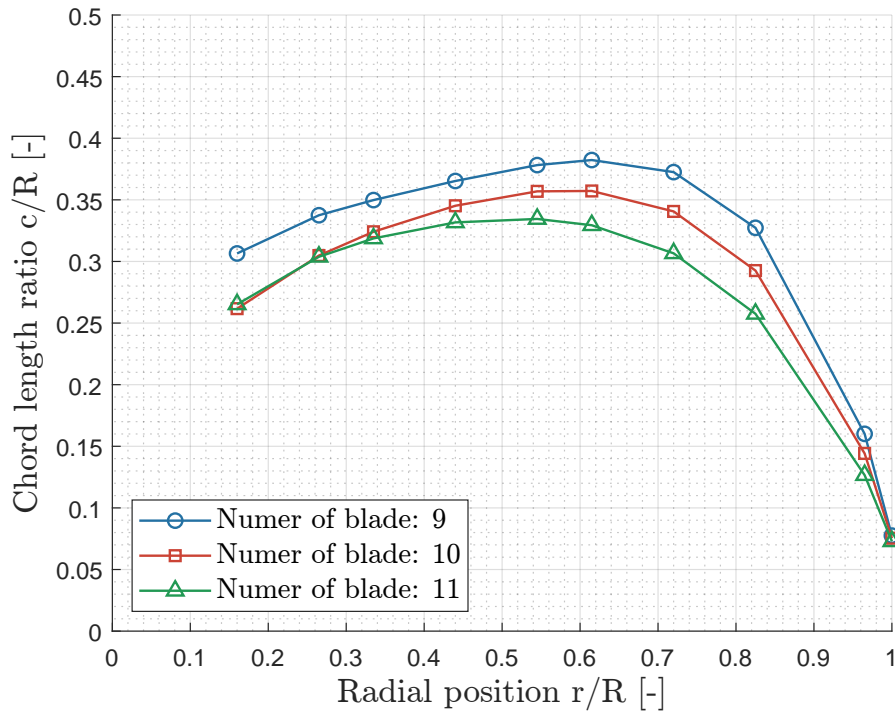
It is found that the optimizer cannot reach convergence and find a feasible design with the proposed optimization setup. Only changing the twist and chord distribution over the blade causes the optimizer trap into the infeasible design region, increasing the blade twist angle and violating constraints. Therefore, it is necessary to include the number of blades as the design variable.

There are three different numbers of blades to perform the BLI propeller optimization. [Figure 3.10](#) shows the distribution of chord and twist along the blade. There are two observations can be made from these comparisons:

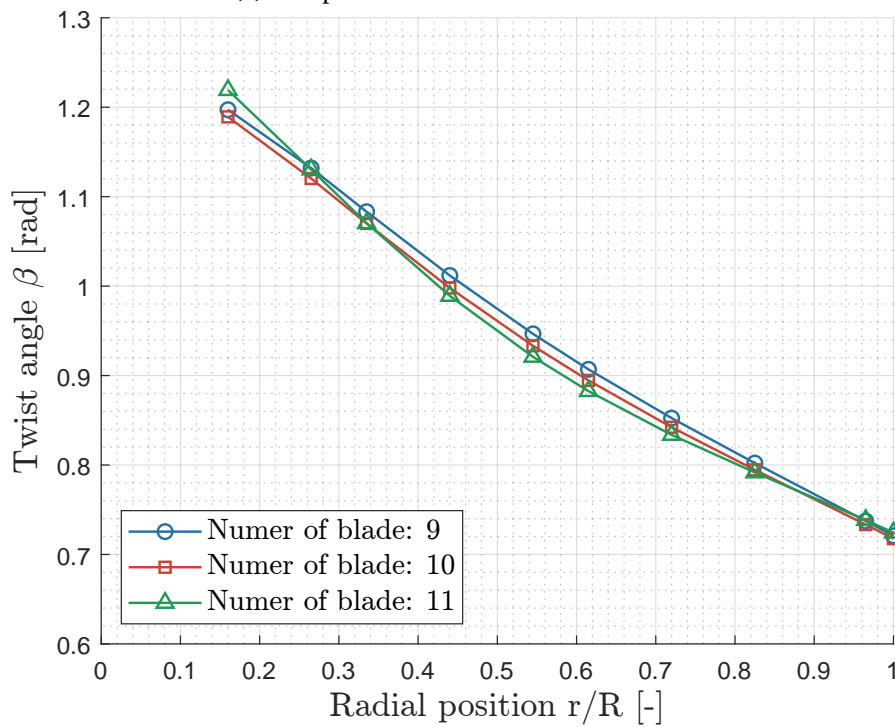
1. **Chord distribution:** The required thrust for the three propeller designs is identical. It is evident that the increase in the number of blades has the opposite trend to the chord length. When the number of blades increases from 9 to 11, the chord length decreases by 17.7%

around the 70% radial position on the blade. Furthermore, unlike the propeller designed for freestream ingestion, the longest chord length position moves toward the inboard due to the boundary layer ingestion. The initial geometry of XPROP has the longest chord length around 70% radius. However, all three BLI propeller designs have a maximum chord length of around 50-60% radius. The velocity gradient in the boundary layer results in a favorable thrust-to-power ratio region toward the propeller root [43]. The optimizer, thus, tends to increase the local circulation in this region to take this advantage.

2. **Twist distribution:** The blade configuration with 11 blades exhibits a smaller twist angle along the entire blade length compared to the other configurations. This results in a reduced local angle of attack. Additionally, it is notable that the twist angle at the blade root is comparatively higher, which aligns with the earlier observation that the optimizer amplifies local circulation to optimize the favorable thrust-to-drag ratio. However, it is essential to emphasize that, overall, the differences in twist distribution among all three BLI propeller designs remain relatively minimal. This result could be due to the optimizer that the change in the twist angle is relatively easy to violate the constraint and lead to the angle of attack out of the linear range. Moreover, these three BLI propeller designs require fine-tuned initial design variables and the initial twist distribution to prevent the optimizer from falling into the infeasible design space. Therefore, the optimizer tends to avoid the constraint area and turns to alter the chord distribution to minimize the value of the objective function.



(a) Comparison of the chord distribution



(b) Comparison of the twist distribution

Figure 3.10: Comparison of chord and twist distributions of three additional BLI propeller design

The BLI propeller blade design with different numbers of blades is presented in Figure 3.11 as the reference to visualize the chord and twist distributions. All propeller designs are present in two perspectives. The red dashed line represents the location of the sectional airfoil, and the red solid line represents the quarter-chord line of the blade.

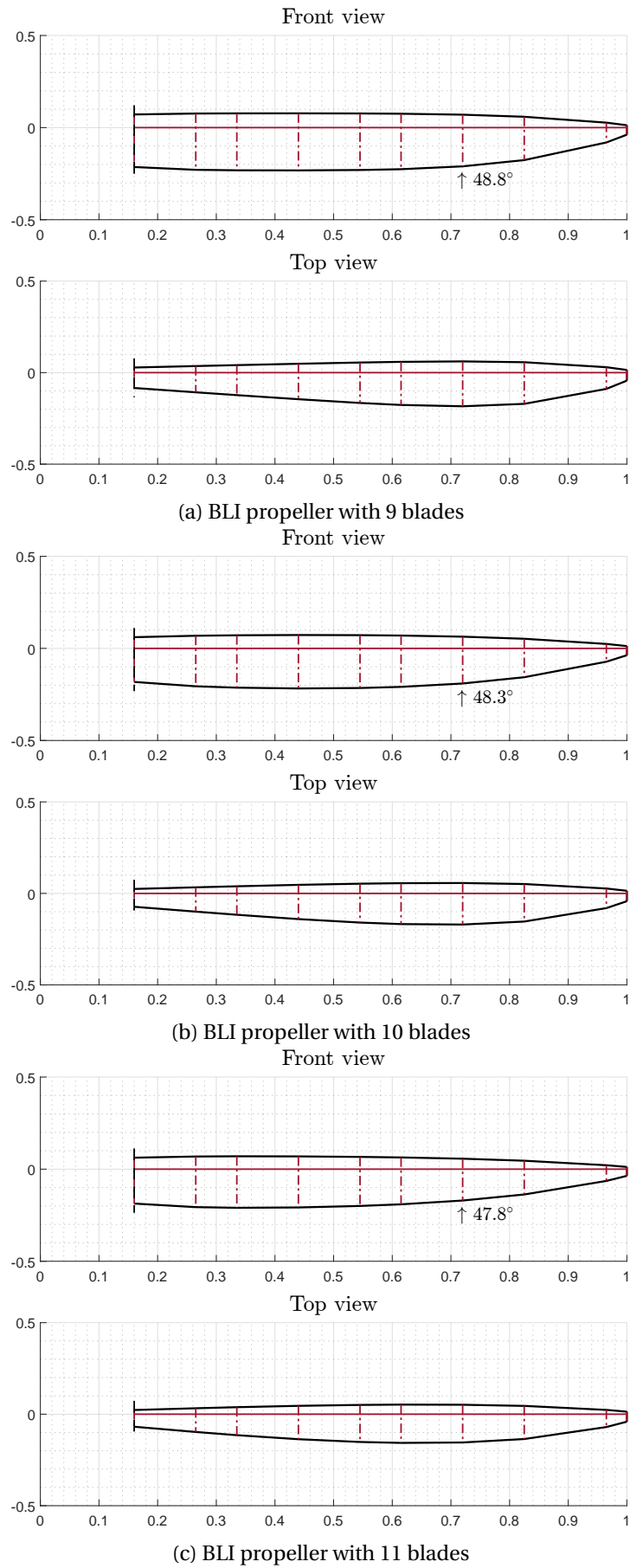


Figure 3.11: All optimized propeller planform for BLI with different blade numbers.

As this section is the extended study on the limitation of the surrogate model, [Table 3.5](#) presents the power-saving benefit of all aforementioned BLI propeller designs. As can be seen in this result, the optimal number of blades for the maximum power-saving benefit during the cruise is 10. This optimal number can be explained by the drag of the blade. The small blade number makes the propeller have to be equipped with a wider blade to generate the required thrust; however, the propeller will require more power to overcome the torque. As the blade number increases, the blade becomes slender. However, more blade numbers again increase the surface area, which leads to the total drag being larger than small blade numbers. Unlike the actuator disk theory, which models the propeller to be an infinitesimally thin blade in the stream tube, the propeller analysis reflects the influence of blade aerodynamics.

Number of blade	$\Delta\eta_{p,cruise}$
9	0.296
10	0.323
11	0.306

Table 3.5: The resulting power-saving benefit of the corresponding blade number

This comprehensive investigation into the limitations of the surrogate model reveals that addressing the issue of the plateau in $\Delta\eta_{p,cruise}$ is achievable through the execution of a full propeller optimization. However, it is important to note that the extent of the power-saving benefit, as presented in [Table 3.5](#), is anticipated to have a minimal impact on the final conceptual aircraft design.

As observed in [subsection 3.3.2](#), the influence of such a small propeller with a greater number of blades can be analyzed at three distinct levels:

1. At the aircraft-level mass, the effect of the change in propeller size is relatively negligible. Although a reduction in power-saving benefit necessitates a larger powertrain mass, inducing a cyclic weight penalty in the final aircraft design, the overall increase in aircraft mass should remain marginal.
2. Down to the propulsion system level, the impact of a diminished power-saving benefit becomes more noticeable than the aircraft-level mass change. To meet the increased power requirements for driving the BLI propeller and generating the necessary thrust, the mass of the electric propulsion system must grow. Consequently, the reduction in mass associated with a smaller BLI propeller will diminish.
3. Finally, the power-saving benefit of the aircraft configuration with λ_p of 0.35, as discussed in [subsection 3.3.2](#), is estimated at 64% higher than the baseline radical design using the surrogate model. However, the fully optimized BLI propeller with 10 blades, as presented in this section, yields only a 40% increase in power-saving benefits. On the other hand, a higher thrust requirement for a small propeller accelerates the boundary layer, resulting in an increase in the drag penalty by 27.5%.

Furthermore, given that the surrogate model is developed with the propeller design and optimization routines, both design processes exhibit a strong interconnection in terms of potential enhancements to the surrogate model. While the limitation concerning disk loading in the surrogate model can be addressed by incorporating the number of blades as a design variable in the optimization, the resulting power-saving benefit can be further refined by considering two key aspects:

1. **Sweep and rake angle:** It is important to note that, in this thesis, the propeller design is constrained to straight blades for two primary reasons. Firstly, the propeller design tool is incapable of modeling blade aerodynamics with non-radial lifting line distributions, primarily due to a lack of comprehensive documentation [45]. However, the incorporation of sweep and rake angles can enable the propeller to operate at higher rotational speeds, potentially leading to reductions in blade chord length or local twist angles. This, in turn, has the potential to decrease the power required to generate a given thrust force.
2. **Airfoil shape:** The optimization of airfoil shape is not concerned within this thesis due to computational constraints. Additionally, XFOIL has demonstrated instability in certain cases, particularly at high Reynolds numbers, leading to infinite loops and impeding the optimization process. However, it is worth noting that tailoring the airfoil shape to accommodate boundary layer inflow has the potential to enhance the thrust-to-drag ratio, influencing both chord and twist distributions along the blade.

The limitations of the surrogate model can be effectively addressed by employing BLI propeller optimization with an increased number of blades. Furthermore, the proposed solutions outlined above primarily target the assumptions inherent in the methodology. However, when combining all these improvements, a higher fidelity tool is necessitated to perform the optimization, thereby demanding additional time and computational resources. In contrast, the surrogate model serves as a rapid estimation approach for evaluating the power-saving benefits resulting from BLI during the conceptual aircraft design phase.

4

CONCLUSION AND RECOMMENDATION

The conclusion of the findings in this thesis is present in [section 4.1](#), and the recommendations for future work are listed in [section 4.2](#)

4.1. CONCLUSION REMARK

The aviation authority has set a goal of reducing emissions by 2050, and the call for sustainable aviation is urgent. The BLI is one of the promising technologies that can reduce energy consumption. Several conceptual studies have been conducted to develop the BLI propulsion system on conventional tube-and-wing aircraft. This system ingests the fuselage boundary layer, re-energizing it to propel the aircraft. However, this mechanism also redefines the propeller efficiency and can exceed the unity. Moreover, using the BLI propulsor increases the fuselage drag and aircraft weight penalties and the required energy is not necessarily reduced depending on the powertrain assumptions.

This thesis explores how aircraft design parameters affect the performance of hybrid-electric aircraft with the BLI propeller, divided into three sub-objectives.

1. **Improvement of the existing BLI model**

The fundamental BLI model within the conceptual aircraft design tool is constructed upon actuator disk theory, which relies on certain assumptions, including uniform inflow, an infinitesimally thin propeller disk, an upstream axisymmetric fuselage body, and the absence of flow distortion caused by wings and empennage. This thesis specifically tackles the uniform inflow and thin propeller disk assumptions by employing boundary element theory. The propeller design process, utilizing a combination of XFOIL and XROTOR, results in a maximum 4% deviation in propeller efficiency compared to the reference validation case. Furthermore, the BLI propeller optimization utilizes this design process to find the power-saving benefit and constructs the surrogate model with the Design of Experiments (DoE) method, complemented by Radial Basis Function (RBF) regression analysis.

Sensitivity studies involving a 10% variation in design parameters from their baseline values and a comparison between the existing BLI model and the surrogate model reveal the significant influence of blade aerodynamics. The surrogate model predicts lower power-saving benefits than the actuator disk-based BLI model. For instance, a 10% increase in propeller size results in a 13% overestimation compared to the original BLI model. The larger propeller size, which ingests more high-speed boundary layer flow at the blade's outboard section, induces greater drag and reduces power-saving benefits. This discrepancy arises because the actuator disk-based BLI model, assuming an average boundary layer velocity, underestimates the

effects of high-speed inflow and blade aerodynamics. Generally, the actuator disk-based BLI model predicts 4-12% more power-saving benefits compared to the surrogate model based on the blade element theory.

2. The sensitivity of the aircraft-level performance to the change of aircraft design parameters

The conceptual aircraft design, which integrates a hybrid-electric powertrain and BLI propeller, is accomplished using the in-house MATLAB software known as Aircraft Design Initiator (Initiator). The Initiator incorporates the BLI surrogate model to size all radical aircraft designs. In this approach, a partial-turboelectric hybrid-electric powertrain is chosen, characterized by a unique shaft-power ratio that controls the power distribution.

For reference, the regional turboprop ATR-72 aircraft serves as the benchmark conventional aircraft design. The baseline radical aircraft design, when compared to the reference ATR-72, exhibits a 5.9% increase in maximum takeoff mass and carries 12.9% more fuel mass. However, the BLI effect does not manifest as a benefit in terms of reducing fuel burn, aligning with findings from existing literature. Furthermore, this thesis has explored the impact of three key aircraft design parameters— λ_{fus} , λ_p , and ϕ —each with variations of $\pm 20\%$. The results of this sensitivity study are summarized in [Table 4.1](#).

Performance indicator	Increase by 20%			Decrease by 20%		
	λ_{fus}	ϕ	λ_p	λ_{fus}	ϕ	λ_p
Maximum takeoff mass	+7%	< 1%	< 1%	-6%	< 1%	< 1%
Fuel mass	+7%	+1%	< 1%	-6%	-1%	< 1%
Electrical propulsion system	+6.5%	+21%	+2%	-6%	-20%	-2%
Change in propeller efficiency due to BLI	+31%	-6%	-22%	-14%	+16%	+64%
Change in profile drag due to BLI	+14%	+18%	-26%	-10%	-16%	N/A

Table 4.1: Summary of the sensitivity study of the aircraft performance

It reveals that the propeller size and powertrain setting have the highest impact in terms of power-saving benefits and BLI-induced profile drag. However, the weight penalty outweighs the aero-propulsive benefits of the BLI propeller. The system-level impact on the aircraft is not reflected in aircraft-level performance indicators. Instead, the cyclic weight penalty induced by components shows a dominant effect and deteriorates performance indicators. The N/A indicates that the required disk loading for the BLI propeller exceeds the bound of the surrogate model, raising the need for further investigation.

3. The investigation of powertrain settings

A more in-depth exploration of the powertrain settings uncovers that the surrogate model has a relatively narrow operational range, particularly when the disk loading is high. Additional seven aircraft configurations are analyzed from ϕ of 0.1 to 0.2, all with λ_p set to 0.35. It is notable that ϕ of 0.12 exceeds the upper bound of the surrogate model. A comprehensive study on the limit of the surrogate model was conducted and found that increasing the number of blades on the propeller can potentially address this issue and identify the optimal number of blades. However, implementing this improvement demands a more refined optimization setting. The fundamental limitation of the surrogate model lies in the physical constraints associated with the propeller blades, which are inherently straight and unable to operate at higher

rotational speeds to generate increased thrust. While increasing the number of blades can reach the required thrust, it comes at the cost of significantly diminishing the power-saving benefits and increasing the fuselage profile drag.

While the system-level study indicates that the surrogate model exhibits the impact of blade aerodynamics and estimates a smaller power-saving benefit compared to the original BLI model, this system-level effect does not extend to the aircraft-level performance. It appears that regional turbo-prop aircraft might not benefit from employing a hybrid-electric powertrain with the BLI propeller. However, it is important to note that this thesis is based on several assumptions, which could be refined in future research.

4.2. RECOMMENDATION FOR FUTURE WORK

During the implementation of this thesis, several assumptions were made, and limitations were identified. This section lists the possible solutions as below:

1. **Boundary layer profile modeling:**
The boundary layer in this thesis is measured from the low-speed wind tunnel experiment and further scaled by the boundary layer thickness and edge velocity. A further investigation of the velocity profile can benefit the modeling fidelity. One possible improvement is setting up DoE and simulating the flowfield with different fuselage dimensions, tailcone dimensions, and Mach numbers. However, this investigation might be challenging to create a surrogate model because there might be no clear trend in the velocity profile under different flow conditions.
2. **Propeller optimization setup:**
The propeller design for boundary layer ingestion does not take into account the number of blades, airfoil shape, and sweep angle during optimization. The limitations regarding the first two parameters are mainly due to computational costs, which necessitate more time for optimizing propeller geometry. The absence of consideration for sweep angle is attributed to constraints within the propeller design tool. It is recommended to investigate the sensitivity of propeller performance with respect to these design parameters by employing a higher-fidelity approach, which could involve coupling CFD analysis and meshing software from the existing literature.
3. **Data point distribution for response surface:**
This thesis utilizes a fractional factorial design to construct the experimental design and determine data points for BLI propeller optimization. However, fractional factorial designs lack randomization, which could provide more valuable information within the design space. Future research could explore more randomized experimental designs to enhance the quality of data collected.
4. **Regression method for building the response surface:**
The radial basis function regression is employed in this thesis to interpolate data points and create a multi-dimensional response surface. Nevertheless, there are some data points that deviate from the surface. To improve the model's accuracy, it is recommended to further investigate data point distribution, explore alternative regression methods, and address outliers to enhance the precision of the model.

A

RADIAL BASIS FUNCTION INTERPOLATION

A.1. BASIC CONCEPT

Consider a set of measurements $\{f_i : i = 1, 2, \dots, n\}$, which is a real-valued function of d variables, taken at the corresponding data sites $\{x_i : i = 1, 2, \dots, n\}$, the interpolant $s(x)$ satisfies the interpolation condition and matches exactly at data sites:

$$s(x_i) = f_i, x \in \mathbb{R}^d \quad (\text{A.1})$$

It is assumed that $s(x)$ can be found through a linear combination of interpolants, and the Equation A.1 can be expressed as:

$$s(\mathbf{x}) = \sum_{i=1}^n \lambda_i \phi(\|x - x_i\|) \quad (\text{A.2})$$

$\|x - x_i\|$ is called Euclidean distance, which is evaluated from the center point x . This distance is calculated by $\sqrt{(x_i - x_j)^2 + (y_i - y_j)^2}$. Sometimes $\|x - x_i\|$ is written as r_{ij} as radial distance. The Euclidean distance makes basis function ϕ become a radially symmetric function. Thus, $s(x)$ is a linear combination of radial basis functions. Moreover, the Equation A.2 can be written further from the Equation A.1 as:

$$\sum_{i=1}^n \lambda_i \phi(\|x_j - x_i\|) = \sum_{i=1}^n \lambda_i \phi(r_{ij}) = f_j, j = 1, 2, \dots, n \quad (\text{A.3})$$

and in a matrix form:

$$\Phi \lambda = \mathbf{f} \quad (\text{A.4})$$

The symmetric matrix Φ has to be non-singular, so the system is unisolvent.

A.2. ADDITIONAL POLYNOMIAL PRECISION

In order to increase the fitting precision of the radial basis function, it is useful to add an additional low-degree polynomial. Let's define Π_m^d to represent the linear space of polynomial functions defined in d -dimensional Euclidean space (\mathbb{R}^d) where the highest degree of any term in the polynomials is at most m . The Equation A.2 can be rewritten with additional polynomial term $p_j(x)$ as:

$$s(\mathbf{x}) = \sum_{i=1}^n \lambda_i \phi(\|x - x_i\|) + \sum_{j=1}^{\hat{m}} \gamma_j p_j(x) \quad (\text{A.5})$$

With additional constrains:

$$\sum_{i=1}^n \lambda_i p_j(x_i) = 0 \quad (\text{A.6})$$

Eventually, the system of linear combination of radial basis function can be presented as:

$$\begin{bmatrix} \Phi & P \\ P^T & \mathbf{0} \end{bmatrix} \begin{bmatrix} \boldsymbol{\lambda} \\ \boldsymbol{\gamma} \end{bmatrix} = \begin{bmatrix} \mathbf{f} \\ \mathbf{0} \end{bmatrix} \quad (\text{A.7})$$

However, the regression quality over the data sites is not ideal only with simple Euclidean distance. The interpolation function is discontinued at the data site x . Thus, the additional smooth functions are required to create a continuous function at x . These smooth interpolation functions are called kernels, which will be discussed in the next section.

A.3. TYPE OF RBF KERNEL

There are several classical kernels in the context of radial basis function. The [Table A.1](#) presents kernels as the corresponding mathematical form. Except for the polyharmonic splines, in this case, also known as thin-plate splines, the kernel has a shape parameter, γ , to control the shape of the function and its response to the variation in the data. A larger shape parameter will make the kernel function less flexible and not responsive to the small-scale variations in the data, while a small shape parameter allows the kernel function to match the data but potentially results in oscillatory interpolation. Thus, it is important to tune the shape parameter for those kernel functions.

Kernel name	Kernel function	Minimum polynomial degree	Parameters
Gaussian	$\gamma^{-(cr)^2}$	0	$c > 0$
Polyharmonic splines	$r^{2m} \log(r)$	1	$c > 0$
Multiquadrics	$\sqrt{r^2 + c^2}$	0	$c > 0$
Inverse Multiquadrics	$\frac{1}{\sqrt{r^2 + c^2}}$	0	$c > 0$

Table A.1: Classical kernel of radial basis function. Recompiled from [56, 59, 60]

In this thesis, it is decided to use polyharmonic splines because it can predict the data in the data-free region well. Yet, to avoid the singularity problem in the Φ matrix with polyharmonic splines, an infinitesimal value, 10^{-6} , is implemented to r as $r + \xi$.

A two-dimensional example is presented to show the use of the radial basis function. With a set of dependent and independent variables, the coefficients and polynomial extension can be solved by using [Equation A.7](#):

$$\Phi \boldsymbol{\lambda} + P \boldsymbol{\gamma} = \mathbf{f} \quad (\text{A.8})$$

$$P^T \boldsymbol{\lambda} = \mathbf{0} \quad (\text{A.9})$$

Where the matrix Φ and P can expressed as:

$$\Phi = \begin{bmatrix} \|x_1 - x_1\| & \|x_1 - x_2\| & \|x_1 - x_3\| & \dots & \|x_1 - x_n\| \\ \|x_2 - x_1\| & \|x_2 - x_2\| & \|x_2 - x_3\| & \dots & \|x_2 - x_n\| \\ \|x_3 - x_1\| & \|x_3 - x_2\| & \|x_3 - x_3\| & \dots & \|x_3 - x_n\| \\ \vdots & \vdots & \vdots & \ddots & \vdots \\ \|x_n - x_1\| & \|x_n - x_2\| & \|x_n - x_3\| & \dots & \|x_n - x_n\| \end{bmatrix} \quad (\text{A.10})$$

$$P = \begin{bmatrix} 1 & x_1 & y_1 \\ 1 & x_2 & y_2 \\ 1 & x_3 & y_3 \\ \vdots & \vdots & \vdots \\ n & x_n & y_n \end{bmatrix} \quad (\text{A.11})$$

Moreover, the vector λ and γ can be written as:

$$\lambda = [\lambda_1 \quad \lambda_2 \quad \lambda_3 \quad \dots \quad \lambda_n]^T \quad (\text{A.12})$$

$$\gamma = [c_0 \quad c_1 \quad c_2]^T \quad (\text{A.13})$$

Therefore, the low-degree polynomial term is expressed as $c_0 + c_1x + c_2y$. In this example, the low-degree polynomial is linear.

A.4. SENSITIVITY STUDY OF PARAMETERS FOR RBF KERNEL

The study explores the RBF kernel of thin plate spline by conducting a sensitivity analysis, altering the smoothing parameter (c) and degree of polynomial (N). The results of this analysis are depicted in figures from [Figure A.1](#) to [Figure A.5](#).

Five Key Performance Indicators (KPIs) are employed to assess the quality of RBF interpolation. The coefficient of determination serves as a fundamental measure for all interpolation methods. The mean and maximum deviations are presented to illustrate the discrepancy between predicted and actual values.

It is important to note that these three KPIs are derived from an average of 10 iterations of the RBF interpolation due to the random nature of selecting training and testing points.

An additional 23 points are used to assess the accuracy of predictions in regions devoid of data. The average error of matched points is also provided for reference.

Upon evaluating all KPIs and striking a balance between interpolation quality and error margin, it is found that a second-degree polynomial with $c = 0.01$ offers the most balanced performance.

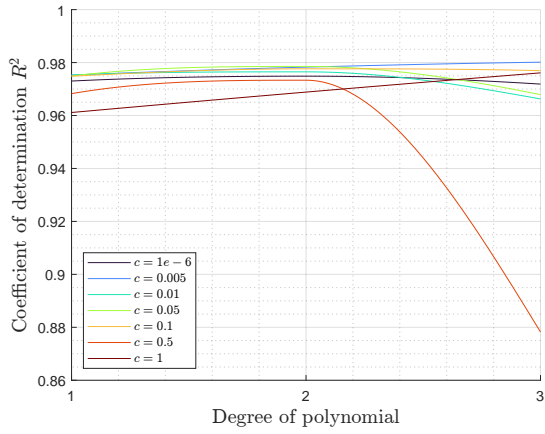


Figure A.1: R^2 value against N with different c

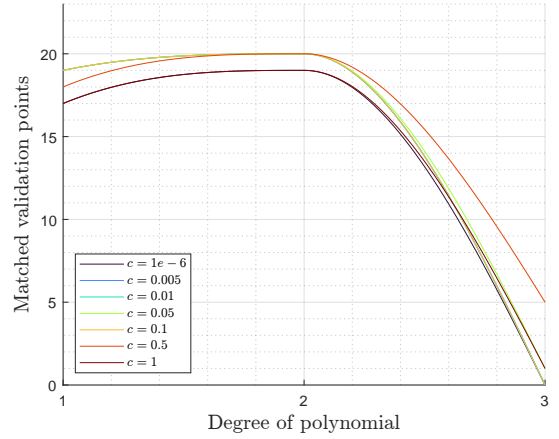


Figure A.2: Number of matched validation point against N with different c

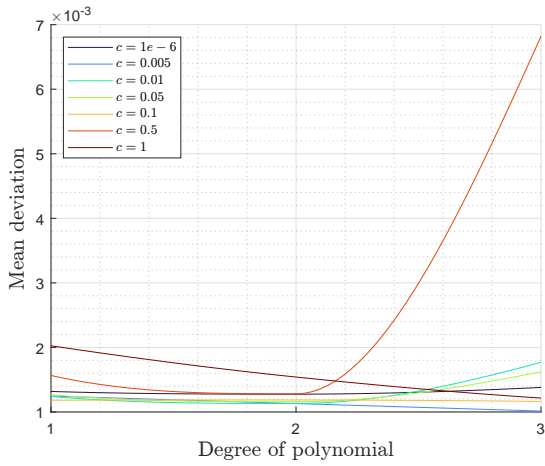


Figure A.3: Mean deviation against N with different c

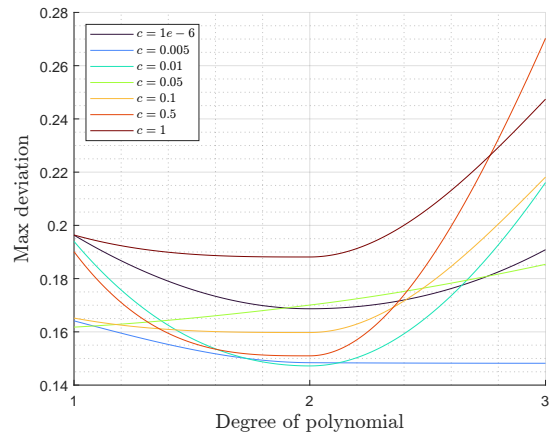


Figure A.4: Max deviation against N with different c

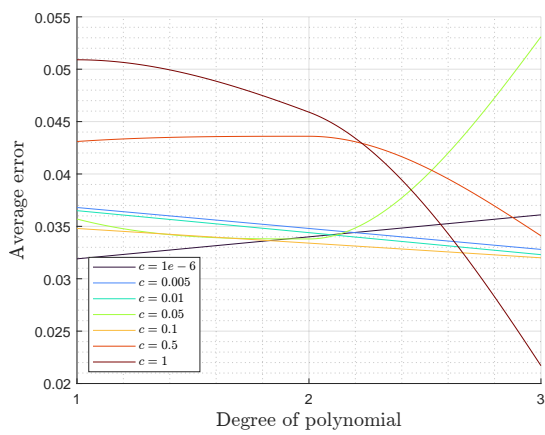


Figure A.5: Average error against N with different c

BIBLIOGRAPHY

- [1] European Commission. *COMMUNICATION FROM THE COMMISSION TO THE EUROPEAN PARLIAMENT, THE EUROPEAN COUNCIL, THE COUNCIL, THE EUROPEAN ECONOMIC AND SOCIAL COMMITTEE AND THE COMMITTEE OF THE REGIONS The European Green Deal*. en. Tech. rep. 52019DC0640. Publisher: European Commission. Brussels, Belgium, Nov. 2019, p. 24. URL: <https://eur-lex.europa.eu/legal-content/EN/ALL/?uri=COM:2019:640:FIN>.
- [2] European Commission, Directorate-General for Mobility and Transport, and Directorate-General for Research and Innovation. *Flightpath 2050: Europe's vision for aviation: maintaining global leadership and serving society's needs*. Publications Office, 2012. DOI: [10.2777/15458](https://doi.org/10.2777/15458).
- [3] Leroy H. Smith. "Wake ingestion propulsion benefit". In: *Journal of Propulsion and Power* 9.1 (Jan. 1993). Publisher: American Institute of Aeronautics and Astronautics, pp. 74–82. ISSN: 0748-4658. DOI: [10.2514/3.11487](https://doi.org/10.2514/3.11487). URL: <https://doi.org/10.2514/3.11487> (visited on 03/27/2023).
- [4] Jai Ahuja and Dimitri N. Mavris. "Sensitivity of Boundary Layer Ingestion Effects to Tube and Wing Airframe Design Features". In: *AIAA Scitech 2020 Forum*. AIAA SciTech Forum. American Institute of Aeronautics and Astronautics, Jan. 2020. DOI: [10.2514/6.2020-1523](https://doi.org/10.2514/6.2020-1523). URL: <https://doi.org/10.2514/6.2020-1523> (visited on 03/30/2023).
- [5] Gérald Carrier et al. "Numerical and Experimental Aerodynamic Investigations of Boundary Layer Ingestion for Improving Propulsion Efficiency of Future Air Transport". en. In: *31st AIAA Applied Aerodynamics Conference*. San Diego, CA: American Institute of Aeronautics and Astronautics, June 2013. DOI: [10.2514/6.2013-2406](https://doi.org/10.2514/6.2013-2406). URL: <https://arc.aiaa.org/doi/10.2514/6.2013-2406> (visited on 11/26/2022).
- [6] Biagio Della Corte et al. "Power Balance Analysis Experiments on an Axisymmetric Fuselage with an Integrated Boundary-Layer-Ingesting Fan". In: *AIAA Journal* 59.12 (Dec. 2021). Publisher: American Institute of Aeronautics and Astronautics, pp. 5211–5224. ISSN: 0001-1452. DOI: [10.2514/1.J060570](https://doi.org/10.2514/1.J060570). URL: <https://doi.org/10.2514/1.J060570> (visited on 03/30/2023).
- [7] Jason Welstead and James L. Felder. "Conceptual Design of a Single-Aisle Turboelectric Commercial Transport with Fuselage Boundary Layer Ingestion". en. In: *54th AIAA Aerospace Sciences Meeting*. San Diego, California, USA: American Institute of Aeronautics and Astronautics, Jan. 2016. ISBN: 978-1-62410-393-3. DOI: [10.2514/6.2016-1027](https://doi.org/10.2514/6.2016-1027). URL: <https://arc.aiaa.org/doi/10.2514/6.2016-1027> (visited on 11/09/2022).
- [8] James L Felder et al. "Updated Assessment of Turboelectric Boundary Layer Ingestion Propulsion Applied to Single-Aisle Commercial Transport". en. In: (Oct. 2022). URL: <https://ntrs.nasa.gov/citations/20210016661>.
- [9] Arne Seitz et al. "Proof of Concept Study for Fuselage Boundary Layer Ingesting Propulsion". In: *Aerospace* 8.1 (2021). ISSN: 2226-4310. DOI: [10.3390/aerospace8010016](https://doi.org/10.3390/aerospace8010016).
- [10] Hermann Schlichting and Klaus Gersten. *Boundary-Layer Theory*. en. Berlin, Heidelberg: Springer Berlin Heidelberg, 2017. ISBN: 978-3-662-52919-5. DOI: [10.1007/978-3-662-52919-5](https://doi.org/10.1007/978-3-662-52919-5). URL: <http://link.springer.com/10.1007/978-3-662-52919-5> (visited on 11/13/2022).

- [11] Hans-Jörg Steiner et al. “Multi-disciplinary Design and Feasibility Study of Distributed Propulsion Systems”. en. In: *28th Congress of the International Council of the Aeronautical Sciences*. Vol. 1. Brisbane, Australia: International Council of The Aeronautical Sciences, Sept. 2012, pp. 403–415. ISBN: 978-1-62276-754-0. URL: http://www.icas.org/ICAS_ARCHIVE/ICAS2012/PAPERS/803.PDF.
- [12] Virendrakumar Chaturbhai Patel. *On the Equations of a Thick Axisymmetric Turbulent Boundary Layer*. IIHR report. Institute of Hydraulic Research, University of Iowa, 1974. URL: <https://books.google.nl/books?id=2TCSkfN2sasC>.
- [13] Alejandra Uranga et al. “Boundary Layer Ingestion Benefit of the D8 Transport Aircraft”. en. In: *AIAA Journal* 55.11 (Nov. 2017), pp. 3693–3708. ISSN: 0001-1452, 1533-385X. DOI: [10.2514/1.J055755](https://doi.org/10.2514/1.J055755). URL: <https://arc.aiaa.org/doi/10.2514/1.J055755> (visited on 11/09/2022).
- [14] Peijian Lv et al. “Performance Analysis of Wake and Boundary-Layer Ingestion for Aircraft Design”. en. In: *Journal of Aircraft* 53.5 (Sept. 2016). Publisher: American Institute of Aeronautics and Astronautics, pp. 1517–1526. ISSN: 0021-8669. DOI: [10.2514/1.C033395](https://doi.org/10.2514/1.C033395). URL: <https://doi.org/10.2514/1.C033395> (visited on 03/27/2023).
- [15] Mark Drela. “Power Balance in Aerodynamic Flows”. en. In: *AIAA Journal* 47.7 (July 2009). Publisher: American Institute of Aeronautics and Astronautics, pp. 1761–1771. ISSN: 0001-1452. DOI: [10.2514/1.42409](https://doi.org/10.2514/1.42409). URL: <https://doi.org/10.2514/1.42409> (visited on 03/27/2023).
- [16] H Clyde McLemore. *Wind-tunnel tests of a 1/20-scale airship model with stern propellers*. en. National Aeronautics and Space Administration, 1962. URL: https://books.google.nl/books?id=Q_4qt2p9pqgC&ots=guFwambwW5&lr&hl=zh-TW&pg=PA1#v=onepage&q&f=false.
- [17] A Plas et al. “Performance of a Boundary Layer Ingesting (BLI) Propulsion System”. en. In: *45th AIAA Aerospace Sciences Meeting and Exhibit*. Reno, Nevada: American Institute of Aeronautics and Astronautics, Jan. 2007. ISBN: 978-1-62410-012-3. DOI: [10.2514/6.2007-450](https://doi.org/10.2514/6.2007-450). URL: <https://arc.aiaa.org/doi/10.2514/6.2007-450> (visited on 11/23/2022).
- [18] Reynard de Vries. *Low-speed fuselage boundary-layer ingestion in conceptual aircraft design*. en. Internal. Delft, Netherlands: Delft University of Technology, Nov. 2019, p. 20.
- [19] Brennan T. Blumenthal et al. “Computational Investigation of a Boundary-Layer-Ingestion Propulsion System”. In: *Journal of Aircraft* 55.3 (May 2018). Publisher: American Institute of Aeronautics and Astronautics, pp. 1141–1153. ISSN: 0021-8669. DOI: [10.2514/1.C034454](https://doi.org/10.2514/1.C034454). URL: <https://doi.org/10.2514/1.C034454> (visited on 03/26/2023).
- [20] David K. Hall et al. “Boundary Layer Ingestion Propulsion Benefit for Transport Aircraft”. en. In: *Journal of Propulsion and Power* 33.5 (Sept. 2017), pp. 1118–1129. ISSN: 0748-4658, 1533-3876. DOI: [10.2514/1.B36321](https://doi.org/10.2514/1.B36321). URL: <https://arc.aiaa.org/doi/10.2514/1.B36321> (visited on 12/13/2022).
- [21] Anaïs Luisa Habermann, Anubhav Gokhale, and Mirko Hornung. “Numerical investigation of the effects of fuselage upsweep in a propulsive fuselage concept”. In: *CEAS Aeronautical Journal* 12.1 (Jan. 2021), pp. 173–189. ISSN: 1869-5590. DOI: [10.1007/s13272-020-00487-2](https://doi.org/10.1007/s13272-020-00487-2). URL: <https://doi.org/10.1007/s13272-020-00487-2>.
- [22] Pradeep Baskaran et al. “Aeropropulsive Performance Analysis of Axisymmetric Fuselage Bodies for Boundary-Layer Ingestion Applications”. In: *AIAA Journal* 60.3 (Mar. 2022). Publisher: American Institute of Aeronautics and Astronautics, pp. 1592–1611. ISSN: 0001-1452. DOI: [10.2514/1.J060362](https://doi.org/10.2514/1.J060362). URL: <https://doi.org/10.2514/1.J060362> (visited on 03/28/2023).

- [23] James Felder et al. "An Examination of the Effect of Boundary Layer Ingestion on Turboelectric Distributed Propulsion Systems". In: *49th AIAA Aerospace Sciences Meeting including the New Horizons Forum and Aerospace Exposition*. Aerospace Sciences Meetings. American Institute of Aeronautics and Astronautics, Jan. 2011. DOI: [10.2514/6.2011-300](https://doi.org/10.2514/6.2011-300). URL: <https://doi.org/10.2514/6.2011-300> (visited on 04/29/2023).
- [24] Marty K Bradley and Christopher K Droney. "Subsonic Ultra Green Aircraft Research". en. In: (May 2012), p. 148. URL: <https://ntrs.nasa.gov/citations/20120009038>.
- [25] Leonardo M. Machado et al. "High-Fidelity Aerodynamic Analysis and Optimization of the SUSAN Electrofan Concept". In: *AIAA SCITECH 2022 Forum*. AIAA SciTech Forum. American Institute of Aeronautics and Astronautics, Dec. 2021. DOI: [10.2514/6.2022-2304](https://doi.org/10.2514/6.2022-2304). URL: <https://doi.org/10.2514/6.2022-2304> (visited on 04/29/2023).
- [26] Ludovic Wiert et al. "Development of NOVA Aircraft Configurations for Large Engine Integration Studies". In: *33rd AIAA Applied Aerodynamics Conference*. AIAA AVIATION Forum. American Institute of Aeronautics and Astronautics, June 2015. DOI: [10.2514/6.2015-2254](https://doi.org/10.2514/6.2015-2254). URL: <https://doi.org/10.2514/6.2015-2254> (visited on 04/29/2023).
- [27] Arne Seitz et al. "CONCEPT VALIDATION STUDY FOR FUSELAGE WAKE- FILLING PROPULSION INTEGRATION". en. In: *31st Congress of the International Council of the Aeronautical Sciences* (2018), pp. 09–14. URL: https://www.icas.org/ICAS_ARCHIVE/ICAS2018/data/papers/ICAS2018_0342_paper.pdf.
- [28] Julian Bijewitz et al. "A review of recent aircraft concepts employing synergistic propulsion-airframe integration". In: *30th Congress of the International Council of the Aeronautical Sciences (ICAS 2016)*. International Council of The Aeronautical Sciences, 2016. ISBN: 978-3-932182-85-3.
- [29] Reynard de Vries, Maurice Hoogreef, and Roelof Vos. "Preliminary Sizing of a Hybrid-Electric Passenger Aircraft Featuring Over-the-Wing Distributed-Propulsion". In: *AIAA Scitech 2019 Forum*. AIAA SciTech Forum. American Institute of Aeronautics and Astronautics, Jan. 2019. ISBN: 978-1-62410-578-4. DOI: [10.2514/6.2019-1811](https://doi.org/10.2514/6.2019-1811). (Visited on 10/13/2023).
- [30] *Single-Aisle Turboelectric Aircraft with Aft Boundary Layer Propulsion (STARC-ABL)*. en-US. June 2023. URL: <https://www1.grc.nasa.gov/aeronautics/eap/airplane-concepts/starc-abl/> (visited on 11/02/2023).
- [31] *ConcEpt validatioN sTudy foR fusElage wake-fillIng propulsioN intEgration | CENTRELINE Project*. en. Aug. 2022. URL: <https://cordis.europa.eu/project/id/723242> (visited on 11/02/2023).
- [32] Maurice Hoogreef et al. "Synthesis of Aero-Propulsive Interaction Studies Applied to Conceptual Hybrid-Electric Aircraft Design". en. In: *AIAA Scitech 2020 Forum*. AIAA SciTech Forum. American Institute of Aeronautics and Astronautics, Jan. 2020. DOI: [10.2514/6.2020-0503](https://doi.org/10.2514/6.2020-0503). URL: <https://doi.org/10.2514/6.2020-0503> (visited on 03/27/2023).
- [33] Vincent O Bonnin and Maurice FM Hoogreef. "Scalability analysis of radical technologies to various aircraft class-part ii: Sensitivity analysis". en. In: *33rd Congress of the International Council of the Aeronautical Sciences (ICAS 2022)*. Vol. 2. Stockholm, Sweden: International Council of The Aeronautical Sciences, Nov. 2022. ISBN: 978-1-71387-116-3. URL: <http://resolver.tudelft.nl/uuid:ef28de38-028a-4e66-b418-c3f8dc659020>.
- [34] Reynard de Vries, Maurice Hoogreef, and Roelof Vos. "Aero-Propulsive Efficiency Requirements for Turboelectric Transport Aircraft". en. In: *AIAA Scitech 2020 Forum*. Orlando, FL: American Institute of Aeronautics and Astronautics, Jan. 2020. ISBN: 978-1-62410-595-1. DOI: [10.2514/6.2020-0502](https://doi.org/10.2514/6.2020-0502). URL: <https://arc.aiaa.org/doi/10.2514/6.2020-0502> (visited on 12/12/2022).

- [35] Biagio Della Corte. *Experimental Investigation of Fuselage-Boundary-Layer Ingestion*. en. Internal. Delft, Netherlands: Delft University of Technology, Dec. 2017.
- [36] Gaetan K. Kenway and Cetin C. Kiris. "Aerodynamic Shape Optimization of the STARC-ABL Concept for Minimal Inlet Distortion". In: *2018 AIAA/ASCE/AHS/ASC Structures, Structural Dynamics, and Materials Conference*. AIAA SciTech Forum. American Institute of Aeronautics and Astronautics, Jan. 2018. DOI: [10.2514/6.2018-1912](https://doi.org/10.2514/6.2018-1912). URL: <https://doi.org/10.2514/6.2018-1912> (visited on 03/28/2023).
- [37] RJM Elmendorp, Roelof Vos, and Gianfranco La Rocca. "A conceptual design and analysis method for conventional and unconventional airplanes". en. In: *29th Congress of the International Council of the Aeronautical Sciences (ICAS 2014)*. Vol. 1. St. Petersburg, Russia: International Council of Aeronautical Sciences, Sept. 2014, pp. 393–405. ISBN: 978-1-63439-411-6.
- [38] P. Jackson. *Jane's All the World's Aircraft 2007/2008*. IHS Jane's All the World's Aircraft. Jane's Information Group, 2007. ISBN: 978-0-7106-2792-6. URL: <https://books.google.nl/books?id=pVgbAAAACAAJ>.
- [39] ATR. *ATR 72-600 Factsheets*. URL: https://www.atr-aircraft.com/wp-content/uploads/2020/07/Factsheets_-_ATR_72-600.pdf.
- [40] Tom Schouten, Maurice Hoogreef, and Roelof Vos. "Effect of Propeller Installation on Performance Indicators of Regional Turboprop Aircraft". In: *AIAA Scitech 2019 Forum*. AIAA SciTech Forum. San Diego, United States: American Institute of Aeronautics and Astronautics, Jan. 2019. ISBN: 978-1-62410-578-4. DOI: [10.2514/6.2019-1306](https://doi.org/10.2514/6.2019-1306). (Visited on 09/07/2023).
- [41] Aerodynamics ESDU. "The influence of body geometry and flow conditions on axisymmetric velocity distribution at subcritical Mach numbers". en. In: *ESDU International, London, UK, Data Item*. Vol. 79020. ESDU, Sept. 1984. ISBN: 978-0-85679-241-0.
- [42] Aerodynamics ESDU. "The influence of body geometry and flow conditions on axisymmetric velocity distribution at subcritical Mach numbers". en. In: *ESDU International, London, UK, Data Item*. Vol. 78037. ESDU, Sept. 1984. ISBN: 978-0-85679-241-0.
- [43] Nando van Arnhem. "Design and Analysis of an Installed Pusher Propeller with Boundary Layer Inflow". en. MA thesis. Delft University of Technology, Sept. 2015. URL: <http://resolver.tudelft.nl/uuid:267beaa5-8b62-4e58-b1ad-ff94355c68f9>.
- [44] H Snel, R Houwink, and J Bosschers. *Sectional prediction of lift coefficients on rotating wind turbine blades in stall*. en. Technical Report ECN-C-93-052. Netherlands: Netherlands Energy Research Foundation (ECN), Petten (Netherlands), Dec. 1994, p. 72.
- [45] Mark Drela and Harold Youngren. *XROTOR*. Feb. 2022. URL: https://web.mit.edu/drela/Public/web/xrotor/xrotor_doc.txt (visited on 04/05/2023).
- [46] John D. Anderson. *Fundamentals of aerodynamics*. eng. Sixth edition. McGraw-Hill series in aeronautical and aerospace engineering. Section: xix, 1130 pages ; 24 cm. New York, NY: McGraw Hill Education New York, NY, 2017. ISBN: 978-1-259-12991-9 978-1-259-25134-4 1-259-12991-8 1-259-25134-9 978-1-259-25134-4 1-259-25134-9.
- [47] Qingxi Li et al. "Design and Experimental Validation of Swirl-Recovery Vanes for Propeller Propulsion Systems". In: *AIAA Journal* 56.12 (Dec. 2018). Publisher: American Institute of Aeronautics and Astronautics, pp. 4719–4729. ISSN: 0001-1452. DOI: [10.2514/1.J057113](https://doi.org/10.2514/1.J057113). URL: <https://doi.org/10.2514/1.J057113> (visited on 07/10/2023).

- [48] Tom Stokkermans, Nando van Arnhem, and Leo Veldhuis. "Mitigation of propeller kinetic energy losses with boundary layer ingestion and swirl recovery vanes". In: *2016 Applied Aerodynamics Conference - Evolution & Innovation Continues - The Next 150 Years of Concepts, Design and Operations*. Bristol, United Kingdom: Royal Aeronautical Society, July 2016. ISBN: 978-1-85768-371-4.
- [49] Brenda Kulfan. "A Universal Parametric Geometry Representation Method - "CST"". In: *45th AIAA Aerospace Sciences Meeting and Exhibit*. Aerospace Sciences Meetings. American Institute of Aeronautics and Astronautics, Jan. 2007. DOI: [10.2514/6.2007-62](https://doi.org/10.2514/6.2007-62). URL: <https://doi.org/10.2514/6.2007-62> (visited on 07/09/2023).
- [50] Fabíola Paula Costa et al. "Aerodynamic Analysis of Conventional and Boundary Layer Ingesting Propellers". In: *Journal of Engineering for Gas Turbines and Power* 145.1 (Dec. 2022). ISSN: 0742-4795. DOI: [10.1115/1.4055014](https://doi.org/10.1115/1.4055014). URL: <https://doi.org/10.1115/1.4055014> (visited on 04/15/2023).
- [51] Mandar N. Thombre, Heinz A. Preisig, and Misganaw B. Addis. "Developing Surrogate Models via Computer Based Experiments". In: *Computer Aided Chemical Engineering*. Ed. by Krist V. Gernaey, Jakob K. Huusom, and Rafiqul Gani. Vol. 37. Elsevier, Jan. 2015, pp. 641–646. ISBN: 1570-7946. DOI: [10.1016/B978-0-444-63578-5.50102-X](https://www.sciencedirect.com/science/article/pii/B978044463578550102X). URL: <https://www.sciencedirect.com/science/article/pii/B978044463578550102X>.
- [52] Saman Razavi, Bryan A. Tolson, and Donald H. Burn. "Review of surrogate modeling in water resources". In: *Water Resources Research* 48.7 (July 2012). Publisher: John Wiley & Sons, Ltd. ISSN: 0043-1397. DOI: [10.1029/2011WR011527](https://doi.org/10.1029/2011WR011527). URL: <https://doi.org/10.1029/2011WR011527> (visited on 11/04/2023).
- [53] Jan Roskam. *Airplane Design: Part 2 - preliminary configuration design and integration of the propulsion system*. en. Vol. 2. DARcorporation, 2017. ISBN: 978-1-884885-43-3. URL: <https://books.google.nl/books?id=1Ia-tAEACAAJ>.
- [54] R.H. Myers, D.C. Montgomery, and C.M. Anderson-Cook. *Response Surface Methodology: Process and Product Optimization Using Designed Experiments*. English. 3rd. Wiley Series in Probability and Statistics. Wiley, Jan. 2009. ISBN: 978-0-470-17446-3.
- [55] Michael D McKay, Richard J Beckman, and William J Conover. "A comparison of three methods for selecting values of input variables in the analysis of output from a computer code". en. In: *Technometrics* 42.1 (Feb. 2000). Publisher: American Statistical Association and American Society for Quality, pp. 55–61. ISSN: 0040-1706. URL: <http://www.jstor.org/stable/1271432>.
- [56] J. C. Carr, W. R. Fright, and R. K. Beatson. "Surface interpolation with radial basis functions for medical imaging". In: *IEEE Transactions on Medical Imaging* 16.1 (Feb. 1997), pp. 96–107. ISSN: 1558-254X. DOI: [10.1109/42.552059](https://doi.org/10.1109/42.552059).
- [57] Snorri Gudmundsson. *General aviation aircraft design: applied methods and procedures*. eng. Second edition. Oxford Cambridge, MA: Butterworth-Heinemann, 2022. ISBN: 978-0-12-818465-3.
- [58] R. de Vries. "Hybrid-Electric Aircraft with Over-the-Wing Distributed Propulsion: Aerodynamic Performance and Conceptual Design". en. PhD thesis. Delft University of Technology, 2022. URL: <http://resolver.tudelft.nl/uuid:ef87dc11-e7b2-4726-a41f-28588d64c58d> (visited on 05/17/2023).
- [59] Eric Jones, Travis Oliphant, and Pearu Peterson. *SciPy: Open Source Scientific Tools for Python*. 2001. URL: <http://www.scipy.org/> (visited on 09/14/2023).

-
- [60] Wilna Du Toit. “Radial basis function interpolation”. en. MA thesis. Stellenbosch, Western Cape, South Africa: Stellenbosch University, Mar. 2008. URL: <http://hdl.handle.net/10019.1/2002>.